Stony Brook University

Modeling Heterogeneous Chemistry of Air Pollutants: Co-Adsorption of O_3, NO_2, and H_2O on Soot Coated with Benzo[a]pyrene in an Urban Pollution Scenario

A Thesis Presented

by

Marco Springmann

to

The Graduate School

in Partial Fulfillment of the Requirements

for the Degree of

Master of Arts

in

Physics

Stony Brook University

August 2009

Stony Brook University

The Graduate School

Marco Springmann

We, the thesis committee for the above candidate for the Master of Arts degree, hereby recommend acceptance of this thesis.

Daniel A. Knopf – Thesis Advisor
Assistant Professor, School of Marine and Atmospheric Sciences

Marvin A. Geller – Chairperson of Defense
Adjunct Professor, Department of Physics and Astronomy

Philip B. Allen
Professor, Department of Physics and Astronomy

Robert L. de Zafra
Research Professor, Department of Physics and Astronomy

This thesis is accepted by the Graduate School.

Lawrence Martin
Dean of the Graduate School

Abstract of the Thesis

Modeling Heterogeneous Chemistry of Air Pollutants: Co-Adsorption of O_3, NO_2, and H_2O on Soot Coated with Benzo[a]pyrene in an Urban Pollution Scenario

by

Marco Springmann

Master of Arts

in

Physics

Stony Brook University

2009

This study assesses in detail the effects of heterogeneous chemistry on the particle surface and gas-phase composition by modeling the reversible co-adsorption of O_3, NO_2, and H_2O on soot coated with benzo[a]pyrene (BaP) for an urban pollution scenario over a period of five days. By coupling the Pöschl-Rudich-Ammann (PRA) kinetic framework for aerosols to a box model version of the gas phase mechanism RADM2, it is possible to track individual concentrations of gas-phase and surface species over the course of several days. The flux-based PRA formulation takes into account changes in the uptake kinetics due to changes in the chemical gas-phase and particle surface compositions. This dynamic uptake coefficient approach is employed for the first time in a broader atmospheric context of an urban pollution scenario. The results show a decrease of the O_3 and NO_2 uptake coefficients by more than three orders of magnitude or 99.9% within the first six hours of simulation time.

Thereafter, periodic peaks of the uptake coefficients follow the diurnal cycle of gas-phase O_3-NO_x reactions. Physisorption of water vapor prolongs the half-life of the coating substance BaP by up to a factor of seven by permanently occupying $\sim 75\%$ of the soot surface. Soot emissions modeled by replenishing reactive surface sites lead to maximum gas-phase O_3 depletions of 41 ppbv for an hourly and 7.8 ppbv for a six-hourly replenishment cycle for the co-adsorption of O_3 and NO_2. For the co-adsorption of O_3, NO_2, and water vapor, the O_3 gas-phase concentration decreases due to the heterogeneous reactions and the hourly replenishment cycle by 19 ppbv or 12%, the NO_2 gas-phase concentration increases during nighttime by 0.1 ppbv or 16%, and the NO concentration increases by 11 pptv or 16% during daytime and 0.3 pptv or 58% during nighttime. This conceptual study highlights the interdependence of co-adsorbing species and their non-linear gas-phase feedback. It yields further insight into the atmospheric oxidation of particles and guides future modeling and experimental investigations of the heterogeneous chemistry and chemical aging of aerosols.

Contents

List of Figures

List of Tables

Acknowledgements

I want to express my gratitude to my advisors Daniel A. Knopf and Nicole Riemer for their guidance, support, and their great responsiveness!

I also want to thank the Physics Department, especially the graduate program director Laszlo Mihaly for letting me undertake this research project in the School of Marine and Atmospheric Sciences, and I want to thank the members of the School of Marine and Atmospheric Sciences for welcoming and treating me so warmly.

On the personal side, I want to thank my friends and family for their unconditional support!

The text of this thesis in part is a reprint of the materials as it appears in:

M. Springmann, D. A. Knopf, and N. Riemer. Detailed Heterogeneous Chemistry in an Urban Plume Box Model: Reversible Co-Adsorption of O_3, NO_2, and H_2O on Soot coated with Benzo[a]pyrene. *Atmospheric Chemistry and Physics Discussions*, 9(2):1005510099, 2009. ISSN 1680-7367. URL http://www.atmos-chem-phys-discuss.net/9/10055/2009/. [1].

The co-author(s) listed in the publication directed and supervised the research that forms the basis for this thesis.

Chapter 1

Introduction

Urban air pollution has been a danger to human health and the environment ever since urbanities existed [2, 3]. From ancient Rome to London during the Industrial Revolution, to Los Angeles in the 20th century, to Beijing and other metropoles today, severe air pollution can be found through time and around the world. One example of urban air pollution is shown in Figure 1.1 for the case of Beijing.

Figure 1.1: Smog episode in Beijing, China. Credits: Guang Niu, Getty Images

From the 13th to the 20th century, documented air pollution problems were primarily associated with high concentrations of sulfur dioxide (SO_2) and soot particles originated from the combustion of coal and other raw materials. Due to a severe air pollution episode in London[1], this kind of air pollution is often referred to as London smog, where the word *smog* describes the combination of smoke and fog, which was characteristic for air pollution episodes. The widespread use of the automobile coincided with the occurrence of another type of air pollution called *photochemical smog*. In air pollution events of such kind, air pollutants are produced photochemically, i.e., by chemical reactions in the presence of solar radiation. Due to its special severity in Los Angeles, it is also sometimes referred to as Los Angeles smog. Although distinct for these two cities, most air pollution events are characterized by a combination of high concentrations of particulate matter and photochemically produced air pollutants. This is also the case for the Beijing smog episode shown in Figure 1.1.

Urban air pollution episodes are caused by a combination of factors. One factor is the combustion of primarily fossil-fuels, chemicals and/or biomass, which is the source of primary pollutants. These pollutants are, e.g., nitrogen oxides ($NO_x = NO + NO_2$) and volatile organic compounds (VOCs), such as alkanes and other hydrocarbons, which are primarily emitted as vehicle exhaust, as well as particulate matter, which is also emitted from factories and power plants. Another factor is the meteorology. Cities are located in the planetary boundary layer, which are the lowest one to two kilometers of the atmosphere. For this altitude range, the temperature generally decreases with increasing altitude, so that pollutants emitted from the ground can disperse to higher altitudes and are thereby removed from the emission source. However, under certain conditions, a temperature inversion can form, in which the temperature increases with height. In these situations, air pollutants cannot disperse to higher altitudes, leading to a build-up of pollutants close to the ground. The conditions that facilitate temperature inversions are the emission of infra-red radiation from the ground, which is the case especially at night, the occurrence of winds that blow cool ocean air underneath warmer inland air, and the presence of subsiding high-pressure systems which warm from adiabatic compression. A third factor contributing to urban air pollution is the presence of sunlight as solar irradiation of the trapped primary air pollutants initiates the photochemical production of secondary air pollutants. These include oxidants, such as ozone (O_3), which have adverse health effects. High concentrations of O_3 cause eye-irritation, taint plants, damage materials, and cause respiratory problems.

[1]In 1952, 4,000 excess deaths were attributed to a single smog episode in London.

A major component of urban air pollution that is not produced photochemically is particulate matter. Of special interest are soot particles, which are produced from incomplete combustion processes, e.g., in power plants or diesel engines. With particle diameters ranging below 2.5 µm, soot particles can penetrate deep into lungs and lead to decreased lung function and increased mortality [4, 5]. They are also the dominant absorber of visible solar radiation in the atmosphere and contribute significantly to regional and global warming [6, 7]. Soot is regularly coated with a variety of polycyclic aromatic hydrocarbons (PAHs), which are produced in the same process of incomplete combustion. In contrast to the gas-phase reactions governing the production and loss of ground-level O_3, which are well known and incorporated into chemical gas-phase models, the chemistry involving soot is much less known. Reactions on the surface of soot particles can change the particles' physical properties, such as reflectivity, mass and size, but also their chemical composition which can influence the toxicity and reactivity of the particles.

Chemical reactions between the gas phase and the condensed phase, which includes the solid and liquid phases, are termed *heterogeneous reactions*. They can lead to changes in the composition of both the gas phase and the particle surface. The most prominent example of heterogeneous reactions in the atmosphere is the conversion of chlorine compounds to molecular chlorine (Cl_2) on polar stratospheric clouds. The converting reactions, whose speed is greatly enhanced on the ice surfaces in comparison to the gas phase, lead to the strong ozone depletion over the Antarctic during polar spring, known as the ozone hole [8–11].

This study focuses on heterogeneous reactions in the lower altitudes of the troposphere, specifically in the planetary boundary layer. It investigates the the interaction of soot particles with other air pollutants and typical atmospheric constituents in the urban environment. Specifically, the competitive co-adsorption and subsequent surface reactions of O_3, NO_2, and water vapor on soot particles coated with the PAH benzo[a]pyrene is modeled to determine the effects of these heterogeneous reactions on the particle and gas-phase compositions in a polluted urban environment. The model approach employs a novel kinetic model framework for aerosol surface chemistry and gas-particle interactions, which in reference to its authors is denoted as the Pöschl-Rudich-Ammann (PRA) framework [12]. It enables a detailed mathematical description of the physiochemical processes governing the uptake process and the particle surface reactions. This framework is implemented into the Second Generation Regional Acid Deposition Model (RADM2) [13], which is a well-established chemical gas-phase mechanism for modeling atmospheric chemistry

on a regional scale. It simulates diurnal changes in photolysis frequencies and gas-phase emissions and can therefore be used to place the heterogeneous reactions in a realistic atmospheric environment. This is the first time that such detailed heterogeneous chemistry is evaluated in an atmospheric context. From the modeling perspective, it is a novelty, since modeling studies often use simple parametrizations of the uptake process [e.g., 14, 15]. From the experimental perspective, it exceeds the complexity of current laboratory experiments which consider two adsorbents at most without a dynamic atmospheric context. Thus, this study shows the application of an extended atmospheric model system and can provide valuable information for the conception of new experiments.

This thesis is structured as follows. The second chapter provides a background in the reactions of air pollutants, the mathematical description of the chemical kinetics governing these reactions, and an overview of atmospheric models and model studies relevant to this study's model system. In the third chapter, the model approach followed in this study is outlined. The centerpiece of this thesis is a published academic paper in chapter four which presents and discusses the obtained model results. Additional results are also shown in the same chapter. The material in the appendices is used to supplement the chapters' contents.

Chapter 2

Background

This chapter provides the background for the undertaken modeling study. It includes information on air pollutants, their chemical interactions, and their representations in atmospheric models. It starts with presenting the photochemistry of gaseous air pollutants. Then, the characteristics of particulate matter, in particular soot, are discussed and laboratory studies on heterogeneous reaction between soot and gas-phase species are reviewed. After discussing the chemical kinetics with special emphasis on heterogeneous reactions, a brief introduction into atmospheric models and model studies of heterogeneous reactions on soot are presented. This chapter closes with summarizing the motivations, but also the limitations of the undertaken modeling study.

2.1 Photochemistry of Air Pollutants

Urban air pollution is characterized, on the gas-phase side, by the formation of O_3 and other oxidants by photochemical reactions of NO_x and VOCs. The following is a basic illustration of these reactions. A more detailed account of the involved processes can be found in Finlayson-Pitts and Pitts [2] and Seinfeld and Pandis [16].

Groundlevel O_3 is produced by the photolysis, i.e., the photodissociation, of nitrogen dioxide (NO_2) to nitric oxide (NO) and excited atomic oxygen ($O(^3P)$),

$$NO_2(g) + h\nu \rightarrow NO(g) + O(^3P)(g)\,, \lambda < 420 \text{ nm}\,, \tag{2.1}$$

followed by the reaction of the atomic oxygen with molecular oxygen (O_2) [17]:

$$O(^3P)(g) + O_2(g) \xrightarrow{M} O_3(g)\,, \tag{2.2}$$

where M denotes the presence of a molecule M that carries off excess energy.

Some NO_2 is emitted directly into the atmosphere by combustion processes [18], but most of it is formed by the oxidation of NO, the major nitrogeneous byproduct of combustion.

In the unpolluted background troposphere, NO is oxidized by O_3,

$$\mathrm{NO(g) + O_3(g) \rightarrow NO_2(g) + O_2(g)\,, } \tag{2.3}$$

which results, together with (2.1) and (2.2), in a photostationary-state relationship between the concentrations of O_3, NO, and NO_2.

In a polluted environment, the conversion from NO to NO_2 is part of the oxidation of reactive VOCs which are emitted alongside NO by combustion processes. The oxidation is initialized by reactive species, such as the hydroxyl radical (OH), which break down the VOCs into radicals, denoted by R, and, for the case of oxidation by OH, water vapor:

$$\mathrm{VOC(g) + OH \rightarrow R(g) + H_2O(g)\,. } \tag{2.4}$$

The radical then reacts with molecular oxygen (O_2) to form a peroxy radical, denoted by RO_2, which then oxidizes NO to NO_2:

$$\mathrm{R(g) + O_2(g) \xrightarrow{M} RO_2(g)\,, } \tag{2.5}$$

$$\mathrm{NO(g) + RO_2(g) \rightarrow NO_2(g) + RO(g)\,. } \tag{2.6}$$

VOCs emitted in urban air include alkanes, alkenes, alkynes, aldehydes, ketones, alcohols, aromatics, and hemiterpenes. Among these, the greatest contributors to O_3 formation can be determined by combining abundance and reactive ability of each VOC. For example, for a smog episode in Los Angeles in the year 1987, the five most important VOCs in terms of generating O_3 were the aromatic hydrocarbons xylene and toluene, the alkene ethene, and the aldehydes acetaldehyde and formaldehyde [19, 20].

Some of these VOCs can also be broken down by photolysis and by reactions with the hydroperoxy radical (HO_2), atomic oxygen (O), nitrate (NO_3), and O_3. However, only OH can break down all of the VOCs. OH is produced in urban air by various reactions throughout the day. These include the photolysis of nitrous acid (HONO), also an emission product of automobiles, the photolysis of aldehydes with subsequent oxidation processes, and the photolysis of O_3 with a subsequent reaction with water vapor.

The presence of sunlight is an essential ingredient of urban air pollution. It initiates the production of the OH and other radicals that enable the oxidation of NO to NO_2 by VOCs. Then sunlight photodissociates NO_2 to NO and O which then reacts with O_2 to form O_3. In the absence of sunlight, the photol-

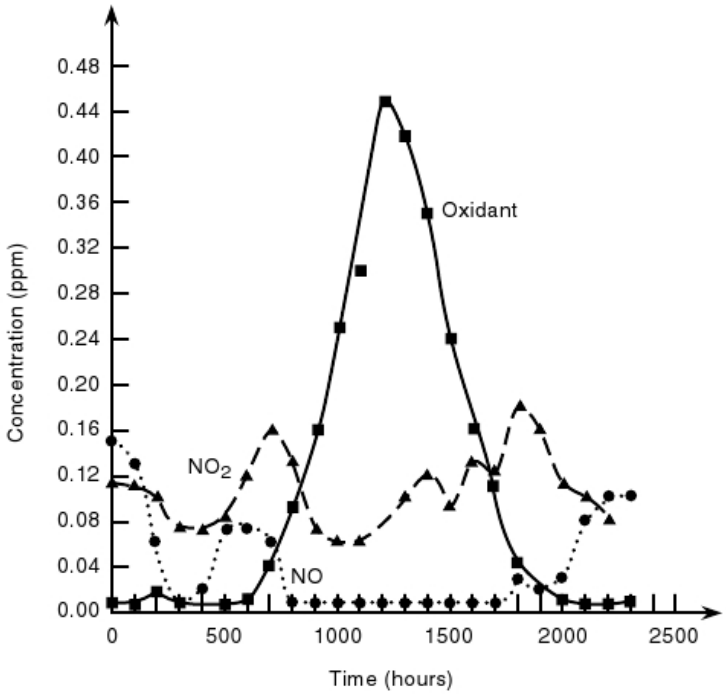

Figure 2.1: Diurnal variation of NO, NO_2, and total oxidant in Pasadena, California, on July 25, 1973. Adapted from Finlayson-Pitts and Pitts [2]

ysis reactions shut off, thereby also haltering the O_3 production. Continued emissions of NO can then lead to nighttime O_3 depletion by reaction (2.3).

A typical diurnal variation of NO, NO_2, and oxidants, such as O_3, is shown in Figure 2.1 for a severe photochemical air pollution episode in July 1973. In the early morning, the NO concentration rises and reaches a maximum coinciding with peak automobile traffic. Reactions (2.4) to (2.6) convert NO to NO_2. When enough NO_2 has built up, reactions (2.1) and (2.2) set in, causing the high production of oxidants, mainly O_3, at noon and and early afternoon. In the night, the oxidant concentration decreases again due to the reaction with NO via (2.3) and due the absence of sunlight which stops the photolytic reactions that led to its production.

Since in the night, NO_2 is not depleted by photolysis either, it can participate in reactions producing the nitrate radical NO_3 and dinitrogen pentoxide (N_2O_5):

$$\mathrm{NO_2(g) + O_3(g) \;\rightarrow\; NO_3(g) + O_2(g)\,,} \tag{2.7}$$

$$\mathrm{NO_2(g) + NO_3(g) \;\overset{M}{\rightleftarrows}\; N_2O_5(g)\,.} \tag{2.8}$$

The gaseous N_2O_5 can then react with liquid particles to produce nitric acid (HNO_3) which can stay in dissolved form or desorb to the gas phase [e. g. 21]:

$$N_2O_5(g) + H_2O(l) \rightarrow 2HNO_3(aq)\ . \tag{2.9}$$

Reaction (2.9), together with reactions (2.7) and (2.8), convert the reactive nitrogen species NO_2 and NO_3 to the longer-lived nitrogen reservoir species HNO_3. If NO_x concentrations are low, this conversion can also influence O_3 production.

Reaction (2.9) occurs between the gas phase and the condensed phase (here, the liquid phase) and is therefore one example of a heterogeneous reaction, which will be covered in more detail in the next section about particulate matter.

2.2 Particulate Matter in Air Pollution

Alongside gas-phase species that lead to photochemical smog episodes, also particulate matter (PM) is emitted in combustion processes. While large, millimeter-sized particles are removed in the combustion zone as bottom ash or wall deposits, or are collected in post-combustion gas cleaning devices, small, micrometer-sized particles travel with the combustion exhaust gas and contribute to ambient air pollution on both the urban and regional scale [22]. Such particles that are suspended in air are defined as *aerosols*.

Classification by Size

Figure 2.2 gives an overview of the sizes of atmospheric particles. The focus of this classification is on the micrometer-sized *fine particles*, often denoted as $PM_{2.5}$, i.e., particles with diameters smaller than 2.5 µm. These can be subdivided into particles in the nucleation and accumulation mode [24]. The *nucleation mode* contains particles with diameters less than 0.1 µm which can be directly emitted (primary) particles or newly nucleated (secondary) particles formed directly in the gas phase. Their size can increase due to coagulation with other particles and due to condensation of gases onto the particle. This can move the particles into the *accumulation mode* which contains particles with diameters between 0.1 and 2 µm. Particles in this size range tend to accumulate in the atmosphere, since they do not settle out or agglomerate to form larger particles. The accumulation mode particles are likely to affect human health, since they penetrate deep into the lungs [25]. They also affect visibility by scattering and absorbing light, causing decreases in visibility and changes in the radiative budget [26]. Some of the particles in this size range

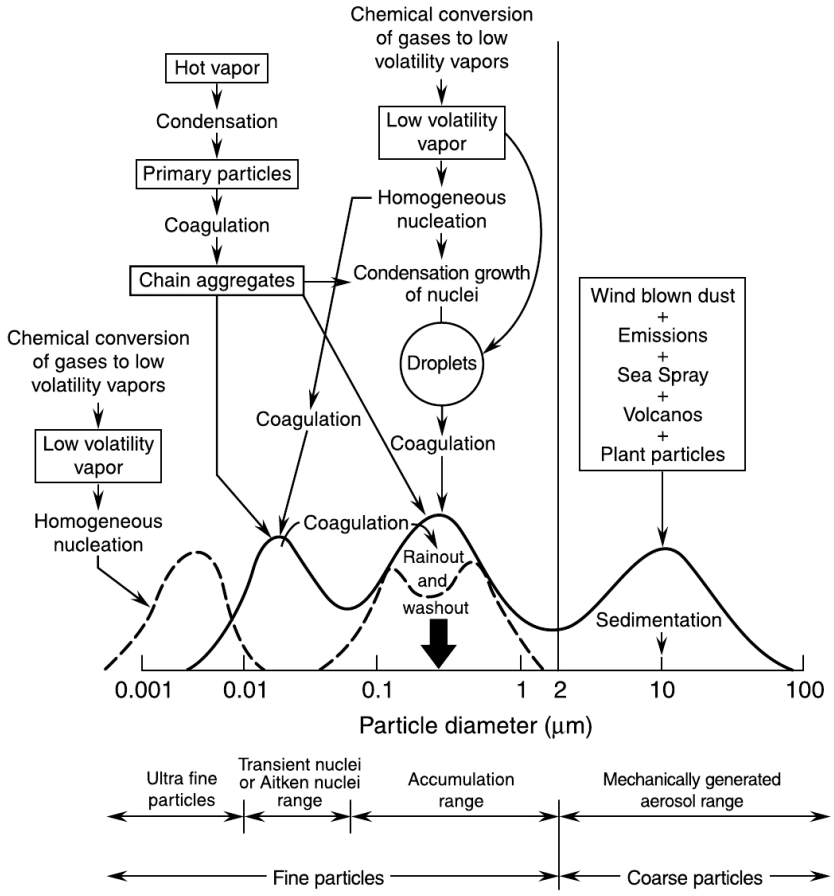

Figure 2.2: Idealized schematic of the size distribution of atmospheric aerosols with principle modes, sources, and indicated particle formation and removal mechanisms. Adapted from Finlayson-Pitts and Pitts [2], Whitby and Sverdrup [23].

are removed by rain. However, to be removed from the air by gravitational settling, the particles have to be larger than about 2 μm and are then termed *coarse mode* particles. Since the fine particles in the nucleation and accumulation mode do not grow by condensation much larger than 1 μm, coarse mode particles originate primarily from emissions. The characteristic residence times of aerosol particles in the atmosphere range from hours to weeks, depending on size, altitude, and atmospheric conditions [27, 28].

2.2.1 Soot

The particulate components emitted during the combustion of fossil fuels include fly ash (consisting of various traces metals), metals, sulfates, organic matter, and carbonaceous particles [24]. Carbonaceous aerosol components (organic compounds and black or elementary carbon) account for a large fraction of air particulate matter — about 40% of $PM_{2.5}$ [29]. About half of the total carbon content in urban air is comprised of black carbon or *soot* [29], which originates from the incomplete combustion of hydrocarbons, primarily from coal, diesel-fuel, and jet-fuel. In Los Angeles, 93% of soot has been attributed to motor vehicle sources; in Detroit, 47%; and in Western Europe, 70 to 90% [16, 30, 31].

Morphology of Soot

Soot particles are straight or branched agglomerates of elementary carbonaceous particles which are roughly spherical in shape and consist of graphene-like layers. Both, agglomerate and elementary soot particles are shown in Figure 2.3. Although the agglomerates can form larger, visible soot particles that have sizes up to a few micrometers, more than 90% of the emitted soot mass is constituted by sub-micrometer particles. The morphology and composition of soot particles varies from particle to particle. Most soot particles in polluted areas are found in the size range from 0.05 to 0.12 µm [32]. The soot concentrations in urban areas can vary from 1.5 to 20 µg m^{-3} and from 0.2 to 2.0 µg m^{-3} in rural and remote areas [16].

The soot surface has a fractal-like (or porous) geometry [35], whose surface area cannot be directly assessed. Therefore indirect methods have to be used. The most commonly employed method is based on the Brunauer-Emmett-Teller (BET) theory [36] which assumes that under suitable pressure and temperature conditions, gas molecules physically adsorb on surfaces in multiple layers with no interaction between the layers. Knowing the adsorbed gas quantity, the surface area can be determined by $S = \mathrm{N_A}\sigma_{\mathrm{X}_i} n_{\mathrm{m}}$, where $\mathrm{N_A}$ is Avogadro's number, σ_{X_i} is the adsorbent's molecular cross section, and n_{m} is the amount adsorbed (in moles per gram of adsorbent). The so-determined surface areas of soot can range up to several hundred m^2 per gram [37, 38].

The soot particles' morphology and chemical composition change with time. As they age, they are "mixed" with other particles through coagulation, condensation of secondary aerosol compounds, and cloud processing on characteristic time scales of a few days [39]. This eventually leads to an internal aerosol mixture consisting of elementary and organic carbon and small amounts of other elements, such as oxygen, nitrogen, and hydrogen [16]. Fresh

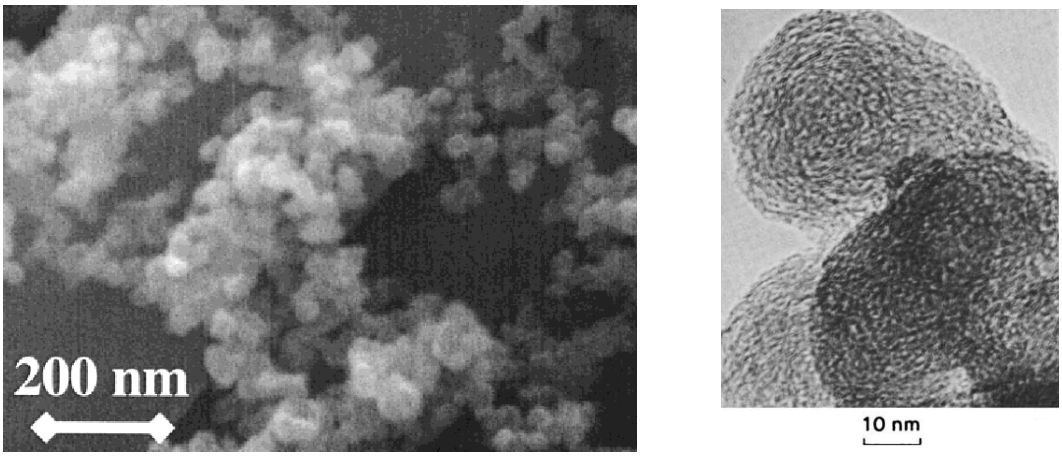

Figure 2.3: Agglomerates of diesel soot particles (left), imaged with a high-resolution scanning electron microscope (HRSEM); adapted from Arens et al. [33]. Elementary diesel soot particles (right), imaged with a transmission electron microscope; adapted from Nienow and Roberts [34].

soot particles also contain compounds other than graphitic carbon. For example, soot particles emitted from spark-ignition engines consist of a core of elementary carbon covered with a layer of polycyclic aromatic hydrocarbons (PAHs) — organic compounds with more than one benzene ring — and an outermost shell of organic and inorganic compounds [40, 41]. Although soot particles tend to be hydrophobic, the coating of soot particles with organic compounds that act as surfactants increases their hygroscopicity [42].

Soot Coating

Among the PAHs that are found to coat soot particles are 5- and 6-ring PAHs, such as benzo[a]pyrene (BaP), a 5-ring PAH with the chemical formula $C_{20}H_{12}$ whose structure is shown in Figure 2.4. BaP was found to be identical to carcinogenic substances in coal tar and induced cancer in mice [43]. It also was identified in carcinogenic extracts of ambient air particles [44–47]. This led the International Agency for Research on Cancer (IARC), as well as the U. S. Environmental Protection Agency (EPA) to classify BaP as animal carcinogen and "probable" human carcinogen [48, 49]. In addition, BaP was found to be a promutagen that can be activated and converted to mutagenic metabolites. Levels of BaP found in urban environments are, e.g., about 1.6 ng m^{-3} in urban Boston air [50] and 2.0 ng m^{-3} in Central London [51].

The photodissociation of BaP and the toxicity of its reaction products was shown to depend on the substrate surface, in particular its carbon content.

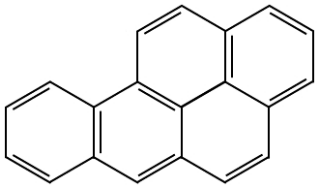

Figure 2.4: Molecular structure of benzo[a]pyrene

While sunlight contributes to BaP degradation when deposited on glass surfaces, thin-layer chromatography plates, and inorganic oxides, such as SiO_2 and Al_2O_3 [52–54], BaP deposited on fly ash substrates and carbon black (soot) are found to be photostable [52, 55, 56]. And, while upon ozonolysis, i.e., exposure to O_3, BaP deposited on glass fiber filters was shown to react readily to form direct-acting mutagens [57], the ozonolosis of BaP dissolved in liquid solution and of BaP deposited on soot particles showed a decrease or steadiness in the toxicity of the BaP degradation products [58, 59].

In laboratory experiments, BaP is often regarded as a proxy for the wider class of polycyclic aromatic compounds (PACs), but also for soot in general due to its structural similarities to the soot surface [60].

2.3 Heterogeneous Reactions on Soot

Laboratory studies have indicated that soot interacts chemically with a variety of gas-phase speciess [29, 34, 61].

O_3 and Soot

Ozonolysis experiments of soot showed rapid initial gas uptake followed by a slower uptake regime during which surface reactions occurred [60, 62–64]. While the detailed reaction pathways of the surface reactions is not always clear, up to 29 reaction products with 3 main products have been identified from the ozonolysis of BaP deposited on soot [59]. Some of these reaction products can be volatile species, such as CO, CO_2, and H_2O, which desorb to the gas phase [65, 66].

NO_2 on Soot

The same two-step kinetic process, fast initial uptake followed by a slower uptake regime, was found in experiments probing the adsorption and reactivity of NO_2 on soot [21, 33, 67–69]. Fourier transform infrared spectroscopy (FTIR)

identified absorption bands of an organic nitrate R-O-NO_2 (the R stands for the soot bulk) and nitro compound R-NO_2 on soot after exposure to NO_2 [70].

Studies also indicated the subsequent formation and desorption of nitrous acid (HONO), which is important for initiating daytime photochemistry by providing a source for the hydroxyl radical (OH) [33, 68, 71, 72] via:

$$NO_2(s) + RH(s) \rightarrow HONO(g) + R(s)\,, \tag{2.10}$$

$$HONO(g) + h\nu \rightarrow OH(g) + NO(g)\,, \lambda < 400\ \text{nm}\,, \tag{2.11}$$

where RH is part of a functional group on the surface of the soot particle, from which a hydrogen atom (H) can be abstracted. In the presence of sunlight, HONO rapidly photodissociates to form the OH radical which can then initialize the oxidation of NO to NO_2. This contributes to O_3 production as described in the last section.

While the ozonolysis of soot coated with BaP resulted in reaction products of similar toxicity [59], the exposure of particle-associated 4- and 5-ring PAHs to NO_2 (and traces of HNO_3) in air resulted in significant yields of nitro-PAH, which are direct-acting, high-potency mutagens [57, 73].

H_2O on Soot

The uptake of water affects the soot particles' ability to act as cloud condensation nuclei [74, 75]. It was found that water uptake increases with soot aging in air, surface oxidation, relative humidity, in the presence of physisorbed O_2, and after the treatment with O_3 [74–76].

Two mechanisms of soot-water interaction were identified [37]: In the absorption mechanism, water dissolutes into the soot bulk and forms a soot-water-soluble coverage; in the adsorption mechanism, water molecules adsorb onto soot surface sites. Which mechanism is followed depends on the soot particle's hydrophilicity, which can vary from hygroscopic (very hydrophilic) to hydrophobic, and it also depends on the kind of soot and its production process [37].

In an experiment investigating the interaction of O_3 and H_2O with soot coated with BaP, the results indicated a rapid, reversible, and competitive co-adsorption of O_3 and H_2O [60].

HO_2 and NO_3 on Soot

Other gases that can be taken up by soot surfaces or its PAH coating include HO_2 [21, 77] and NO_3 [78]. In the atmosphere, HO_2 is a direct oxidant of NO to NO_2 and a OH source via reaction (2.6) (with R replaced by H) and

therefore of importance for the gas-phase NO_2 and O_3 production. However, less is known about its reaction mechanism on the surface. NO_3 was found to be the dominant adsorbent among N_2O_5, NO_2, HNO_3, and O_3 on pure 4-ring PAH surfaces. In the atmosphere, NO_3 uptake would decrease the efficiency of reaction (2.8) in forward-direction, thereby lowering the O_3 reducing effect of reaction (2.9). However, as mentioned in section 2.2.1, the PAH substrate has a great influence on the possible reaction pathways, so that an extrapolation to soot coated with PAHs might not be valid.

In each of the experiments described above, the efficiency of the uptake of gas-phase species on soot particles is quantified by an uptake coefficient, which is part of the chemical kinetics of heterogeneous reactions. These, as well as the mathematical representation of homogeneous reactions will be discussed in the next chapter.

2.4 Chemical Kinetics

Chemical kinetics represent a reaction mathematically. They express a relationship between the reactants' and the products' concentrations and can therefore be used to predict the concentrations of the chemical species that participate in the reaction at specific points in time, which is essential for modeling chemical processes. On the other hand, if the species' concentrations are measured experimentally, the chemical kinetics can be used to determine the reaction rate, i.e., the speed of the reaction and infer the concrete reaction pathway. Thus, the derivation of process-specific chemical kinetics reconciles laboratory measurements with the underlying physiochemical processes.

This section first introduces the general reaction kinetics, which is valid for reactions occurring in the same phase, e.g., in the gas phase. Then, heterogeneous kinetics are described, first, by a classic framework, mostly used for the interaction between gas-phase species and liquid particles, and then by a novel approach, which offers a comprehensive kinetic framework which is also valid for the interaction between gas-phase species and solid particles, such as soot.

2.4.1 Homogeneous Kinetics

Elementary reactions, i.e., reactions that cannot be broken down into two or more simpler reactions, can consist of one, two, or three reactants, correspondingly referred to as unimolecular, bimolecular, and termolecular processes, respectively. In most atmospheric cases, termolecular reactions involve molecular nitrogen (N_2) and molecular oxygen (O_2) as the third molecule which acts

as an inert stabilizer of the energy-rich intermediates formed by the reaction of the other two species by carrying away the excess energy and thereby preventing their dissociation back into the reactants. In such cases, the colliding third body is denoted by the symbol M. Reaction (2.2) is an example of such a reaction.

The majority of elementary reactions in the atmosphere are bimolecular, i.e., they consist of two reactant species. In general form, such a reaction can be written as a *stoichiometric equation*:

$$a\ \mathrm{A} + b\ \mathrm{B} \rightarrow c\ \mathrm{C} + d\ \mathrm{D}\,, \tag{2.12}$$

where a, b, c, and d are stoichiometric coefficients quantifying the rate of disappearance and appearance, respectively, of the chemical species A, B, C, and D.

The change in the concentration of each reactant and product with time, i.e., the *rate of reaction* r, is in proportion to the corresponding stoichiometric coefficient defined, by convention, as:

$$r = -\frac{1}{a}\frac{d[\mathrm{A}]}{dt} = -\frac{1}{b}\frac{d[\mathrm{B}]}{dt} = \frac{1}{c}\frac{d[\mathrm{C}]}{dt} = \frac{1}{d}\frac{d[\mathrm{D}]}{dt}\,, \tag{2.13}$$

where the square brackets denote the concentration of the species in brackets.

While the rate of reaction relates the temporal changes in the species' concentrations to each other, the *rate equation* (or rate law) quantifies these temporal changes by an absolute value. For the elementary generalized equation (2.12), the rate law is given by

$$r = k[\mathrm{A}]^a[\mathrm{B}]^b\,, \tag{2.14}$$

where k is the *rate constant*, which relates the rate of the reaction to the concentrations of the reactants.

The rate equation for the reaction (2.12) can now be written by equating (2.13) with (2.14), e. g., for the loss of molecules A as

$$-\frac{1}{a}\frac{d[\mathrm{A}]}{dt} = k[\mathrm{A}]^a[\mathrm{B}]^b\,. \tag{2.15}$$

The rate constant k can be temperature, as well as pressure dependent. The temperature dependence is empirically parametrized by the *Arrhenius equation*:

$$k = Ae^{-\frac{E_\mathrm{a}}{\mathrm{R}T}}\,, \tag{2.16}$$

where R is the gas contant (in J K^{-1} mol^{-1}), T the temperature (in Kelvin),

E_a the activation energy (in J mol^{-1}), and A a preexponential factor characteristic of the particular reaction. For most reactions in the troposphere, A is temperature independent or varies only insignificantly. However, for reactions in which the activation energy is small or zero, A can display a non-negligible temperature dependence, of the form $A = BT^n$, where the number n and the temperature-independent constant B are fitted to the specific reaction. Also the form of $A = A\,(T/T_0)$ is used, where T_0 is a reference temperature. Since atmospheric termolecular processes often involve an inert molecule M, usually N_2 and O_2 whose concentrations are pressure-related, the rate constant can also exhibit a pressure dependence, which was parametrized by Troe [79] as

$$k = \frac{k_0 k_\infty}{k_0 + k_\infty} F\,. \tag{2.17}$$

The parameters k_0 and k_∞ are high- and low-pressure limiting values, which are combinations of rate constants for the formation of an excited intermediate, its re-dissociation, and the collision with molecule M. F is a (vibrational) broadening factor that also depends on k_0, k_∞, and the temperature. However, in the following, the reaction rate will simply be denoted by k, without referring to its potential temperature and pressure dependence explicitly.

For elementary reactions, the coefficients a and b in (2.14) are the same stoichiometric coefficients as in reaction (2.12). The sum of the exponents a and b is called the *order* of the reaction, e.g., for the reaction $\mathrm{A} + \mathrm{B} \rightarrow \mathrm{C} + \mathrm{D}$, the rate equation for the loss of species A would be $-\frac{d[\mathrm{A}]}{dt} = k[\mathrm{A}][\mathrm{B}]$, so the reaction would be second order, since it is first order with respect to each reactant.

In reactions in which the concentration of one reactant is much larger than the concentration of the other reactant or reactants, it is customary to define a *pseudo-rate-constant*, which includes the larger reactant's concentration. For example, in tropospheric termolecular reactions which involve an inert collision molecule M, a pseudo-second-order rate constant k^bi can be defined which includes the concentration of M:

$$r = k^\mathrm{ter}[\mathrm{A}]^2[\mathrm{M}] = k^\mathrm{bi}[\mathrm{A}]^2\,. \tag{2.18}$$

For *overall* reactions, which include two or more elementary reactions, the exponents of the rate equations may be different from the stochiometric coefficients in the stochiometric equation and a generalized rate equation, for a

species X_i, can be written as:

$$r_i = \frac{d[X_i]}{dt} = \sum_{j=1}^{N_R} c_{ij} k_j \prod_{k=1}^{N_j} [X_k]^{c_{kj}} , \tag{2.19}$$

where c_{ij} and c_{kj} are stoichiometric coefficients; j numbers the reactions in which X_i is produced and lost, so that N_R is the total number of involved reactions; k numbers the participating reactants, so that N_j is the total number of reactants; and k_j is the rate constant for reaction j. For example, the overall rate equation for O_3 taking into account reactions (2.2) and (2.3) is

$$\frac{d[O_3]}{dt} = k_{(2.2)}[O][O_2] - k_{(2.3)}[NO][O_3] , \tag{2.20}$$

where the rate constants are denoted by the corresponding reactions.

2.4.2 Photolytic Reactions

As described in section 2.1, photolytic reactions play a crucial role in urban air pollution. They can be described as first-order reactions and are therefore included in the generalized rate equation (2.19). The general reaction and rate equation for the photodissociation of a molecule A, upon light absorption, are:

$$A + h\nu \rightarrow B + C , \tag{2.21}$$

$$\frac{d[A]}{dt} = -k_p[A] , \tag{2.22}$$

where $h\nu$ is the energy of a quantum of light with h being the Planck's constant (in J s), and ν the light's frequency. The rate constant k_p, also called the *photolysis rate*, is given by:

$$k_p = \int_\lambda \phi(\lambda)\sigma(\lambda)F(\lambda)d\lambda , \tag{2.23}$$

where $\phi(\lambda)$ is the quantum yield for photodissociation for a specific wavelength λ, which quantifies the relative efficiency of the photochemical or photophysical process, i.e., number of excited molecules by the process divided by the total number of photons absorbed; $\sigma(\lambda)$ is the absorption cross section for wavelength λ; and $F(\lambda)$ is the spherically integrated actinic flux, which describes the total intensity of light of wavelength λ including direct, scattered, and reflected radiation reaching molecule A.

2.4.3 Heterogeneous Kinetics

While the reaction kinetics mentioned in the previous section can be applied in a straight forward manner to chemical reactions in the gas phase and in solution, several other processes that influence the reaction kinetics need to be taken into account for heterogeneous reactions between the gas phase and the condensed phase.

The first general account for such atmospheric heterogeneous reactions was given for the interactions of gas-phase species with aqueous solutions, since such aqueous solutions are present in the atmosphere in the form of clouds, fogs, rain, and particulate matter coated with a liquid film [2]. An overview of the process governing the heterogeneous reactions between the gas phase and the liquid phase is given in Figure 2.5. As shown in the figure, the uptake of a gas into a liquid, including subsequent reactions, is determined by several physical and chemical processes. In order for heterogeneous reactions to take place, the gas has to first diffuse to the interface. At the interface, it can bounce off or is taken up by the surface. On the surface, the adsorbent can either react, or dissolve and diffuse into the bulk, where it may subsequently react as well. Reaction products and/or the adsorbent may evaporate again to the gas phase. This framework can also be adapted for the uptake on solid particles, for which chemical reactions occur on the surface of the particle.

Two important parameters for the uptake process are the accommodation coefficient α and the net uptake coefficient γ_{net}. The accommodation coefficient, also called the sticking coefficient, denotes the fraction of gas-condensed phase collisions that result in uptake of the gas by the condensed phase:

$$\alpha = \frac{\text{Number of gas molecules taken up by the surface}}{\text{Number of gas-surface collisions}} \,. \tag{2.24}$$

While desorption and evaporation back into the gas phase are excluded in this definition, they are included in the definition of the net uptake coefficient γ_{net}, sometimes referred to as uptake probability. It is defined as the net rate of uptake of the gas normalized to the rate of gas-surface collisions:

$$\gamma_{\text{net}} = \frac{\text{Number of gas molecules lost due to uptake}}{\text{Number of gas-surface collisions}} \,. \tag{2.25}$$

In experiments, the adsorbent-specific γ_{net} is inferred from the adsorbent's net gas-phase loss due to uptake on a particle. This can be done, if the adsorbent's collision flux, $J_{\text{coll,X}_i}$, and the particle surface concentration in air,

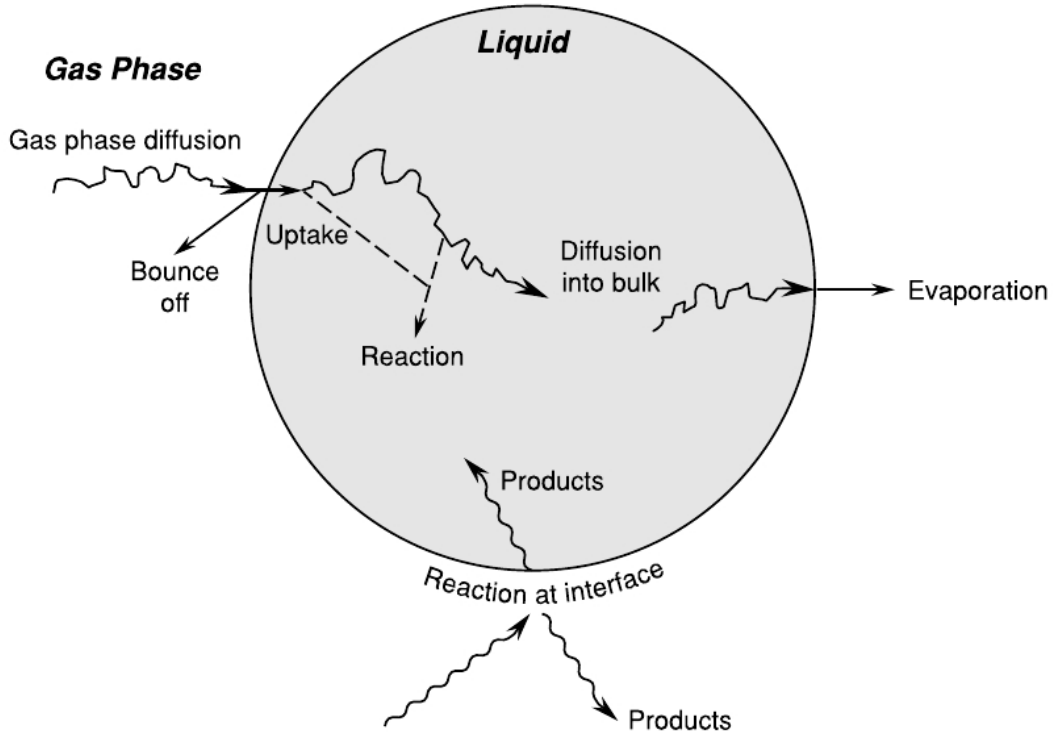

Figure 2.5: Schematic diagram of uptake and reaction of gases in liquids. Adapted from Finlayson-Pitts and Pitts [2].

$[\mathrm{PS}]_\mathrm{g}$, are known, via the relationship:

$$\left[\frac{\mathrm{d}}{\mathrm{dt}}[\mathrm{X}_i]_\mathrm{g}\right]_\mathrm{uptake} = -J_{\mathrm{coll},\mathrm{X}_i}\gamma_{\mathrm{net},\mathrm{X}_i}[\mathrm{PS}]_\mathrm{g}\ , \tag{2.26}$$

where X_i denotes the specific adsorbent.

The collision flux, i.e., the rate of gas-surface collisions of a molecule X_i is given by

$$J_{\mathrm{coll},\mathrm{X}_i} = [\mathrm{X}_i]_\mathrm{g}\frac{\omega_{\mathrm{X}_i}}{4}\ , \tag{2.27}$$

where $[\mathrm{X}_i]_\mathrm{g}$ is the adsorbent's gas-phase concentration and ω_{X_i} is the mean thermal velocity of molecule X_i given by $\omega_{\mathrm{X}_i} = \sqrt{8\mathrm{R}T/(\pi M_{\mathrm{X}_i})}$, in which R is the universal gas constant (in J K^{-1} mol^{-1}), T is the absolute temperature (in K), and M_{X_i} is the molar mass of species X_i (in g mol^{-1}).

By inserting equation (2.27) into (2.26), the net gas-phase loss of adsorbent

X_i can be obtained in more explicit form as

$$\left[\frac{\mathrm{d}}{\mathrm{dt}}[\mathrm{X}_i]_\mathrm{g}\right]_\mathrm{uptake} = -\gamma_{\mathrm{net},\mathrm{X}_i}[\mathrm{PS}]_\mathrm{g}[\mathrm{X}_i]_\mathrm{g}\frac{\omega_{\mathrm{X}_i}}{4} = -k_{\mathrm{g,p},\mathrm{X}_i}[\mathrm{X}_i]_\mathrm{g} \ , \tag{2.28}$$

where $k_{\mathrm{g,p},\mathrm{X}_i} = \gamma_{\mathrm{net},\mathrm{X}_i}[\mathrm{PS}]_\mathrm{g}\frac{\omega_{\mathrm{X}_i}}{4}$ is a pseudo-first order rate coefficient that can be defined to treat the gas-phase uptake as a pseudo-first order loss mechanism with respect to the adsorbent's gas-phase concentration.

Equation (2.28) is a dynamic equation, since the adsorbent's gas-phase concentration $[\mathrm{X}_i]_\mathrm{g}$ and the particle surface concentration $[\mathrm{PS}]_\mathrm{g}$ can change with time. This is also true for the net uptake coefficient $\gamma_{\mathrm{net},\mathrm{X}_i}$, which contains all physiochemical processes illustrated in Figure 2.5, such as desorption, dissolution and diffusion, and surface reactions. Thus, the explicit form of $\gamma_{\mathrm{net},\mathrm{X}_i}$ determines not only the net gas-phase uptake, but also the surface composition. Resolving these different processes enables a fundamental understanding of the uptake process.

In the following, two models with different parametrizations of $\gamma_{\mathrm{net},\mathrm{X}_i}$ will be presented. These are the resistor model, which decouples the involved physiochemical processes, and the PRA model framework, which employs a flux-based approach that emphasizes the dynamic nature of the uptake process.

Resistor Model

The uptake of a gas by the condensed phase followed by its reactions can be described by a series of coupled differential equations [80], which in most cases have to be solved numerically. The *resistor model* [81, 82] is an approximation, in which the individual processes governing the uptake are treated as resistances in analogy to an electric circuit. An outline of this model is shown in Figure 2.6. Dimensionless "conductances" Γ are associated with each process, reflecting the rate (or speed) of each process normalized to the rate of gas-surface collisions. The corresponding "resistances" are given by $1/\Gamma$. The net resistance, corresponding to the inverse of the net uptake coefficient, $1/\gamma_\mathrm{net}$, is obtained by combining the individual resistances in analogy to an electric circuit, i.e., by adding the resistances connected in series and by adding their inverse for resistances connected in parallel:

$$\frac{1}{\gamma_\mathrm{net}} = \frac{1}{\Gamma_\mathrm{g}} + \frac{1}{\alpha} + \frac{1}{\Gamma_\mathrm{rxn} + \Gamma_\mathrm{sol}} \ , \tag{2.29}$$

where α is the accommodation coefficient, γ_net the net uptake coefficient, Γ_g the conductance (=normalized rate) of gas-phase diffusion, Γ_rxn the conductance for reaction in the aqueous phase, and Γ_sol the conductance for solubility and

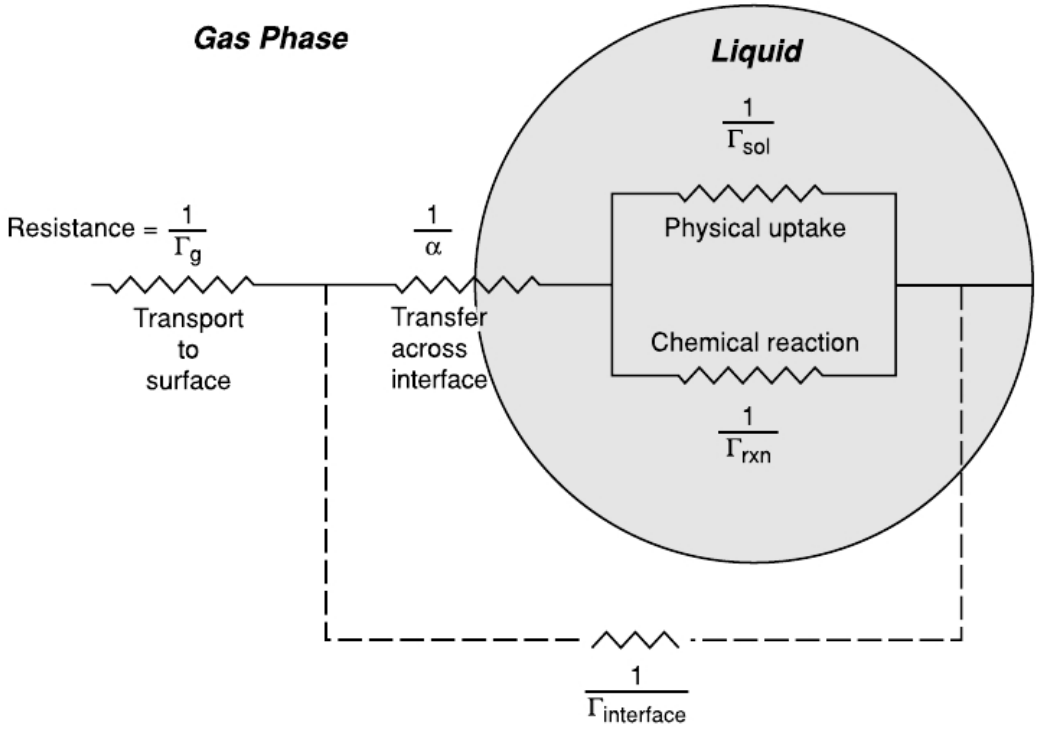

Figure 2.6: Schematic of resistor model for diffusion, uptake and reaction of gases with liquids. Γ_{g} represents the transport of gases to the surface of the particle, α the mass accommodation coefficient for transfer across the interface, Γ_{sol} the solubilization and diffusion in the liquid phase, Γ_{rxn} the bulk liquid reaction, and $\Gamma_{\mathrm{interface}}$ the reaction of the gas at the interface. Adapted from Finlayson-Pitts and Pitts [2].

diffusion into the bulk.

Under the assumption that every collision leads to an uptake, which is often the case for gas uptake by liquids, the rate of diffusion of a gas-phase molecule X_i to the particle surface is given by $2\pi D_{\mathrm{g}} d[\mathrm{X}_i]_{\mathrm{g}}$ [83], where D_{g} is the gas diffusion coefficient and d is the particle's diameter. Normalizing this rate to a spherical particle surface of πd^2 and to the collision rate (2.27) yields

$$\Gamma_{\mathrm{g}} = \frac{8\pi D_{\mathrm{g}} d[\mathrm{X}_i]_{\mathrm{g}}}{\pi d^2 [\mathrm{X}_i]_{\mathrm{g}} \omega_{\mathrm{X}_i}} = \frac{8 D_{\mathrm{g}}}{\omega_{\mathrm{X}_i} d} \,. \tag{2.30}$$

For such rapid uptake, the Boltzmann velocity distribution close to the surface is distorted, so that the speed towards the surface is effectively doubled. The

overall resistance is then given by

$$\frac{1}{\Gamma_{\mathrm{g}}} = \frac{\omega_{\mathrm{X}_i} d}{8 D_{\mathrm{g}}} - \frac{1}{2} \,. \tag{2.31}$$

An expression for the rate of dissolution can be obtained by assuming that the dissolution of gas-phase molecules occurs in a thin layer of thickness $(D_1 t)^{1/2}$, where D_1 is the diffusion coefficient in the liquid phase, and that the layer is in Henry's law equilibrium, i.e., the solubility of the gas in the liquid is proportional to the pressure of the gas above the liquid, $[\mathrm{X}_i] = H P_{\mathrm{X}_i}$, where H is the molecule-specific Henry's law constant and P_{X_i} is the pressure of the gas above the liquid. Then,

$$J_{\mathrm{sol}} = [\mathrm{X}_i]_{\mathrm{gs}} H \mathrm{R} T \sqrt{\frac{D_1}{\pi t}} \,, \tag{2.32}$$

where $[\mathrm{X}_i]_{\mathrm{gs}}$ is the gas-phase concentration of X_i immediately adjacent to the interface, R the gas constant, and t the time of exposure of the liquid to the gas. The rate of dissolution decreases with time of exposure of the liquid to the gas, since more evaporation back to the gas phase takes place when the concentration of the dissolved species increases. Normalizing by the flux rate of gas-surface collisions — with $[\mathrm{X}_i]_{\mathrm{gs}} = [\mathrm{X}_i]_{\mathrm{g}}$, since gas-phase diffusion is accounted for by the decoupled diffusion conductance — the conductance of solubility is given by:

$$\Gamma_{\mathrm{sol}} = \frac{4 H \mathrm{R} T}{\omega_{\mathrm{X}_i}} \sqrt{\frac{D_1}{\pi t}} \,. \tag{2.33}$$

If an irreversible, first-order reaction takes place in the interface layer in addition to diffusion and dissolution, and the solubility of the reaction product is assumed to be large, the conductance of solubility can be adapted to formulate the conductance of reactions:

$$\Gamma_{\mathrm{rxn}} = \frac{4 H \mathrm{R} T}{\omega_{\mathrm{X}_i}} \sqrt{D_1 k} \left[\coth\left(\frac{r}{l}\right) - \frac{l}{r} \right] \,, \tag{2.34}$$

where k is the reaction constant, r the particle radius, and l is the diffuso-reactive length, which is a measure of the distance from the interface at which the reaction occurs and is defined by $l = \sqrt{D_1/k}$. The second term in parenthesis accounts for a decreased rate of reaction in small particles, for which the reaction occurs throughout the particle volume, i.e., the diffuso-reactive length is the same, or greater than, the particle radius.

Combining equations (2.31) to (2.33), the net resistance can be written as:

$$\frac{1}{\gamma_{\text{net}}} = \frac{1}{\Gamma_{\text{g}}} + \frac{1}{\alpha} + \frac{\omega_{\text{X}_i}}{4HRT\left(\sqrt{\frac{D_1}{\pi t}} + \sqrt{D_1 k}\left[\coth\left(\frac{r}{l}\right) - \frac{l}{r}\right]\right)} \,. \tag{2.35}$$

Equation (2.35) is essentially an equilibrium expression, since, with the exception of the dissolution conductance, all conductances are time-independent. This is justified for the uptake onto liquid particles, since the dissolution into the liquid bulk equilibrates the bulk concentration and the outside pressure.

However, the resistor model, in the form of equation (2.35), has several shortcomings when adapting it to heterogeneous reactions between the gas phase and solid particles, where surface saturation effects introduce time-dependencies. Especially, the surface reactions on solid particles are generally different from those within a bulk liquid. As outlined in section 2.3, reactions on solid particles are dominated by competitive surface adsorption and chemical reactions among the surface components, which are not captured in equation (2.35).

Another point of critique of the resistor model is that too much emphasis is put on decoupling parameters, although they are intrinsically linked [84]. For example, Henry's law coefficient H could be replaced by an adsorption rate coefficient divided by an evaporation rate coefficient. Since the adsorption rate depends on the accommodation coefficient α, this would introduce a coupled α-dependence. Similar arguments hold for the reaction on solid particles, which also depend on α [84].

Addressing the first point of criticism, Ammann et al. [84] derived a conductance term that describes Langmuir-Hinshelwood type surface reactions by assuming a steady-state equilibrium between adsorption and desorption, whose derivation is outlined in appendix B. The equilibrium assumption, however, might not be valid at all times, especially not in the beginning of the uptake process. To overcome this and the aforementioned shortcomings, Pöschl, Rudich, and Ammann formulated a comprehensive kinetic model framework for aerosol and cloud surface chemistry and gas-particle interactions [12], referred to as PRA framework, which will be outlined in the next subsection.

PRA Framework

The PRA framework [12] describes gas-phase uptake and surface chemistry by a double-layer surface model with a sorption layer and a quasi-static layer, and by flux-based rate equations. Sketches of the model compartments and parametrized surface reactions are shown in Figure 2.7. Gas and bulk diffusion and reaction processes as described by the resistor model are now represented

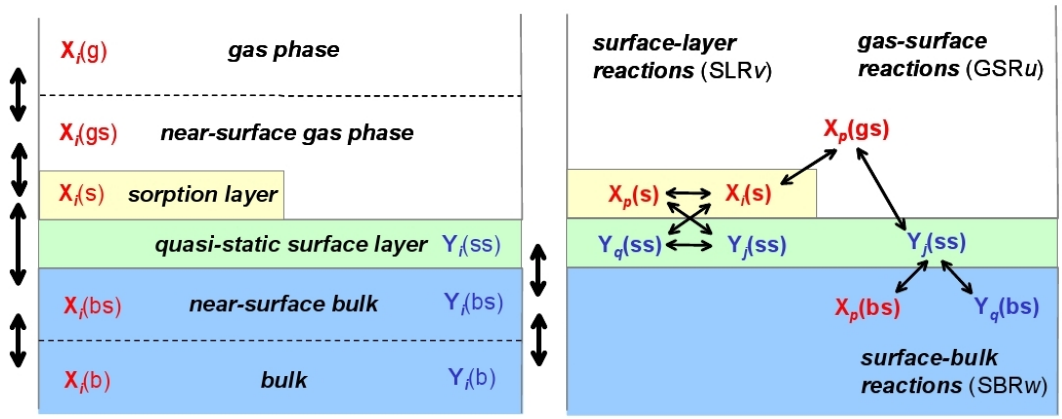

Figure 2.7: Double-layer surface model compartments with arrows indicating transport fluxes for volatile species X_i and non-volatile species Y_j (left). Classification of chemical reactions between volatile and non-volatile species at the surface (right). Adapted from Pöschl et al. [12].

by specific model compartments and transport fluxes, which distinguishes between the specific physiochemical processes.

Also the net uptake coefficient is now defined in terms of fluxes, as the ratio between the net flux of X_i to the condensed phase, $J_{\mathrm{net,X}_i}$, which can be decomposed into an adsorption and desorption flux, $J_{\mathrm{ads,X}_i}$ and $J_{\mathrm{des,X}_i}$ respectively, and the gas kinetic flux of X_i colliding with the surface, $J_{\mathrm{coll,X}_i}$:

$$\gamma_{\mathrm{net,X}_i} = \frac{J_{\mathrm{net,X}_i}}{J_{\mathrm{coll,X}_i}} = \frac{J_{\mathrm{ads,X}_i} - J_{\mathrm{des,X}_i}}{J_{\mathrm{coll,X}_i}} \,. \tag{2.36}$$

This definition is in accordance to definition (2.25) given before. In this formulation, the uptake processes are not decoupled, but are represented by the corresponding fluxes.

Instead of having a separate conductance for gas-phase diffusion as in the resistor model, a local depletion of X_i close to the surface with the resulting gas-phase diffusion can be accounted for by defining a gas-phase diffusion correction factor $C_{\mathrm{g,X}_i}$ that relates the gas-phase concentration close to the surface $[X_i]_{\mathrm{gs}}$ to the average gas-phase concentration $[X_i]_{\mathrm{g}}$:

$$C_{\mathrm{g,X}_i} = \frac{[X_i]_{\mathrm{gs}}}{[X_i]_{\mathrm{g}}} = \frac{\gamma_{\mathrm{eff,net,X}_i}}{\gamma_{\mathrm{net,X}_i}} \,. \tag{2.37}$$

This factor can be implemented into the diffusion-affected collision flux by replacing $[X_i]_{\mathrm{g}}$ in equation (2.27) by $[X_i]_{\mathrm{gs}} = C_{\mathrm{g,X}_i}[X_i]_{\mathrm{g}}$, since it is really the

gas-phase concentration close to the surface that collides with the surface. Alternatively, the net uptake coefficient $\gamma_{\mathrm{net,X}_i}$ can be multiplied by $C_{\mathrm{g,X}_i}$ to obtain an effective net uptake coefficient $\gamma_{\mathrm{eff,net,X}_i}$ which accounts for gas-phase diffusive effects. For γ_{X_i}-values smaller than one, which is often the case for gas uptake on solid particles, $C_{\mathrm{g,X}_i}$ can be determined as [83]

$$C_{\mathrm{g,X}_i} = \frac{1}{1 + \gamma_{\mathrm{X}_i} \frac{0.75+0.28\mathrm{Kn}_{\mathrm{X}_i}}{\mathrm{Kn}_{\mathrm{X}_i}(1+\mathrm{Kn}_{\mathrm{X}_i})}} \,, \tag{2.38}$$

where $\mathrm{Kn}_{\mathrm{X_i}}$ is the Knudsen number, the ratio of the mean free path of X_i in the gas phase, λ_{X_i}, and the particle radius. It can be approximated by [83]

$$\mathrm{Kn}_{\mathrm{X}_i} = \frac{2\lambda_{\mathrm{X}_i}}{d_{\mathrm{p}}} \approx \frac{6D_{\mathrm{g,X}_i}}{\omega_{\mathrm{X}_i} d_{\mathrm{p}}} \,, \tag{2.39}$$

where $D_{\mathrm{g,X}_i}$ is the gas-phase diffusion coefficient of species X_i and d_{p} is the particle diameter.

The adsorption flux of a gas molecule X_i is related to the collision flux via the accommodation coefficient $\alpha_{\mathrm{s,X}_i}$ representing the molecule's probability of adsorption on the surface:

$$\alpha_{\mathrm{s,X}_i} = \frac{J_{\mathrm{ads,X}_i}}{J_{\mathrm{coll,X}_i}} \,. \tag{2.40}$$

Thus, $J_{\mathrm{ads,X}_i}$ can be expressed as

$$J_{\mathrm{ads,X}_i} = \alpha_{\mathrm{s,X}_i} J_{\mathrm{coll,X}_i} = \alpha_{\mathrm{s,X}_i} \frac{\omega_{\mathrm{X}_i}}{4} [\mathrm{X}_i]_{\mathrm{gs}} \,. \tag{2.41}$$

In case of competitive co-adsorption of several gas-phase species, the accommodation coefficient of the individual species, $\alpha_{\mathrm{s,X}_i}$, can be derived using a *Langmuir adsorption* model in which all adsorbate species compete for a single sorption site on the quasi-static surface, such that

$$\alpha_{\mathrm{s,X}_i} = \alpha_{\mathrm{s,0,X}_i}(1 - \theta_{\mathrm{s}}) \,, \tag{2.42}$$

where $\alpha_{\mathrm{s,0,X}_i}$ is the surface accommodation coefficient on an adsorbate-free surface. θ_{s} is the sorption layer surface coverage which is given by the sum of fractional surface coverages of all competing adsorbate species, $\theta_{\mathrm{s,X}_p}$:

$$\theta_{\mathrm{s}} = \sum_p \theta_{\mathrm{s,X}_p} \,, \tag{2.43}$$

where the fractional surface coverage depends on the surface concentration of

the adsorbate species X_p, $[X_p]_s$, and its effective molecular cross section, σ_{s,X_p}, which corresponds to the inverse of the species' maximum surface concentration in the sorption layer, $[X_p]_{s,max}$:

$$\theta_{s,X_p} = [X_p]_s / [X_p]_{s,max} = \sigma_{s,X_p} [X_p]_s \ . \tag{2.44}$$

The desorption flux of species X_i can be quantified by the ratio between this species' surface concentration $[X_i]_s$ and its desorption lifetime τ_{d,X_i} which is the mean residence time of the species on the surface:

$$J_{des,X_i} = [X_i]_s / \tau_{d,X_i} \ . \tag{2.45}$$

By combining equations (2.27) and (2.36) to (2.45), the net uptake coefficient of species X_i can be written as

$$\gamma_{net,X_i} = \frac{\frac{1}{4}\alpha_{s,0,X_i}\omega_{X_i}[X_i]_{gs}(1 - \sum_p \sigma_{s,X_p}[X_p]_s) - \frac{[X_i]_s}{\tau_{d,X_i}}}{\frac{1}{4}\omega_{X_i}[X_i]_{gs}} \ . \tag{2.46}$$

Equation (2.46) shows that the uptake coefficient derived according to Pöschl et al. [12] depends on the parameters of the adsorbing species such as the accommodation coefficient $\alpha_{s,0,X_i}$, the effective molecular cross section σ_{s,X_p}, the mean molecular velocity ω_{X_i}, the desorption lifetime τ_{d,X_i}, but also on its surface and gas-phase concentrations $[X_i]_s$ and $[X_i]_{gs}$, which can be affected by transport and chemical reactions. Therefore, equation (2.46) expresses γ_{X_i} as a dynamic uptake coefficient when changes in $[X_i]_s$ and $[X_i]_{gs}$ are taken into account.

$[X_i]_{gs}$ can change due to gas-phase reactions as outlined in section 2.4.1 and 2.4.2. Additionally, direct reactions between gas-phase species and surface components in the quasi-static surface layers, as illustrated in Figure 2.7, can influence the adsorbent's gas-phase concentrations.

The adsorbent's surface concentration $[X_i]_s$ can change due to surface reactions that, after adsorption, can be described by Langmuir-Hinshelwood surface reactions.

Langmuir-Hinshelwood Surface Reactions

As described in section 2.3, a two-step kinetic process consisting of fast initial uptake followed by a slower uptake regime was observed for the adsorption of NO_2 [21, 33, 67–69], O_3 [62–64], and for the co-adsorption of H_2O and O_3 on soot [60]. The surface reactions observed in these experiments were explained by and are consistent with a *Langmuir-Hinshelwood* reaction mech-

anism, which resolves the two-step kinetic process as initial adsorption, which can be competitive when multiple adsorbing species are present and is then called *Langmuir adsorption*, followed by surface reactions among adsorbents or other components on the surface. Since the same kinetic characteristics could be observed in other heterogeneous chemistry studies [85–89], it was concluded that the Langmuir-Hinshelwood mechanism is the general reaction pathway for surface reactions on aerosols [90].

Within the PRA framework, Langmuir-Hinshelwood surface reactions are parametrized by a double-layer surface model as shown in Figure 2.7 (right): Gas-phase species $\mathrm{X}_i(\mathrm{g})$ adsorb onto the sorption layer, quantified by the adsorption flux J_{ads}. Adsorbed species $\mathrm{X}_i(\mathrm{s})$ can then either desorb, expressed by the desorption flux J_{des}, or react with non-volatile particle components $\mathrm{Y}_i(\mathrm{ss})$ from the quasi-static surface layer, which is indicated by a second-order rate coefficient k_{SLR}.

The net chemical production of surface species under the assumption that the surface reactions take place between adsorbed species in the sorption layer, $\mathrm{X}_p(\mathrm{s})$, and surface components in the quasi-static surface layer, $\mathrm{Y}_q(\mathrm{ss})$, and that the product of these reactions is a surface component residing within the quasi-static surface layer, $\mathrm{Y}_i(\mathrm{ss})$, can be expressed, in analogy to the generalized rate equation (2.19), by

$$\frac{\mathrm{d}}{\mathrm{dt}}[\mathrm{Y}_i]_{\mathrm{ss}} = \sum_v \sum_p \sum_q c_{\mathrm{SLR}v,\mathrm{s},\mathrm{Y}_i} k_{\mathrm{SLR}v,\mathrm{X}_p,\mathrm{Y}_i} [\mathrm{X}_p]_{\mathrm{s}} [\mathrm{Y}_q]_{\mathrm{ss}} \ , \tag{2.47}$$

where v numbers the rate equation, p and q number the reactants, c_{SLR} are negative or positive stoichiometric coefficients, and k_{SLR} are second-order rate coefficients.

The loss of sorption layer species X_i due to surface reactions, which alongside adsorption and desorption contributes to the total production of adsorbents in the sorption layer, is a subset of equation (2.47) with the reactant summation index variable p fixed to species X_i:

$$L_{\mathrm{s,ss},\mathrm{X}_i} = \sum_v \sum_q c_{\mathrm{SLR}v,\mathrm{s},\mathrm{X}_i} k_{\mathrm{SLR}v,\mathrm{X}_i,\mathrm{Y}_i} [\mathrm{X}_i]_{\mathrm{s}} [\mathrm{Y}_q]_{\mathrm{ss}} \ , \tag{2.48}$$

$$\frac{\mathrm{d}}{\mathrm{dt}}[\mathrm{X}_i]_{\mathrm{s}} = J_{\mathrm{ads},\mathrm{X}_i} - J_{\mathrm{des},\mathrm{X}_i} - L_{\mathrm{s,ss},\mathrm{X}_i} \ , \tag{2.49}$$

where $J_{\mathrm{ads},\mathrm{X}_i}$ and $J_{\mathrm{des},\mathrm{X}_i}$ are the adsorption and desorption fluxes, respectively, as defined in (2.41) and (2.45) in section 2.4.3.

The gas-phase uptake with subsequent Langmuir-Hinshelwood surface reactions is now fully determined by the set of differential equation consisting

of the net surface production (2.49), the net gas-phase production (2.19), and the net gas-phase loss (2.28), which are related to each other by the expression for the net uptake coefficient (2.46).

These differential equations have to be solved simultaneously to completely model the gas-phase uptake with subsequent surface reactions. Depending on the exact chemical pathway of the specific heterogeneous reaction, other differential equations, such as for direct reactions between the gas phase and the condensed phase, as well as for bulk diffusion processes and reactions, need to be taken into account.

In atmospheric models, the chemical differential equations are solved numerically, as will be described in the next section.

2.5 Atmospheric Models

Atmospheric models are developed to understand and predict the relationship between emissions, reactions, and concentrations of primary and secondary pollutants. In general, the major components of an atmospheric model are: (1) emissions of the primary pollutants; (2) meteorological and topographical features, such as temperature, relative humidity, wind speed and direction, inversion height, and other terrain features; and (3) the chemistry.

2.5.1 Chemical Component

The chemistry in an atmospheric model is represented by chemical rate equations, such as equations (2.19), which are a system of coupled, non-linear differential equations. In order to predict the temporal evolution of the chemical species' concentrations, the differential equations need to be solved simultaneously.

A simple explicit solution method for ordinary differential equation is the forward Euler method [91], which uses the formula

$$y_{(n+1)} = y_n + hf(x_n, y_n)\,, \tag{2.50}$$

to advance a solution by a step length h, from x_n to $x_{(n+1)} = x_{n+h}$. In this method, the difference quotient is evaluated at the beginning of the interval:

$$f(x_n, y_n) = \frac{y(t+h) - y(t)}{h}\,. \tag{2.51}$$

Chemical rate equations commonly have a high degree of *stiffness*, which is the ratio between the largest and the smallest Eigenvalue of the system of

equations to be solved. The stiffness can amount as much as 10^{10} for chemical rate equations. This demands a small time step for simple explicit solution methods, such as the Euler forward method. Since this would be computationally very inefficient, other solution algorithms are used in these cases.

A standard solution method for the equations of chemical kinetics is the Gear algorithm [92], which is a robust and accurate, multistep, variable order numerical scheme [93]. Multistep and variable order mean that not only values from one order n are used to compute the value at $n+1$, but that the solution depends on s more past values:

$$\begin{aligned} & y_{n+s} + a_{s-1}y_{n+s-1} + a_{s-2}y_{n+s-2} + ... + a_0 y_n \\ & = h[b_s f(x_{n+s}, y_{n+s}) + b_{s-1} f(x_{n+s-1}, y_{n+s-1}) + ... + b_0 f(x_n, y_n)] \,, \end{aligned} \tag{2.52}$$

where the a's and the b's are coefficients.

The dependence on multiple steps makes multistep methods more accurate than one-order methods. However, these methods are also slower than one-order methods, since they require the storing of multiple previous values of concentrations of each species.

Chemical Representation

The explicit representation of atmospheric chemistry can be very extensive with respect to the number of differential equations that need to be solved. For example, the oxidation of just one organic species in air, contributing to the formation of ground-level O_3 by reactions (2.4) to (2.6), can include hundreds of reactions [94]. The Master Chemical Mechanism (MCMv3) [95], which is a near-explicit chemical mechanism describing the tropospheric degradation of 124 VOCs and the associated inorganic chemistry, contains in excess of 12,600 reactions and 4,500 chemical species. When also meteorological conditions and emissions need to be taken into account, such explicit chemical approaches in combination with multistep schemes become quickly unmanageable and computational expensive.

As a result, the chemical mechanisms of most models are condensed in various ways by lumping together several organic species and reactions [95, 96]. Two main approaches have been followed so far. The first approach groups organics by their traditional classifications, e.g., alkanes, alkenes, aromatics, sometimes with some exceptions when members of that group are much more reactive than others. Two examples of models utilizing this approach are the Lurman-Carter-Coyner (LCC) mechanism [97] and the Regional Acid Deposition Model (RADM) [13]. The second approach, the so-called "carbon bond mechanism", groups organics in terms of their chemical bonding [98].

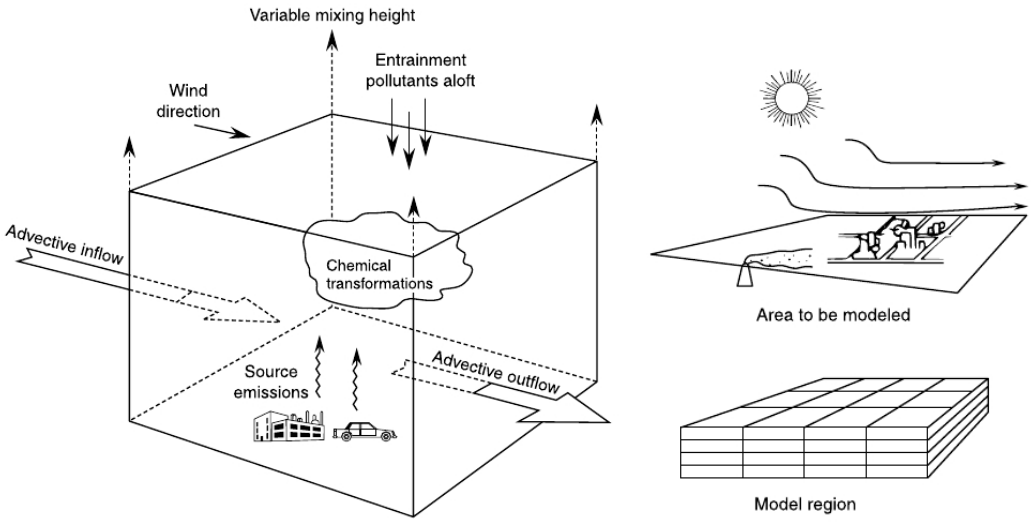

Figure 2.8: Schematic diagram showing basic elements of a box model (left) and a grid model's representation of an area to be modeled. Adapted from Finlayson-Pitts and Pitts [2].

Model intercomparisons show generally good agreement between the models for the major species O_3 and NO_x [99, 100]. However, the discrepancies can be larger for trace species, such as H_2O_2 and HCHO.

Before chemical submodels, such as a VOC chemical model, are incoporated into comprehensive models, they are tested against environmental chamber experiments [e. g. 13]. The comprehensive models, which include complex meteorology and may have a spatial resolution that incorporates terrain-features, can be tested against field campaigns [e. g. 101].

2.5.2 Spatial Categorization

With regards to spatial resolution, models can be classified into box models, Lagrangian models, and grid models. In a *box model*, whose basic elements are shown in Figure 2.8 (left), the airshed, i.e., a given volume of atmospheric air in a geographical region, is in the shape of a box. It is based on the assumption that the air pollutants inside the box are homogeneously distributed to estimate the average pollutant concentrations anywhere within the airshed. It may include advective in- and outflow. Although it does not fully resolve topographic features and complex meteorology, box models are being used to represent landscapes with simple topographies [102, 103]. They are also often used as a first approach to incorporating and testing new chemical sub-

modules [104]. A *Langrangian model* is a series of adjacent, interconnected boxes that follow the trajectory of an air pollution parcel. If the frame of reference does not move with the air parcel, the model is called an (Eulerian) *grid model*. These are the models currently used for making concrete, terrain-specific, predictions. As Figure 2.8 (right) illustrates, grid models divide an area horizontally and vertically into grids (or boxes) which are interconnected by transport processes. The horizontal size of each grid, as well as its number can vary, depending on the purpose of the model. There are also nested approaches which nest urban-scale grids into larger regional-scale grids [105].

Frequently when chemical kinetics are being tested, simple models parametrizing only the investigated chemical species are being used as first estimates [33, 72].

2.5.3 Heterogeneous Chemistry in Models

Particles are represented in atmospheric models in several ways. Some models focus on predicting aerosol mass concentrations, which is motivated by correlations of respiratory disease with aerosol mass burden [106]. These models resolve particles in size bins and include physical processes, such as nucleation, coagulation, condensation, and evaporation. The condensation of gas-phase species onto the particles is usually treated by assuming a gas-particle equilibrium without accounting for surface reactions [107–109].

Other models investigate the influence that heterogeneous reactions have on the gas-phase composition, in particular on the gaseous air pollutants O_3 and NO_x. This is done by integrating equation (2.28) into the models' numerical solvers. The physiochemical processes on the surface or in the bulk of the particle are also mostly assumed to be in equilibrium, which corresponds to the resistor model described in section 2.4.3 and the use of constant uptake coefficients.

In the following, findings of the model investigations involving heterogeneous reactions on soot are reviewed.

Review of Previous Heterogeneous Model Studies

As described in section 2.3, several laboratory studies observed the production of HONO by heterogeneous reactions of NO_2 with soot particles [33, 68, 71, 72]. These heterogeneous reactions were suggested to be an important HONO source, since the observed HONO concentrations cannot be explained by gas-phase production only [110, 111]. By producing HONO, the heterogeneous reactions also have an influence on the O_3 concentration via the photolysis to NO and OH and the subsequent oxidation to NO_2, as described in section 2.3.

For these reasons, several model studies investigated the HONO production by heterogeneous reactions of NO_2 with soot.

Kotamarthi et al. [112] performed a series of box model calculations to test the model's NO_x sensitivity to a number of reactions on soot surfaces, including HONO production analogous to reaction (2.10). Besides this, also a reaction of ammonium bisulfate to HNO_3, as in reaction (2.9), was incorporated. The calculations suggest that the conversion of NO_2 to HONO on particle surfaces produces a large, measurable signal, up to several parts per billion (ppbv), in nighttime HONO mixing ratios. According to the simulations, this results in a decrease in the gas-phase O_3 concentration of 20 ppbv and 8 ppbv respectively, depending on the value of the NO_2 uptake coefficient, which was either 3.3×10^{-4} or 0.01.

In contrast, a model study by Aumont et al. [110] that, in contrast to Kotamarthi et al. [112], took into account depositional losses of HONO and deactivation of the soot as a result of NO_2 processing, observed no significant influence of reaction (2.10) on the OH and O_3 concentrations. Subsequently, the assumed soot deactivation by NO_2 processing was observed in the laboratory, e.g., by Lelievre et al. [113] and Aubin and Abbatt [72]. Also other estimates of the HONO formation potential that took into account surface saturation effects agree with the result of Aumont et al. [110] [33, 72]. Additionally, a numerical simulation with a comprehensive mesoscale model system implied that reactions on aerosol surfaces are a negligible source of HONO and that heterogeneous reactions at the ground and direct emissions are the most important currently identified sources [114].

As described in section 2.3, several other gas-phase species besides NO_2 can be involved in heterogeneous reactions with soot. Their effect was investigated in model studies as well. For example, Saathoff et al. [21] fitted aerosol chamber data to box model simulations to investigate the heterogeneous loss of NO_2, HNO_3, NO_3/N_2O_5, and HO_2/HO_2NO_2 on soot. It was found that these heterogeneous reactions had a minor impact on the O_3 concentration when NO_x emissions were low, but caused a decrease in O_3 up to 10% when NO_x emission were high. The HO_2 uptake was responsible for 7% out of the 10%. However, the authors suggested that the impact of soot on atmospheric chemistry is likely to be small and perhaps negligible, since transport, deposition, and dilution processes were not taken into account in the modeling study and high soot surface concentrations and uptake coefficients were used.

Aklilu and Michelangeli [115] used a box model simulation to investigate the effects of heterogeneous reactions on soot in an air parcel passing over an urban area and traveling downwind. Taking into account the consumption of soot surface sites, the heterogeneous reactions of O_3, HNO_3, NO_2, NO_3, and

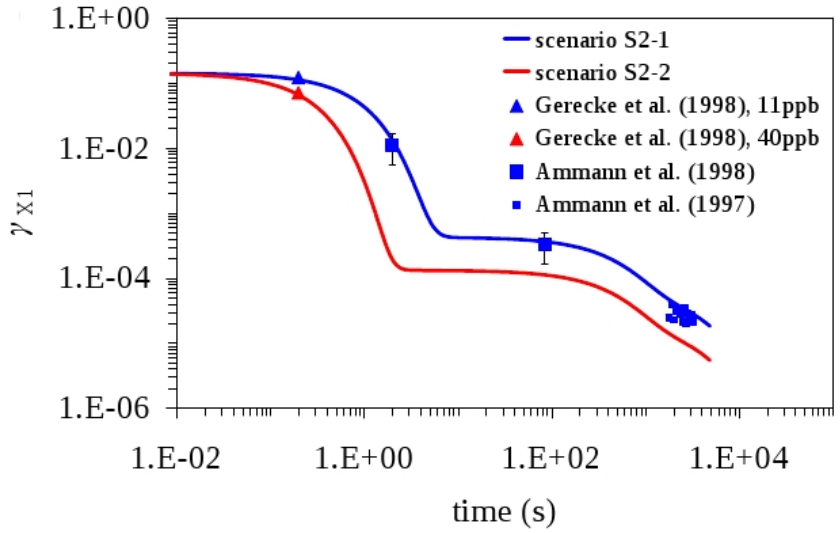

Figure 2.9: Temporal evolution of the NO_2 uptake coefficient, modeled to fit uptake coefficient values measured by Ammann et al. [68], Gerecke et al. [71], Ammann et al. [116]. Specifications and input parameters for scenarios S2-1 and S2-2 are given in Ammann and Pöschl [117]. Adapted from Ammann and Pöschl [117].

N_2O_5 with soot particles resulted in a maximum O_3 reduction of 7 ppbv (about 25%) downwind of the urban center.

The results of the model studies presented above show that heterogeneous reactions potentially play a role in influencing the concentrations of gaseous air pollutants in the troposphere. However, it also becomes clear that the atmospheric model studies depend crucially on the parameters and reaction mechanisms they employ. A major uncertainty is associated with the adapted uptake coefficients. The span of measured uptake coefficients on soot surfaces of various kinds ranges seven orders of magnitude, from 10^{-8} to 10^{-1}, for NO_2 uptake [72], and four orders of magnitude, from 10^{-3} to 10^{-7}, for O_3 uptake [63].

The modeling results also depend on the way heterogeneous reactions are represented in the model. While simple equilibrium parametrizations with constant uptake coefficients are computationally efficient, they ignore the underlying physical processes and therefore may result in erroneous projections. This was, for example, the case for the study by Kotamarthi et al. [112] which did not take soot surface passivation into account.

As discussed in section 2.4.3, the PRA kinetic framework for aerosol surface chemistry and gas-particle interactions takes into account the underlying

physical picture with its flux-based formulation of the uptake process and mass balances. Ammann and Pöschl [117] showed in kinetic model investigations using the PRA framework that the uptake coefficient decreases with time due to surface saturation effects [117]. Thus, different measured uptake coefficients for the same model substance can be reconciled when aligning the values according to the time scales of the measurements. An example for the uptake coefficients measured in NO_2 uptake experiments is shown in Figure 2.9, where the temporal evolution of the NO_2 uptake coefficient was modeled to fit the different uptake values measured by Ammann et al. [68, 116] and Gerecke et al. [71].

The absence of atmospheric model simulations which fully resolve the underlying physiochemical processes that govern heterogeneous reactions is one motivation for the study presented here.

2.6 Motivation for Modeling Study

The focus of this paper is to determine how heterogeneous reactions change the aerosol surface composition and affect the gas-phase concentrations of air pollutants in a polluted urban environment. The specific heterogeneous reactions that will be focused on are the reversible co-adsorption of O_3, NO_2, and water vapor on soot particles coated with the polycyclic aromatic hydrocarbon benzo[a]pyrene (BaP) in an urban pollution scenario.

2.6.1 Motivation and Relevance

The studied model substances are of high relevance with respect to public health and the environment, as BaP is classified as a "probable human carcinogen" [118] and the trace gases O_3 and NO_2 are major criteria air pollutants [119] as was outlined in section 2.1 and 2.2.

Sections 2.3 and 2.4.3 showed that the heterogeneous reactions between the model substances and soot follow two-step Langmuir-Hinshelwood type surface reactions, which have a direct effect on the uptake process by inducing variations in the uptake coefficient via equation (2.46). However, as discussed in section 2.5.3, current atmospheric models commonly parametrize the uptake process by constant uptake coefficients or coarse parametrizations that do not take dynamic changes in the uptake kinetics into account [14, 15, 115, 120, 121]. This can lead to erroneous results. This study addresses this shortcoming by resolving the physiochemical processes that determine the uptake process and surface reactions with the PRA framework for gas-particle interactions and surface chemistry [12], as described in section 2.4.3.

Previous modeling studies employing the PRA framework were so far limited to kinetic modeling exercises [117] that considered only one adsorbent at a time without simulating a dynamic atmospheric context. However, the uptake coefficient, as given in equation (2.46), explicitly depends on the adsorbent's gas-phase concentration which generally undergoes diurnal changes in the atmosphere, as described in section 2.1. To address this shortcoming, this study implements the heterogeneous kinetics parametrized by the PRA framework into the gas-phase solver RADM2 (Second Generation Regional Acid Deposition Model) [13], which is a well-established, nonlinear chemical gas-phase mechanism for modeling atmospheric chemistry on a regional scale. It can simulate diurnal changes in photolysis frequencies and gas-phase emissions and can therefore be used to study heterogeneous reactions in a realistic atmospheric environment. Since this study focuses on air pollutants, RADM2 is initialized with gas-phase concentrations and emissions characteristic for an urban pollution scenario.

With this coupled RADM2-PRA framework, the effects of heterogeneous reactions on the particle surface and gas-phase composition can be studied in a realistic atmospheric environment and under consideration of the underlying physiochemical processes. The adaptation of a polluted urban environment as context for the heterogeneous reactions allows to investigate the importance of heterogeneous reactions for urban air pollution, in particular for the concentrations of the major air pollutants O_3 and NO_2. With respect to laboratory studies, the detail with which the surface chemistry can be modeled using this framework exceeds the complexity of current laboratory experiments which consider two adsorbents at most without a dynamic atmospheric context. Therefore this study can provide valuable information for the conception of new experiments. This is the first time that such detailed heterogeneous chemistry is evaluated in an atmospheric environment.

2.6.2 Limitations

The scope of this study is conceptual and therefore relies on some simplifications:

This study focuses on three adsorbents. However, as the experimental studies reviewed in section 2.3 show, other gas-phase species, such as HO_2 and NO_3 can also adsorb onto soot surfaces [21, 77, 78]. Moreover, under realistic atmospheric conditions, one can expect even more chemical species, such as other PAHs and different trace gases, to adsorb on, or react with, soot. This study limits the number of adsorbents to three to assess each adsorbent's influence in detail. The determination of simple cause-effect relationships with a higher number of adsorbents would be very complex, without necessarily

providing more insights. It is assumed that atmospheric oxidation is well represented by the major oxidants, which include the here-considered O_3. Other very reactive gases, such as OH and NO_3, have not been shown to adhere to Langmuir adsorption kinetics with subsequent surface reactions. These gases are not included in this study to avoid the mixing of conceptual frameworks.

By using the PRA model framework, this study limits the the maximum adsorbents' surface coverage to one monolayer. Therefore, diffusion processes through multiple surface layers, such as multiple layers of water, are not considered in the model framework. However, limiting the total adsorbents' surface coverage to one monolayer allows treating the uptake of gas-phase species according to Langmuir adsorption kinetics, which was the experimentally determined reaction mechanism for the chemical species considered in this study [e. g. 33, 60].

To reduce complexity, this study does not take into account the changes in particle composition and mass due to coagulation, dilution, and condensation of semi-volatile gas-phase species.

Finally, this study uses as input parameters realistic values characteristic of an urban pollution scenario and uptake parameters determined by laboratory experiments. However, the purpose of this study is not to make exact atmospheric predictions, but to conceptually investigate the influence of heterogeneous reactions with soot on common polluted environments.

The next chapter discusses the this study's model approach in detail.

Chapter 3

Model approach

This study's model approach is based on the coupling of the PRA kinetic framework for aerosol chemistry and gas-particle interactions [12] to the chemical gas-phase solver RADM2 [13]. Details about the adapted PRA framework, as well as the reaction scenarios and input parameters are presented in this chapter. First, a description of the gas-phase mechanism RADM2, its solver routine, and the adapted gas-phase scenarios is given.

3.1 Gas-Phase Mechanism

The nonlinear, chemical gas-phase mechanism RADM2 [13] is widely used in atmospheric models to predict concentrations of oxidants and other air pollutants [e.g., 122, 123]. It is based on the earlier RADM1 and RADM1.0 [93, 124], as well as on several other mechanisms [97, 125, 126]. It includes 62 chemical species, 21 photolysis reactions, and 140 thermal reactions [13]. Volatile organic compounds (VOCs) are aggregated (lumped) into 15 classes of reactive organic species. It also includes one heterogeneous reaction by default: the hydrolysis of N_2O_5 as described by equation (2.9). The reaction is parametrized by equation (2.28) with a constant uptake coefficient of $\gamma_{N_2O_5} = 0.02$. (The use of constant uptake coefficient is justified for the interaction between gas-phase species and liquid particles as discussed in section 2.4.3.) The included chemical species and reactions are listed in appendix C. As suggested by Vogel et al. [114], the reaction rate for the production of HONO from NO and OH was updated to 9.7×10^{-12} cm^3 s^{-1} according to Atkinson et al. [127]. RADM2 is used in a box model version for the conceptual purpose of this study.

3.1.1 Urban Pollution Scenario

For studying the uptake process in a polluted urban environment, RADM2 is initialized with the tropospheric urban plume scenario PLUME1 according to Kuhn et al. [100]. PLUME1 was designed to represent the chemistry in the polluted boundary layer. It includes constant emissions for a variety of trace gases representative for continental European air [128], such as 0.54 pptv min^{-1} of SO_2, 2.68 pptv min^{-1} of NO, and 5.85 pptv min^{-1} of CO. Initial concentrations are set to 50 ppbv for O_3, 0.5 ppbv for NO_2, 0.2 ppbv for NO, and 20,000 ppmv for H_2O which corresponds to 64% relative humidity (RH). Time-dependent photolysis rates are parametrized by equation (2.1) with parameters based on a radiation transport model by E. P. Roeth [100]. A detailed overview of the emission rates, initial gas concentrations, and photolysis parameters is given in appendix D.

The pressure and temperature are set to 1013.25 hPa and 298 K, respectively. Note that this temperature is 10 K warmer than the temperature in the PLUME1 scenario by Kuhn et al. [100]. This is to represent typical temperatures in the summer when photochemical smog episodes are most frequent. The physical processes of deposition, particle coagulation, and dilution of trace gases and soot particles are not considered. A modeling period of five days is chosen, which is within the reported soot residence times in the atmosphere [27, 28]. The simulation period starts at 12 noon.

The numerical solution technique with which RADM2 solves the chemical differential equations is described in the next subsection.

3.1.2 Chemical Solver

As descibed in section 2.5.1, a standard solution method for the stiff differential equations of chemical kinetics is the Gear algorithm [92]. This multistep algorithm is accurate, but since it requires storing of up to six previous values of concentrations for each species, it is computationally slow. For RADM2, a more efficient but mathematically less rigorous integration technique has been developed [93].

The stiffness of the chemical differential equations is reduced by several measures. Pairs of species with large reaction rates are grouped to linear combinations and thereby removed from the system of equations. The grouped species, as well as species with very large characteristic time scales of loss reactions, are treated with the Euler forward method, which was described in section 2.5.1. Additionally, chemical species with lifetimes less than a minute are treated by local steady-state equations, which avoids solving their rate equations by numerical integration. The remaining differential equations are

then solved as follows:

The chemical rate equations can be written in a generic form as

$$\frac{d[\mathrm{X}_i]}{dt} = P_{\mathrm{X}_i}(\mathrm{X}_j) - \frac{\mathrm{X}_i}{\tau_\mathrm{c}(\mathrm{X}_j)} \,, \tag{3.1}$$

where P_{X_i} is the production term of species X_i, which is dependent on some other species X_j, and τ_c is the characteristic time scale of the loss reactions, also dependent on some other species. If P_{X_i} and τ_c are constant during a time step Δt_c, equation (3.1) has the exponential solution:

$$[\mathrm{X}_i]^{t+\Delta t_\mathrm{c}} = P_{\mathrm{X}_i}\tau_\mathrm{c} + ([\mathrm{X}_i] - P_{\mathrm{X}_i}\tau_\mathrm{c}) \exp\left(-\Delta t_\mathrm{c}/\tau_\mathrm{c}\right) \,, \tag{3.2}$$

where $[\mathrm{X}_i]^t$ is the concentration of X_i at time t and $[\mathrm{X}_i]^{t+\Delta t_\mathrm{c}}$ the concentration at time $t+\Delta t_\mathrm{c}$. The time step Δt_c is variably determined by the condition [129]:

$$\Delta t_\mathrm{c} = \min\left(\epsilon \frac{\mathrm{X}_i}{d\mathrm{X}_i/dt}\right) \,, \tag{3.3}$$

where ϵ ensures that the change in concentration stays within a pre-set limit.

This numerical method was compared to the Gear algorithm [92], which showed good agreement between both solvers, but the RADM method described above used six to ten times less computational memory and was at least five times faster [93].

An overview of the RADM2 code, outlining the way the chemical production and loss terms are supplied to the solver, is given in appendix E. The next section presents the heterogeneous reactions that were implemented into the RADM2 solver.

3.2 Heterogeneous Reactions

This study models the co-adsorption and subsequent surface reactions of O_3, NO_2, and water vapor on soot coated with BaP. Based on experiments on the adsorption and subsequent surface reaction of O_3 on soot [60, 62], and NO_2 on soot [33, 68], which were outlined in section 2.3, the heterogeneous reactions of the considered model substances can be assumed to follow a competitive Langmuir adsorption process and Langmuir-Hinshelwood surface reactions between the adsorbents and the soot surface components. As described in section 2.4.3, these heterogeneous reaction processes can be described by the PRA kinetic framework for aerosol chemistry and gas-particle interactions [12]. The PRA framework's flux-based formulation of the uptake process led to expression

(2.46) for describing the uptake kinetics. This equation shows dependencies on the adsorbent's gas-phase and surface concentrations. While the gas-phase processes affecting the uptake were illustrated in sections 2.1 and 2.4.1 and their model implementation was outlined above, this section describes the implemented surface reaction scenarios.

3.2.1 Surface Reactions

Three reaction scenarios are defined to investigate the effect that the co-adsorption of O_3, NO_2, and water vapor has on the soot surface composition and the gas phase: the adsorption of O_3 in *Scenario A*, the co-adsorption of O_3 and NO_2 in *Scenario B*, and the co-adsorption of O_3, NO_2, and water vapor in *Scenario C*. Up to five surface reactions, depending on the scenario, are simulated. An overview is given in Table 3.1. It should be noted that experimentally determined initial uptake coefficients are implemented as accommodation coefficients in accord to Ammann and Pöschl [117]. This approach is justified, since initially $\gamma_{\mathrm{X}i} = \alpha_{\mathrm{s,0,X}i}$, as can be seen from equation (2.46). In the following, the reaction pathway of each adsorbent and the input parameters are discussed.

O_3 Adsorbed O_3 can participate in three surface reactions, which convert the soot-coating BaP into generic chemical derivatives Y2, Y3, and Y4. These derivatives are meant to represent the three major reaction products identified in ozonolysis experiments of soot coated with BaP [59] and can be pictured as BaP derivatives with an increasing number of oxygenated functional groups and decreasing reactivity towards photo-oxidants such as BaP-quinones, hydroxy-ketones, acid anhydrides, lactones, etc. [59, 131–133]. Their decreasing reactivity was modeled by Ammann and Pöschl [117] with decreasing reaction rates, k_{SLR1} to k_{SLR3}, as given in Table 3.1. Scenario A, in which only O_3 adsorbs and reacts on the soot surface is adapted from their Model System Solid 1 [117], with the exception that in this study the atmospheric context is simulated by the coupling to RADM2. The reaction rate k_{SLR1} and the O_3 specific parameters $\alpha_{\mathrm{s,0,O_3}}$, $\sigma_{\mathrm{O_3}}$, $\tau_{\mathrm{d,O_3}}$ are adapted from results of the ozonolysis experiment by Pöschl et al. [60], which used an aerosol flow tube apparatus at ambient temperature and pressure.

NO_2 Adsorbed NO_2 is modeled to convert the BaP derivatives Y2 and Y3 to another surface component, Y5, and HONO that desorbs to the gas phase. As mentioned in section 2.3, the possible important desorption of HONO received much experimental investigation [e.g., 68, 72], but less is known about

Table 3.1: Adsorbents, surface reactions, reaction rates, and parameters (accommodation coefficient (α), effective molecular cross section (σ), desorption time (τ)) applied in model scenarios A, B, C.

Scenario	Adsorbants	Surface reactions
A	O_3	(1) O_3(s) + BaP(ss) → Y2(ss) (2) O_3(s) + Y2(ss) → Y3(ss) (3) O_3(s) + Y3(ss) → Y4(ss)
B	O_3, NO_2	(1) to (3) (4) NO_2(s) + Y2(ss) → Y5(ss) (5) NO_2(s) + Y3(ss) → HONO(g)
C	O_3, NO_2, H_2O	(1) to (5)
Scenario	**Reaction rates [$cm^2\ s^{-1}$]**	**Parameters**
A	$k_{SLR1} = 2.1 \times 10^{-17}$ [60, 117] $k_{SLR2} = 2.1 \times 10^{-19}$ [117] $k_{SLR3} = 2.1 \times 10^{-21}$ [117]	$\alpha_{s,0,O_3} = 1 \times 10^{-3}$ [60, 65, 117] $\sigma_{O_3} = 1.8 \times 10^{-15}$ cm^2 [60, 117] $\tau_{d,O_3} = 18$ s [60, 117]
B	k_{SLR1} to k_{SLR3} $k_{SLR4} = 7 \times 10^{-18}$ [117] $k_{SLR5} = 7.5 \times 10^{-21}$ [116, 117]	$\alpha_{s,0,NO_2} = 0.14$ [71, 117] $\sigma_{NO_2} = 3 \times 10^{-15}$ cm^2 [116, 117] $\tau_{d,NO_2} = 18$ s [116, 117]
C	k_{SLR1} to k_{SLR5}	$\alpha_{s,0,H_2O} = 0.4 \times 10^{-3}$ [60, 67] $\sigma_{H_2O} = 1.08 \times 10^{-15}$ cm^2 [130] $\tau_{d,H_2O} = 3 \times 10^{-3}$ s [60]

the exact reaction pathways. Besides the HONO producing reaction, Kirchner et al. [70] identified several possible reactions with, e.g., OH groups on the soot surface. These OH groups are present as functional groups on soot surfaces, but can also be pictured as a results of a reaction with O_3 in the presence of small humidity levels. Since it was shown that small humidity levels are enough for the HONO formation to proceed [71], the influence of water vapor was not parametrized within the modeled reactions. The two-reaction pathway of NO_2 on soot was adapted from Model System Solid 2 [117], which was used to reconcile short-term and long-term experimental results of NO_2-soot experiments obtained by Ammann et al. [68, 116] and Gerecke et al. [71]. Input parameters are based on these experiments, which were conducted with a

Knudsen cell apparatus [71], an aerosol flow reactor [68], and by filter deposition [116]. The reaction rate coefficient for surface reaction (4), k_{SLR4}, was adjusted by Ammann and Pöschl [117] to fit the experimental data. Model System Solid 2 was changed for this study to include the desorption of HONO with a reaction rate adapted from Ammann et al. [68].

H_2O The co-adsorption with water vapor was modeled to be without additional surface reactions. This was suggested by an ozonolysis experiment conducted by Pöschl et al. [60] on the basis that fresh soot is known to be hydrophobic and that the detected O_3 loss displayed a behavior compatible with competitive Langmuir adsorption of O_3 and H_2O. The H_2O specific parameters $\alpha_{\mathrm{s,0,H_2O}}$ and $\tau_{\mathrm{d,H_2O}}$ are adapted from carbon hydration experiments by Rogaski et al. [67] and from experiments investigating the interaction of O_3 and H_2O on soot by Pöschl et al. [60]; $\sigma_{\mathrm{H_2O}}$ is adapted from results of H_2O adsorption experiments by Nishino [130].

Surface Kinetics

The rate equations for the loss of adsorbents through surface reactions are described by equation (2.49) in section 2.4.3. Adapted for the surface reactions considered here, these rate equations are:

$$\begin{aligned} L_{\mathrm{s,ss,O_3}} &= k_{\mathrm{SLR1}}[\mathrm{O_3}]_{\mathrm{s}}[\mathrm{BaP}]_{\mathrm{ss}} + k_{\mathrm{SLR2}}[\mathrm{O_3}]_{\mathrm{s}}[\mathrm{Y2}]_{\mathrm{ss}} \\ &+ k_{\mathrm{SLR3}}[\mathrm{O_3}]_{\mathrm{s}}[\mathrm{Y3}]_{\mathrm{ss}} \,, \qquad (3.4) \\ L_{\mathrm{s,ss,NO_2}} &= k_{\mathrm{SLR4}}[\mathrm{NO_2}]_{\mathrm{s}}[\mathrm{Y2}]_{\mathrm{ss}} + k_{\mathrm{SLR5}}[\mathrm{NO_2}]_{\mathrm{s}}[\mathrm{Y3}]_{\mathrm{ss}} \,. \qquad (3.5) \end{aligned}$$

The concentrations of the surface components BaP, Y2 to Y5 are determined by their reactions with the following rate equations, according to equation (2.47):

$$\begin{aligned} \frac{d[\mathrm{BaP}]_{\mathrm{ss}}}{dt} &= -k_{\mathrm{SLR1}}[\mathrm{O_3}]_{\mathrm{s}}[\mathrm{BaP}]_{\mathrm{ss}} \,, \qquad (3.6) \\ \frac{d[\mathrm{Y2}]_{\mathrm{ss}}}{dt} &= k_{\mathrm{SLR1}}[\mathrm{O_3}]_{\mathrm{s}}[\mathrm{BaP}]_{\mathrm{ss}} - k_{\mathrm{SLR2}}[\mathrm{O_3}]_{\mathrm{s}}[\mathrm{Y2}]_{\mathrm{ss}} \\ &- k_{\mathrm{SLR4}}[\mathrm{NO_2}]_{\mathrm{s}}[\mathrm{Y2}]_{\mathrm{ss}} \,, \qquad (3.7) \\ \frac{d[\mathrm{Y3}]_{\mathrm{ss}}}{dt} &= k_{\mathrm{SLR1}}[\mathrm{O_3}]_{\mathrm{s}}[\mathrm{Y2}]_{\mathrm{ss}} - k_{\mathrm{SLR2}}[\mathrm{O_3}]_{\mathrm{s}}[\mathrm{Y3}]_{\mathrm{ss}} \\ &- k_{\mathrm{SLR5}}[\mathrm{NO_2}]_{\mathrm{s}}[\mathrm{Y3}]_{\mathrm{ss}} \,, \qquad (3.8) \end{aligned}$$

$$\frac{d[\mathrm{Y4}]_{\mathrm{ss}}}{dt} = k_{\mathrm{SLR3}}[\mathrm{O_3}]_{\mathrm{s}}[\mathrm{Y3}]_{\mathrm{ss}} \,, \tag{3.9}$$

$$\frac{d[\mathrm{Y5}]_{\mathrm{ss}}}{dt} = k_{\mathrm{SLR4}}[\mathrm{NO_2}]_{\mathrm{s}}[\mathrm{Y2}]_{\mathrm{ss}} \,. \tag{3.10}$$

The overall loss of adsorbents on the surface is given by equation (2.49), which contains, in addition to the loss through surface reactions, the loss through desorption from the surface and the production through adsorption onto the surface. The respective fluxes are determined by equation (2.41) and (2.45) with X_i replaced by $\mathrm{O_3}$ and $\mathrm{NO_2}$, respectively. The adsorption flux depends on the sorption layer surface coverage, which for the co-adsorption of $\mathrm{O_3}$, $\mathrm{NO_2}$, and water vapor is given by

$$\theta_{\mathrm{s}} = \sigma_{\mathrm{s,O_3}}[\mathrm{O_3}]_{\mathrm{s}} + \sigma_{\mathrm{s,NO_2}}[\mathrm{NO_2}]_{\mathrm{s}} + \sigma_{\mathrm{s,H_2O}}[\mathrm{H_2O}]_{\mathrm{s}} \,, \tag{3.11}$$

where the fractional sorption layer coverages are given by the product of the respective effective molecular cross section on the surface, σ_{s}, and the concentration of the adsorbent in the sorption layer.

Together with the expression for the collision flux, (2.27), the uptake coefficient can be determined according to equation (2.36). With that, the net gas-phase loss of the specific adsorbent can be calculated according to equation (2.28).

The PRA framework outlined in this chapter is coupled to the chemical gas-phase solver RADM2. This is done by integrating the described reaction kinetics into the chemical solver routine of the RADM2 mechanism. An excerpt of the integrated FORTRAN-code is given in appendix E.2.

3.2.2 Soot Concentration

As the surface kinetics above show, soot does not take part directly in the surface reactions. The way soot is incorporated in the model is by means of its particle surface concentration in air, which is an input parameter for equation (2.28). The surface concentration can be calculated from the mass concentration and the surface area per mass. The mass concentration for soot in polluted environments is about 10 µg $\mathrm{m^{-3}}$ in air [16]. The soot surface area per mass can vary, depending on the type of soot, from 6 $\mathrm{m^2\,g^{-1}}$ for aircraft engine combustor soot [37] to approximately 500 $\mathrm{m^2\,g^{-1}}$ for the post-treated black carbon Degussa FW2 [38]. This study adapts a surface area of 500 $\mathrm{m^2\,g^{-1}}$. This corresponds to values that have been used in laboratory studies [e.g., 63, 134, 135]. However, since this value is at the upper end, it may result in an upper limit for the concentration of surface reaction sites.

Multiplying the surface per mass value by the soot mass concentration yields a total soot surface concentration of $[\mathrm{PS}]_\mathrm{g} = 5 \times 10^{-5}$ cm^2 cm^{-3}. It should be noted that this value does not necessarily represent an upper limit, since soot mass concentrations which are double the amount used for this calculation have been measured in polluted urban environments [16].

The overall soot production and loss in the box model are assumed to be in equilibrium and therefore the soot surface concentration $[\mathrm{PS}]_\mathrm{g}$ is kept constant. The surface composition is changing with time due to the described surface reactions, which is referred to as chemical "aging" and assessed by the reactions scenarios A, B, and C.

Since the surface coverage of soot particles increases with the adsorption of gas-phase species, "aged" particles are less reactive than freshly emitted ones. However, in polluted environments, fresh soot is emitted continuously by a variety of sources, such as car traffic and coal-fired power plants [2, 136]. Two additional soot emission scenarios, which are described in the next subsection, are adapted as a sensitivity study to estimate the effect of soot emissions on the gas phase.

3.2.3 Soot Emission Scenarios

The emission of fresh soot in this box model study is approximated by resetting the soot surface to its initial condition with a BaP surface concentration of $[\mathrm{BaP}] = 1 \times 10^{14}$ cm^{-2} and no secondary surface components. At this point in the simulation, the existing population of soot with the residual BaP concentration and higher order surface components is discarded. While the number of reactive surface sites changes to account for the effect of soot emissions on chemical reactions, the soot surface concentration $[\mathrm{PS}]_\mathrm{g}$ is kept constant and physical processes, such as coagulation, deposition, and dilution of the soot particles are neglected.

The BaP surface concentration on soot is replenished according to two scenarios. In a low emission scenario, the reactive surface is replenished every six hours, and in a high emission scenario, it is replenished every hour. The error from neglecting gas-phase uptake on discarded populations for these replenishing times will be assessed in the next chapter.

Although the soot surface concentration is kept constant, the replenishing times can be expressed as hourly emission rates, R_emission, by

$$R_\mathrm{emission} = \frac{[\mathrm{PS}]_\mathrm{g} \cdot h_\mathrm{box}}{\mathrm{BET} \cdot t_\mathrm{r}} \ , \tag{3.12}$$

where $[\mathrm{PS}]_\mathrm{g} = 5 \times 10^{-5}$ cm^2 cm^{-3} is the particle surface concentration, BET =

500 m^2 g^{-1}, t_r is the replenishing time, and h_{box} is the box height chosen as 1 km corresponding to the depth of the planetary boundary layer. This yields hourly emission rates of 1.67 kg km^{-2} h^{-1} for the low emission scenario with t_r = 6 h, and 10 kg km^{-2} h^{-1} for the high emission scenario with t_r = 1 h. These emission rates are comparable in magnitude to the soot emission rates of 0.72 kg km^{-2} h^{-1} and 7.2 kg km^{-2} h^{-1} chosen in a previous study by Aklilu and Michelangeli [115] to model typical atmospheric background conditions with the lower rate and locations close to urban combustion sources with the higher rate.

This completes this study's set of model scenarios consisting of the co-adsorption scenarios A, B, and C, and the two classes of emission scenarios which are labeled by the number of replenishments per day as A_{4x}, B_{4x}, C_{4x}, and A_{24x}, B_{24x}, C_{24x}. For matters of comparison, additional scenarios are defined at various places in this study. These scenarios are briefly discussed when defined, since they involve only minor changes of the scenarios described above.

As noted before, each model scenario takes into account the gas-phase and surface chemistry defined by the respective surface reaction scenarios and the implemented urban pollution gas-phase chemistry.

The next chapter presents and discusses the results of this modeling study.

Chapter 4

Results and Discussion

The following section presents this study's results in the form of the academic paper:

M. Springmann, D. A. Knopf, and N. Riemer. Detailed Heterogeneous Chemistry in an Urban Plume Box Model: Reversible Co-Adsorption of O_3, NO_2, and H_2O on Soot coated with Benzo[a]pyrene. *Atmospheric Chemistry and Physics Discussions*, 9(2):1005510099, 2009. ISSN 1680-7367. URL http://www.atmos-chem-phys-discuss.net/9/10055/2009/. [1]

The permission for reproduction was granted by the co-authors. The formatting has been adapted to the format of this thesis.

4.1 Detailed Heterogeneous Chemistry in an Urban Plume Box Model: Reversible Co-Adsorption of O_3, NO_2, and H_2O on Soot coated with Benzo[a]pyrene

Marco Springmann[1], Daniel A. Knopf[2], Nicole Riemer[3]

[1]Department of Physics and Astronomy, Stony Brook University, NY, USA
[2]School of Marine and Atmospheric Sciences, Institute for Terrestrial and Planetary Atmospheres, Stony Brook University, NY, USA
[3]Department of Atmospheric Sciences, University of Illinois at Urbana-Champaign, IL, USA

Correspondence to: Daniel A. Knopf
(Daniel.Knopf@stonybrook.edu)

Abstract This study assesses in detail the effects of heterogeneous chemistry on the particle surface and gas-phase composition by modeling the reversible co-adsorption of O_3, NO_2, and H_2O on soot coated with benzo[a]pyrene (BaP) for an urban plume scenario over a period of five days. By coupling the Pöschl-Rudich-Ammann (PRA) kinetic framework for aerosols (*Pöschl et al., 2007*) to a box model version of the gas-phase mechanism RADM2, we are able to track individual concentrations of gas-phase and surface species over the course of several days. The flux-based PRA formulation takes into account changes in the uptake kinetics due to changes in the chemical gas-phase and particle surface compositions. This dynamic uptake coefficient approach is employed for the first time in a broader atmospheric context of an urban plume scenario. Our model scenarios include one to three adsorbents and three to five coupled surface reactions. The results show a variation of the O_3 and NO_2 uptake coefficients of more than five orders of magnitude over the course of the simulation time and a decrease in the uptake coefficients in the various scenarios by more than three orders of magnitude within the first six hours. Thereafter, periodic peaks of the uptake coefficients follow the diurnal cycle of gas-phase O_3-NO_x reactions. Physisorption of water vapor reduces the half-life of the coating substance BaP by up to a factor of seven by permanently occupying $\sim 75\%$ of the soot surface. Soot emissions modeled by replenishing reactive surface sites lead to maximum gas-phase O_3 depletions of 41 ppbv and 7.8 ppbv for an hourly and six-hourly replenishment cycle, respectively.

This conceptual study highlights the interdependence of co-adsorbing species and their non-linear gas-phase feedback. It yields further insight into the atmospheric importance of the chemical oxidation of particles and emphasizes the necessity to implement detailed heterogeneous kinetics in future modeling studies.

4.1.1 Introduction

Heterogeneous chemistry describes reactions between gas-phase species and condensed matter. In the atmosphere, these heterogeneous reactions can significantly change the composition of aerosol particles and the atmospheric environment. The most prominent example is heterogeneous reactions on polar stratospheric clouds, which are the key processes for the observed strong ozone depletion during polar spring in the Antartic [8, 10, 11].

In the troposphere, changes in aerosol composition due to heterogeneous reactions can affect the particle's hygroscopicity with subsequent consequences for its radiative properties and its interactions with clouds [e.g., 61, 90, 137]. Furthermore, heterogenous reactions can have significant impact on the chemistry of the troposphere by changing gas-phase concentrations of air pollutants and oxidizing agents [e.g., 120, 138–145]. Human health can be affected by heterogeneous reactions leading to changes in the aerosol particle's toxicity and allergic potential [2, 133, 146–149].

A ubiquitous aerosol particle type, particularly in urban environments, is soot. Soot particles originate from the incomplete combustion of hydrocarbons, e.g., in combustion engines and coal-fired power plants [2, 136], and may be coated with polycyclic aromatic hydrocarbons (PAHs) formed by the same processes [2].

Laboratory studies indicated that gas-phase species such as ozone (O_3) and nitrogen dioxide (NO_2) can react with soot surfaces [29, 34, 61]. Ozonolysis experiments on soot showed rapid initial gas uptake followed by a slower uptake regime during which surface reactions occurred [60, 62, 63]. These surface reactions can produce carboxyl groups that stay on the particle surface and/or volatile species such as CO_2 and H_2O that desorb to the gas phase [66]. The same two-step kinetic process, fast initial uptake followed by a slower uptake regime, was found in experiments probing the adsorption and reactivity of NO_2 on soot [21, 68, 69]. Studies also indicated the subsequent formation and desorption of nitrous acid (HONO), which is important for initiating daytime photochemistry by providing a source for the hydroxyl radical (OH) [33, 68, 72, 114, 150]. Water vapor significantly affects the ozonolysis of soot, as it lowers the O_3 surface concentration, which delays the loss of surface species [60].

The efficiency of heterogeneous reactions is often expressed employing an

uptake coefficient (γ) which represents the ratio between the net flux of a gas-phase species to the condensed phase and the gas kinetic flux of the gas-phase species colliding with the surface [12, 80–82]. Modeling studies often assume constant uptake coefficients to describe heterogeneous reactions [14, 15, 115], or employ empirical parameterizations of the uptake coefficient in dependence of relative humidity, temperature, and aerosol composition [120, 121]. However, the experimental studies on the adsorption of gas-phase species on soot mentioned above indicate that the heterogeneous kinetics depend also on particle surface composition and gas-phase concentrations, in addition to the environmental conditions described by temperature and relative humidity. Consequently, changes in the gas-phase composition due to reactions within the gas phase and uptake of gas-phase species by particles can significantly affect the efficiency of the uptake kinetics. For these reasons, the uptake coefficient cannot a priori be treated as a constant value. Instead, one expects that it generally varies over time due to changes in the particle surface composition and gas-phase concentrations.

Pöschl et al. [12] developed a kinetic model framework for aerosol surface chemistry and gas-particle interactions which includes flux-based mass balance and rate equations, and a clear separation of mass transport and chemical reactions. This treatment, also termed the Pöschl-Rudich-Ammann (PRA) framework [12, 117], allows to consider changes in the rate parameters such as the uptake coefficient as a result of changes in particle surface composition and gas-phase concentrations. For the remainder of this manuscript, we refer to this approach as dynamic uptake coefficient approach emphasizing the potential variability of γ. The PRA framework consists of a double-layer surface model which incorporates gas-surface, surface layer, and surface-bulk reactions and allows the addition of unlimited numbers of chemical species and physicochemical processes [12]. It provides an explicit mechanistic description of concentration and time dependencies of the reactive and non-reactive gas uptake and subsequent changes in particle composition. Using this framework, the two-step kinetic process observed in the ozonolysis and NO_2 adsorption experiments can be described by a Langmuir adsorption-desorption equilibrium followed by Langmuir-Hinshelwood type surface reactions [12, 60, 61, 90].

The focus of this paper is to determine how heterogeneous reactions change the aerosol surface composition and affect the gas-phase concentrations of adsorbing pollutants in an urban plume scenario. To investigate this question, the PRA dynamic uptake coefficient approach is coupled to the Second Generation Regional Acid Deposition Model (RADM2) which is a well-established, nonlinear chemical gas-phase mechanism for modeling atmospheric chemistry on a regional scale [13, 93] under consideration of diurnal changes in photolysis

frequencies and gas-phase emissions. With this coupled model framework, we are able to assess in yet not achieved detail the effects of heterogeneous reactions on particle and atmospheric gas-phase composition for arbitrary time scales. We apply data from several heterogeneous uptake experiments on soot to model the reversible co-adsorption of O_3, NO_2, and water vapor on soot particles coated with the polycyclic aromatic hydrocarbon benzo[a]pyrene (BaP) for an urban plume scenario. These model substances are of high relevance with respect to public health and the environment, as BaP is classified as a "probable human carcinogen" [118] and the trace gases O_3 and NO_2 are major criteria air pollutants [119]. With these gas-phase species, we define three model scenarios of increasing complexity which are comprised of adsorption and surface reactions of O_3, of O_3 and NO_2, and of O_3, NO_2, and water vapor. Since each scenario has a different number of co-adsorbing species, we are able to give a detailed account on the influence of co-adsorption on heterogeneous chemistry and the gas phase. Instead of applying a prescribed uptake coefficient, we explicitly resolve the fluxes that determine the uptake coefficient. Therefore, the uptake coefficient is a quantity that is diagnosed from our calculations and is dependent on adsorbent specific parameters, such as the molecular cross section, the accommodation coefficient, the desorption time, and the adsorbents' gas-phase and surface concentrations and reactions.

The new contributions of this study are the coupling of the PRA framework to gas-phase chemistry and the co-adsorption of multiple gas-phase species with coupled surface reactions. By including the competing effects of O_3, NO_2, and water vapor, the model complexity goes beyond current laboratory experiments, which consider two co-adsorbing gas-phase species at most [e.g., 60]. It also places the heterogeneous reactions into a more realistic atmospheric context with atmospheric humidity levels, gas-phase and soot emissions, and diurnal photolysis patterns.

The scope of this paper is conceptual and relies on some simplifications. For example, the maximum adsorbents' surface coverage is limited to one monolayer, which means that diffusion processes through multiple surface layers are not considered in our model framework. This allows us to treat the uptake of gas-phase species according to Langmuir adsorption kinetics. To reduce complexity, we neglect changes in particle composition due to coagulation, dilution, and condensation of semi-volatile gas-phase species. We also expect more trace gases than the three considered here to adsorb onto soot particles under atmospheric conditions. However, with limiting the number of adsorbents to three, we are able to specifically assess each adsorbent's influence on the heterogeneous chemistry. Other trace gases, such as OH and NO_3, are also involved in important heterogeneous reactions [e.g., 78, 142, 151–

155], but have not been shown to adhere to Langmuir adsorption kinetics with subsequent surface reactions (Langmuir-Hinshelwood type reactions) and are therefore not the subject of this study. Although we attempt to use realistic values characteristic of an urban plume scenario as input parameters, our purpose is not to make exact atmospheric predictions.

The paper is organized as follows. Section 2 describes the employed model framework consisting of the PRA model framework coupled to the gas-phase solver RADM2. In section 3, we outline our model approach by describing the adapted gas-phase chemistry of an urban plume scenario, the representation of soot coated with BaP as a model substance, our model scenarios with the implemented surface reactions, and additional soot emission scenarios. Section 4 presents our results on the temporal evolution of surface composition, the BaP half-life, and the feedback on the gas-phase O_3 concentration for the dynamic uptake approach and, for comparison, for an approach with constant uptake coefficients. We conclude with summarizing the findings and their atmospheric implications.

4.1.2 Coupled PRA Model Framework

The PRA framework [12] describes gas-phase uptake and surface chemistry by a double-layer surface model with sorption layer and quasi-static layer, and by flux-based rate equations. Figure 4.1 shows the scenario we adapt on this basis, supported by experiments on the adsorption and subsequent reaction of O_3 on soot [60], and NO_2 on soot [68]: Gas-phase species X_i(g) adsorbs onto the sorption layer, quantified by the adsorption flux J_{ads}. Adsorbed species X_i(s) can then either desorb, expressed by the desorption flux J_{des}, or react with non-volatile particle components Y_i(ss) from the quasi-static surface layer, which is indicated by a second-order rate coefficient k_{SLR}.

The coupling of the PRA model framework to the gas-phase mechanism RADM2 is achieved by implementing the PRA framework's net production and loss terms of gas-phase and surface species into the chemical integration routine of RADM2. Section 4.1.2 describes the gas-phase loss due to the reversible co-adsorption of gas-phase species using a dynamic uptake approach and section 4.1.2 gives an account of the chemical production and loss of adsorbed and surface species due to Langmuir-Hinshelwood type surface reactions. Throughout these sections, we follow closely the derivations given by Pöschl et al. [12].

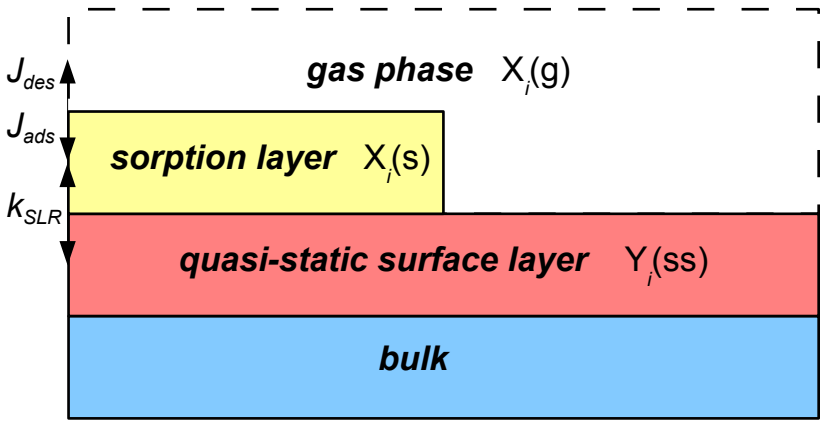

Figure 4.1: The applied surface layer model is shown as a schematic. The gas-particle interface is divided into a gas-phase (g) with gas-phase species $X_i(g)$, a sorption layer (s) with adsorbed gas-phase species $X_i(s)$, a quasi-static surface layer (ss) with non-volatile particle components $Y_i(ss)$, and a particle bulk. The adsorption and desorption fluxes are indicated as J_{ads} and J_{des} respectively, and the rate coefficient for surface layer reactions is denoted by k_{SLR}. Adapted from Pöschl et al. [12].

Dynamic Uptake Coefficient Approach

The uptake coefficient of gas species X_i, γ_{X_i}, is defined, in terms of fluxes, as the ratio between the net flux of X_i to the condensed phase, J_{net,X_i}, and the gas kinetic flux of X_i colliding with the surface, J_{coll,X_i}:

$$\gamma_{X_i} = \frac{J_{\text{net},X_i}}{J_{\text{coll},X_i}} \,. \tag{4.1}$$

It is important to note that this definition of γ_{X_i} does not explicitly include chemical reactions or gas-phase diffusion, as is often assumed when referring to the reactive uptake coefficient.

The collision flux is based on kinetic gas theory and can be expressed as

$$J_{\text{coll},X_i} = [X_i]_{\text{gs}} \frac{\omega_{X_i}}{4} \,, \tag{4.2}$$

where $[X_i]_{\text{gs}}$ is the gas-phase concentration close to the surface and ω_{X_i} is the mean thermal velocity of molecule X_i given by $\omega_{X_i} = \sqrt{8RT/(\pi M_{X_i})}$, where R is the universal gas constant, T is the absolute temperature, and M_{X_i} is the molar mass of species X_i.

Significant net uptake of the gas-phase species can lead to its local depletion close to the surface. A gas-phase diffusion correction factor $C_{\mathrm{g,X}_i}$ can be applied to relate the gas-phase concentration close to the surface $[\mathrm{X}_i]_{\mathrm{gs}}$ to the average gas-phase concentration $[\mathrm{X}_i]_{\mathrm{g}}$, such that $C_{\mathrm{g,X}_i} = \frac{[\mathrm{X}_i]_{\mathrm{gs}}}{[\mathrm{X}_i]_{\mathrm{g}}}$. For γ_{X_i}-values smaller than one, which is justified for the scenarios considered here, $C_{\mathrm{g,X}_i}$ can be determined as [83]

$$C_{\mathrm{g,X}_i} = \frac{1}{1 + \gamma_{\mathrm{X}_i} \frac{0.75+0.28\mathrm{Kn}_{\mathrm{X}_i}}{\mathrm{Kn}_{\mathrm{X}_i}(1+\mathrm{Kn}_{\mathrm{X}_i})}} \,, \tag{4.3}$$

where $\mathrm{Kn}_{\mathrm{X_i}}$ is the Knudsen number given by

$$\mathrm{Kn}_{\mathrm{X}_i} = \frac{6 D_{\mathrm{g,X}_i}}{\omega_{\mathrm{X}_i} d_{\mathrm{p}}} \,. \tag{4.4}$$

$D_{\mathrm{g,X}_i}$ is the gas-phase diffusion coefficient of species X_i and d_{p} is the particle diameter. Using the diffusion coefficients for O_3, NO_2, and water vapor given by Massman [156] and a particle diameter of 119 nm for soot [60] results in Knudsen numbers of about 2.17 for NO_2 and H_2O and 2.35 for O_3. Sensitivity runs with and without gas-phase diffusion corrections showed no difference for the case of O_3 and H_2O uptake, and only a difference within the first 10 s of maximum 2% for NO_2 uptake. For this reason, the gas-phase diffusion correction for the cases considered here can be neglected and the gas-phase concentration close to the surface equals the average gas-phase concentration, $[\mathrm{X}_i]_{\mathrm{gs}} \approx [\mathrm{X}_i]_{\mathrm{g}}$.

The net flux to the condensed phase is the difference of the adsorption flux and desorption flux,

$$J_{\mathrm{net,X}_i} = J_{\mathrm{ads,X}_i} - J_{\mathrm{des,X}_i} \,. \tag{4.5}$$

The adsorption flux of a gas molecule X_i is related to the collision flux via the accommodation coefficient $\alpha_{\mathrm{s,X}_i}$ representing the molecule's probability of adsorption on the surface:

$$\alpha_{\mathrm{s,X}_i} = \frac{J_{\mathrm{ads,X}_i}}{J_{\mathrm{coll,X}_i}} \,. \tag{4.6}$$

Thus, $J_{\mathrm{ads,X}_i}$ can be expressed as

$$J_{\mathrm{ads,X}_i} = \alpha_{\mathrm{s,X}_i} J_{\mathrm{coll,X}_i} = \alpha_{\mathrm{s,X}_i} \frac{\omega_{\mathrm{X}_i}}{4} [\mathrm{X}_i]_{\mathrm{gs}} \,. \tag{4.7}$$

In case of competitive co-adsorption of several gas-phase species, the accommodation coefficient of the individual species, $\alpha_{\mathrm{s,X}_i}$, can be derived using a Langmuir adsorption model in which all adsorbate species compete for a single

sorption site on the quasi-static surface, such that

$$\alpha_{\mathrm{s,X}_i} = \alpha_{\mathrm{s,0,X}_i}(1-\theta_\mathrm{s}) \ , \tag{4.8}$$

where $\alpha_{\mathrm{s,0,X}_i}$ is the surface accommodation coefficient on an adsorbate-free surface. θ_s is the sorption layer surface coverage which is given by the sum of fractional surface coverages of all competing adsorbate species, $\theta_{\mathrm{s,X}_p}$, i.e., $\theta_\mathrm{s} = \sum_p \theta_{\mathrm{s,X}_p}$. The fractional surface coverage depends on the surface concentration of the adsorbate species X_p, $[\mathrm{X}_p]_\mathrm{s}$, and its effective molecular cross section, $\sigma_{\mathrm{s,X}_p}$, which corresponds to the inverse of the species' maximum surface concentration in the sorption layer, $[\mathrm{X}_p]_\mathrm{s,max}$:

$$\theta_{\mathrm{s,X}_p} = [\mathrm{X}_p]_\mathrm{s}/[\mathrm{X}_p]_\mathrm{s,max} = \sigma_{\mathrm{s,X}_p}[\mathrm{X}_p]_\mathrm{s} \ . \tag{4.9}$$

The desorption flux of species X_i can be quantified by the ratio between this species' surface concentration $[\mathrm{X}_i]_\mathrm{s}$ and its desorption lifetime $\tau_{\mathrm{d,X}_i}$ which is the mean residence time of the species on the surface:

$$J_{\mathrm{des,X}_i} = [\mathrm{X}_i]_\mathrm{s}/\tau_{\mathrm{d,X}_i} \ . \tag{4.10}$$

By combining Eqs. (4.1)–(4.10) and assuming $[\mathrm{X}_i]_\mathrm{gs} = [\mathrm{X}_i]_\mathrm{g}$, the uptake coefficient of species X_i can be derived as

$$\begin{aligned} \gamma_{\mathrm{X}_i} &= \frac{J_{\mathrm{ads,X}_i} - J_{\mathrm{des,X}_i}}{J_{\mathrm{coll,X}_i}} \\ &= \frac{\frac{1}{4}\alpha_{\mathrm{s,0,X}_i}\omega_{\mathrm{X}_i}[\mathrm{X}_i]_\mathrm{g}(1-\sum_p \sigma_{\mathrm{s,X}_p}[\mathrm{X}_p]_\mathrm{s}) - \frac{[\mathrm{X}_i]_\mathrm{s}}{\tau_{\mathrm{d,X}_i}}}{\frac{1}{4}\omega_{\mathrm{X}_i}[\mathrm{X}_i]_\mathrm{g}} \ . \end{aligned} \tag{4.11}$$

Equation (4.11) shows that the uptake coefficient derived according to Pöschl et al. [12] depends on the parameters of the adsorbing species such as $\alpha_{\mathrm{s,0,X}_i}$, $\sigma_{\mathrm{s,X}_p}$, ω_{X_i}, $\tau_{\mathrm{d,X}_i}$, but also on its surface and gas-phase concentrations $[\mathrm{X}_i]_\mathrm{s}$ and $[\mathrm{X}_i]_\mathrm{g}$, which can be affected by transport and chemical reactions. Therefore, Eq. (4.11) expresses γ_{X_i} as a dynamic uptake coefficient when changes in $[\mathrm{X}_i]_\mathrm{s}$ and $[\mathrm{X}_i]_\mathrm{g}$ are taken into account. The numerator of Eq. (4.11) describes the net flux of X_i(g) to the particle and hence the generation of X_i(s) in the sorption layer under consideration of the surface coverage of all adsorbing species. Surface reactions need to be taken into account to obtain the total net production of sorption layer species, which we outline in section 4.1.2. It should be noted that the initial adsorbent surface concentration in the sorption layer is zero, thus, the uptake coefficient's initial value is given by the accommodation coefficient, $\gamma_{\mathrm{X}_i,\mathrm{ini}} = \alpha_{\mathrm{s,0,X}_i}$.

The net gas-phase loss of adsorbent X_i, i. e. loss L due to uptake onto the particle in the condensed phase minus production P due to desorption back to the gas phase, is calculated by multiplying the adsorbent's collision flux by the corresponding dynamic uptake coefficient and by the particle surface area in air, $[\mathrm{PS}]_\mathrm{g}$:

$$\begin{aligned}\left[\frac{\mathrm{d}}{\mathrm{dt}}[\mathrm{X}_i]_\mathrm{g}\right]_\mathrm{uptake} &= L_{\mathrm{g,p,X}_i} - P_{\mathrm{g,p,X}_i} \\ &= J_{\mathrm{coll,X}_i}\gamma_{\mathrm{X}_i}[\mathrm{PS}]_\mathrm{g} = \gamma_{\mathrm{X}_i}[\mathrm{PS}]_\mathrm{g}[\mathrm{X}_i]_\mathrm{g}\frac{\omega_{\mathrm{X}_i}}{4} \ . \end{aligned} \tag{4.12}$$

The next section describes the reaction kinetics between the adsorbed species and surface components according to a Langmuir-Hinshelwood reaction mechanism.

Langmuir-Hinshelwood Mechanism For Surface Reactions

The Langmuir-Hinshelwood mechanism describes reactions in which adsorbed gas-phase species react on the surface [12]. For the cases considered here, we focus on surface reactions between the sorption layer (s) and the quasi-static surface layer (ss) following the derivations by Pöschl et al. [12] and Ammann and Pöschl [117]. Chemical reactions that proceed between the gas phase and the particle surface, exclusively within the sorption or the quasi-static surface layer, as well as photo-chemical processes on the surface are neglected. We assume the product of the surface reactions to be a surface component residing within the quasi-static surface layer. Applying these assumptions, the net chemical production of quasi-static surface species Y_i(ss) from reaction between adsorbed species in the sorption layer, X_p(s), and surface components in the quasi-static surface layer, Y_q(ss), is determined by

$$\begin{aligned}\frac{\mathrm{d}}{\mathrm{dt}}[\mathrm{Y}_i]_\mathrm{ss} &= P_{\mathrm{s,ss,Y}_i} - L_{\mathrm{s,ss,Y}_i} \\ &= \sum_v \sum_p \sum_q c_{\mathrm{SLR}v,\mathrm{s,Y}_i} k_{\mathrm{SLR}v,\mathrm{X}_p,\mathrm{Y}_i}[\mathrm{X}_p]_\mathrm{s}[\mathrm{Y}_q]_\mathrm{ss} \ , \end{aligned} \tag{4.13}$$

where v numbers the rate equation, p and q number the reactants, c_SLR are negative or positive stoichiometric coefficients, and k_SLR are second-order rate coefficients.

In contrast to quasi-static surface layer components which are produced and lost through surface reactions, adsorbed sorption layer species are only depleted by surface reactions, since we assume the surface reactions considered here to be irreversible. The loss of sorption layer species X_i due to the surface

reactions is a subset of Eq. (4.13) with the reactant summation index variable p fixed to species X_i:

$$L_{\mathrm{s,ss,X}_i} = \sum_v \sum_q c_{\mathrm{SLR}v,\mathrm{s,X}_i} k_{\mathrm{SLR}v,\mathrm{X}_i,\mathrm{Y}_i} [\mathrm{X}_i]_\mathrm{s} [\mathrm{Y}_q]_\mathrm{ss} \ . \tag{4.14}$$

The total net chemical production of sorption layer species X_i(s) is composed of the loss due to surface reactions and the production and loss due to adsorption and desorption:

$$\frac{\mathrm{d}}{\mathrm{dt}} [\mathrm{X}_i]_\mathrm{s} = J_{\mathrm{ads,X}_i} - J_{\mathrm{des,X}_i} - L_{\mathrm{s,ss,X}_i} \ , \tag{4.15}$$

where the fluxes of adsorption and desorption, $J_{\mathrm{ads,X}_i}$ and $J_{\mathrm{des,X}_i}$, are described in section 4.1.2.

The differential Eqs. (4.12), (4.13), and (4.15) represent the heterogeneous kinetics adapted in our model framework. We implement these differential equations into the chemical integration routine of RADM2 [13, 93] to obtain solutions and to account for the temporal evolution of the gas phase.

In the next section, we specify the gas-phase chemistry of RADM2 and give a detailed account of our model approach and implemented heterogeneous chemistry scenarios.

4.1.3 Model Approach

We model the reversible co-adsorption and subsequent surface reactions of O_3, NO_2, and water vapor on soot coated with BaP in an urban plume scenario. Section 4.1.3 describes the gas-phase chemistry of this urban plume scenario as implemented into the chemical gas-phase solver RADM2. Section 4.1.3 gives a representation of soot coated with BaP as a model substance, which is followed by an overview of the implemented surface reactions and corresponding model scenarios in section 4.1.3. Section 4.1.3 describes two soot emission scenarios to assess the gas-phase feedback from heterogeneous reactions under polluted conditions.

Gas-Phase Chemistry

The chemical gas-phase solver RADM2 includes 62 chemical species, 21 photolysis reactions, and 140 thermal reactions [13]. A detailed account on the gas-phase reactions of RADM2 is given elsewhere [13, 93]. RADM2 is widely used in atmospheric models to predict concentrations of oxidants and other air pollutants [e.g., 122, 123]. The main feature that RADM2 provides to this

study is the NO_x-O_3 chemistry with its diurnal pattern. This results in continuous changes in the O_3 and NO_2 gas-phase concentrations throughout the simulation period. These variations in gas-phase concentrations subsequently affect the magnitude of the individual and combined uptake of O_3 and NO_2 by the soot particles. This investigation of the gas phase-particle surface interrelationship under atmospherically relevant conditions is one of the main foci and and novelty of this study.

We use RADM2 in a tropospheric urban plume scenario (PLUME1) according to Kuhn et al. [100]. This case was designed to represent the chemistry in the polluted boundary layer, which is consistent with an urban plume scenario where emissions of soot occur. This plume scenario includes constant emissions for a variety of trace gases representative for continental European air [128], such as 0.54 pptv min^{-1} of SO_2, 2.68 pptv min^{-1} of NO, and 5.85 pptv min^{-1} of CO. Volatile organic compounds (VOCs) are aggregated into 15 classes of reactive organic species with emissions of 0.14 pptv min^{-1} for formaldehyde (HCHO), 0.037 pptv min^{-1} for acetaldehyde and higher aldehydes, and 0.46 pptv min^{-1} for acetone, methyl ethyl ketone and higher ketones. Initial concentrations are set to 50 ppbv for O_3, 0.5 ppbv for NO_2, 0.2 ppbv for NO, and 20,000 ppmv for H_2O which corresponds to 64% relative humidity (RH). Time-dependent photolysis rates are calculated as described in Kuhn et al. [100]. Physical processes such as deposition and dilution of trace gases and soot particles, and particle coagulation are not considered. As suggested by Vogel et al. [114], the reaction rate for the production of HONO from NO and OH was revised according to Atkinson et al. [127].

RADM2 is run in a box model version for a modeling period of five days, under atmospheric conditions of 1013.25 hPa pressure and a temperature of 298 K. The simulation starts at 12 noon. The gas-phase chemistry in RADM2 is solved with a variable chemical time step [93] ranging from 0.096 s to 3 s. To resolve the rapid adsorption of water vapor in scenario C, a shorter time step is used for the first day of the simulation period, ranging from 0.003 s to 0.006 s. The gas-phase solver RADM2 and the heterogeneous chemistry part outlined in the last section run in a coupled fashion for all model scenarios considered in this paper.

Representation of Soot

The chemical surface reactions occur on a population of soot particles coated with BaP. We adopted an initial soot concentration of 10 $\mu g\, m^{-3}$ in air corresponding to concentrations in heavily polluted air [16]. Since the soot surface is of fractal-like geometry [35], we use the surface area obtained from Brunauer-Emmett-Teller (BET) isotherms as reactive surface area and implement a BET

value of 500 $m^2\,g^{-1}$. This corresponds to values that have been used in laboratory heterogeneous chemistry studies [e.g., 63, 134, 135]. Multiplying the BET value by the soot concentration yields a total surface concentration of $[PS]_g = 5 \times 10^{-5}$ cm^2 cm^{-3}. However, BET values for soot can range from 6 $m^2\,g^{-1}$ for aircraft engine combustor soot [37] to approximately 500 $m^2\,g^{-1}$ for the post-treated black carbon Degussa FW2 [38], which can lead to large differences in $[PS]_g$. Thus, the implemented BET-value of 500 $m^2\,g^{-1}$ may result in an upper limit for the concentration of surface reaction sites.

While the surface concentration remains constant in this model, the passivation of the surface is introduced by the consumption of the BaP coating, which has initially a surface concentration of $1{\times}10^{14}$ cm^{-2} corresponding to a full monolayer coverage. BaP readily adsorbs onto soot particles and can be regarded as a proxy for the wider class of polycyclic aromatic compounds, but also for soot due to its structural similarities of the surface [60]. Soot can be pictured as agglomerate of graphene layers, while BaP ($C_{20}H_{12}$) represents a single graphene layer consisting of five six-membered aromatic rings [60, 157]. Here, BaP provides consumable reactive sites for adsorption processes and surface reactions.

Surface reactions

We define three model scenarios with an increasing level of complexity. These scenarios represent the adsorption and surface reactions of O_3 in scenario A, of O_3 and NO_2 in scenario B, and of O_3, NO_2, and water vapor in scenario C. As starting point for the dynamic uptake coefficient approach described in section 4.1.2, we implemented experimentally determined initial uptake coefficients as accommodation coefficients in accord to Ammann and Pöschl [117]. This approach is justified, since initially $\gamma_{\mathrm{X}i} = \alpha_{\mathrm{s},0,\mathrm{X}i}$, as can be seen from equation (4.11). In the following, we discuss each scenario with regards to the implemented surface reactions and adapted input parameters with reference to Table 4.1.

Scenario A represents the adsorption of O_3 and subsequent surface reactions of O_3 with BaP and its derivatives. After O_3 is adsorbed to the sorption layer (s), it participates in three surface reactions with the quasi-static surface layer (ss), (1) to (3), as given in Table 4.1. These reactions convert BaP into chemical derivatives Y2, Y3, and Y4, whose chemical form is not exactly known, but can be pictured as BaP derivatives with an increasing number of oxygenated functional groups and decreasing reactivity towards photooxidants such as BaP-quinones, hydroxy-ketones, acid anhydrides, lactones, etc. [59, 131–133]. This scenario corresponds to Model System Solid 1 [117], except that it includes the atmospheric context by the coupling to RADM2.

Table 4.1: Adsorbents, surface reactions, reaction rates, and parameters (accommodation coefficient (α), effective molecular cross section (σ), desorption time (τ)) applied in model scenarios A, B, C.

Scenario	Adsorbents	Surface reactions
A	O_3	(1) O_3(s) + BaP(ss) → Y2(ss) (2) O_3(s) + Y2(ss) → Y3(ss) (3) O_3(s) + Y3(ss) → Y4(ss)
B	O_3, NO_2	(1) to (3) (4) NO_2(s) + Y2(ss) → Y5(ss) (5) NO_2(s) + Y3(ss) → HONO(g)
C	O_3, NO_2, H_2O	(1) to (5)
Scenario	**Reaction rates [cm^2 s^{-1}]**	**Parameters**
A	$k_{SLR1} = 2.1 \times 10^{-17}$ [60, 117] $k_{SLR2} = 2.1 \times 10^{-19}$ [117] $k_{SLR3} = 2.1 \times 10^{-21}$ [117]	$\alpha_{s,0,O_3} = 1 \times 10^{-3}$ [60, 65, 117] $\sigma_{O_3} = 1.8 \times 10^{-15}$ cm^2 [60, 117] $\tau_{d,O_3} = 18$ s [60, 117]
B	k_{SLR1} to k_{SLR3} $k_{SLR4} = 7 \times 10^{-18}$ [117] $k_{SLR5} = 7.5 \times 10^{-21}$ [116, 117]	$\alpha_{s,0,NO_2} = 0.14$ [71, 117] $\sigma_{NO_2} = 3 \times 10^{-15}$ cm^2 [116, 117] $\tau_{d,NO_2} = 18$ s [116, 117]
C	k_{SLR1} to k_{SLR5}	$\alpha_{s,0,H_2O} = 0.4 \times 10^{-3}$ [60, 67] $\sigma_{H_2O} = 1.08 \times 10^{-15}$ cm^2 [130] $\tau_{d,H_2O} = 3 \times 10^{-3}$ s [60]

The reaction rate k_{SLR1}, and the O_3-specific parameters $\alpha_{s,0,O_3}$, σ_{O_3}, τ_{d,O_3} are adapted from results of aerosol flow tube experiments at ambient temperature and pressure [60]. The reaction rate coefficients for reactions (2) and (3), k_{SLR2} and k_{SLR3}, were chosen according to Ammann and Pöschl [117] to account for the decreasing reactivity of the BaP derivatives.

Scenario B represents the co-adsorption and subsequent surface reactions of O_3 and NO_2. In addition to surface reactions (1) to (3), adsorbed NO_2 also reacts with BaP derivatives according to surface reactions (4) and (5) as listed in Table 4.1. Based on Model System Solid 2 [117], the products consist of another surface component (with increased oxygenated functional group) and a volatile component which desorbs to the gas-phase. Input parameters

are based on experimental data for the reaction and adsorption of NO_2 at the surface of soot particles in Knudsen cell experiments [71], aerosol flow reactor experiments [68], and filter deposition experiments [116]. The reaction rate coefficient for surface reaction (4), k_{SLR4}, was adjusted by Ammann and Pöschl [117] to fit the experimental data. In surface reaction (5), we identify the volatile component with nitrous acid (HONO) and apply a reaction rate of 3.7×10^{-3} s^{-1} according to Ammann et al. [68], which yields 7.5×10^{-21} cm^2 s^{-1}.

Scenario C involves the co-adsorption of O_3, NO_2, and water vapor, with subsequent surface reactions of O_3 and NO_2 according to surface reactions (1) to (5) as listed in Table 4.1. For this scenario, we assume that water vapor adsorbs to the surface without being involved in subsequent surface reactions. This is supported by Pöschl et al. [60], who observed a slower decay of BaP and smaller gas-phase O_3 loss under humid conditions indicating the inhibition of O_3 adsorption by competitive adsorption of water vapor at the aerosol surface. Since freshly emitted discharge soot particles are known to be hydrophobic, physisorption of water vapor on soot was suggested as the mechanism for adsorption, supported by the water vapor's small desorption lifetime [60]. The H_2O specific parameters $\alpha_{\mathrm{s,0,H_2O}}$ and $\tau_{\mathrm{d,H_2O}}$ are adapted from Rogaski et al. [67] and Pöschl et al. [60], and $\sigma_{\mathrm{H_2O}}$ is taken from Nishino [130].

In our first set of simulations we start with an initial soot concentration and do not include any emissions of fresh soot over the course of the simulation. While the surface concentration $[\mathrm{PS}]_{\mathrm{g}}$ remains constant, the uptake coefficient γ_{X_i} does change with time, according to the available surface reaction sites and gas concentrations, which is explicitly predicted from Eq. (4.11). In the second set of simulations, we also keep the surface concentration constant, but include the effect of soot emissions by replenishing the reactive surface sites, which we describe in the next section.

Soot Emissions

In polluted areas, soot is emitted continuously by a variety of sources, such as car traffic and coal-fired power plants [2, 136]. Once emitted, the surface of soot particles is expected to become passivated as surface sites are taken up by adsorbents. Therefore, at any given point in time, soot particles of different ages with different surface reactivities co-exist, ranging from freshly emitted particles with large numbers of reactive surface sites to aged particles where most of the surface sites are depleted. In such an environment, the continuous emission of fresh soot particles could be important when estimating the gas-phase feedback from heterogeneous reactions on soot. In our box model framework, individual soot particles that are introduced at different times due to continuous emissions cannot be tracked. Nevertheless, to estimate the effect

of freshly emitted soot particles on the gas phase in our box-model framework, we adopt the following approach as a sensitivity study.

The emission of fresh soot in our box model is approximated by resetting the soot surface to its initial condition with a BaP surface concentration of $[\mathrm{BaP}] = 1 \times 10^{14}$ cm^{-2} and no secondary surface components. At this point in the simulation, the existing population of soot with the residual BaP concentration and higher order surface components is discarded. While the number of reactive surface sites changes to account for the effect of soot emissions on chemical reactions, we assume the overall soot production and loss to be in equilibrium and therefore keep the soot surface concentration $[\mathrm{PS}]_\mathrm{g}$ constant. We neglect physical processes, such as coagulation, deposition, and dilution of the soot particles. The BaP surface concentration on soot is replenished according to the two following scenarios. In the low emission scenario, the reactive surface is replenished every six hours, and in the high emission scenario, it is replenished every hour. The error from neglecting gas-phase uptake on discarded populations for these replenishing times will be assessed in the next section.

The replenishing times are related to hourly emission rates, R_emission, by

$$R_\mathrm{emission} = \frac{[\mathrm{PS}]_\mathrm{g} \cdot h_\mathrm{box}}{\mathrm{BET} \cdot t_\mathrm{r}} \,, \tag{4.16}$$

where $[\mathrm{PS}]_\mathrm{g} = 5 \times 10^{-5}$ cm^2 cm^{-3} is the particle surface concentration, BET = 500 m^2 g^{-1}, t_r is the replenishing time, and h_box is the box height which we choose as 1 km corresponding to the depth of the tropospheric boundary layer. This yields hourly emission rates of 1.67 kg km^{-2} h^{-1} for the low emission scenario with $t_\mathrm{r} = 6$ h, and 10 kg km^{-2} h^{-1} for the high emission scenario with $t_\mathrm{r} = 1$ h. These emission rates are comparable in magnitude to the soot emission rates of 0.72 kg km^{-2} h^{-1} and 7.2 kg km^{-2} h^{-1} chosen in a previous study by Aklilu and Michelangeli [115] to model typical atmospheric background conditions with the lower rate and locations close to urban combustion sources with the higher rate.

This completes our set of model scenarios consisting of the co-adsorption scenarios A, B, and C, and the two classes of emission scenarios which are labeled by the number of replenishments per day as $\mathrm{A_{4x}}$, $\mathrm{B_{4x}}$, $\mathrm{C_{4x}}$, and $\mathrm{A_{24x}}$, $\mathrm{B_{24x}}$, $\mathrm{C_{24x}}$. For matters of comparison, we define additional scenarios at various places in this paper. We briefly discuss these scenarios when defined, since they involve only minor changes of the scenarios described above.

4.1.4 Results and Discussion

In this section, we present and discuss the results of the different model scenarios. Section 4.1.4 focuses on the soot surface chemistry and composition, followed by an account of the characteristic lifetime of the coating substance BaP in section 4.1.4. In section 4.1.4, we assess the influence of heterogeneous reactions on the gas-phase O_3 concentration for emission and non-emission scenarios. These results are then compared with the gas-phase O_3 feedback obtained by applying constant uptake coefficients in section 4.1.4.

Surface Composition

The surface chemistry of scenario A is shown in Fig. 4.2A. During the first 0.1 min, O_3 adsorbs onto an essentially adsorbate free surface with $\theta_s \approx 0$. This causes the initial plateau of the O_3 uptake coefficient γ_{O_3} where its value is dominated by the adsorption flux, so that $\gamma_{O_3} \approx 0.001 = \alpha_{s,0,O_3}$. When reaching a O_3 surface concentration of $[O_3]_s \approx 1.5 \times 10^{14}$ cm^{-2}, the surface becomes saturated leading to the first decrease in γ_{O_3} until around 1 min. The subsequent plateau in γ_{O_3} is due to the chemical reaction of O_3 in the sorption layer with BaP in the quasi-static surface layer. As a result, the BaP surface concentration decreases, the reactions product concentration $[Y2]_{ss}$ increases, and O_3 uptake remains constant to sustain the reaction. Further depletion of BaP causes the second decrease of γ_{O_3} at 10 min, followed again by a plateau due to the reaction of O_3 with Y2 that increases the surface concentration of Y3. The same temporal pattern applies for the production of Y4 from the reaction of O_3 with Y3. After the first day, the gas-phase O_3 concentration increases due to the photochemical production from the reactions of the O_3 precursors NO_x and VOCs. This is shown in Fig. 4.2G, which presents the gas-phase concentrations and diurnal cycles of O_3, NO_2, NO, and HONO corresponding to scenario A. Since the effect of the surface chemistry on the gas phase is negligible in scenario A, B, and C, the temporal evolution of the gas-phase concentrations in scenarios A, B, and C are identical. An increase in the gas-phase O_3 concentration results in a larger O_3 uptake according to Eq. (4.11). However, with $\gamma_{O_3} < 1 \times 10^{-7}$, its magnitude stays below first-day values due to increased surface saturation and the consumption of reactive primary surface components. Within the first day, BaP is decreased by almost 100%, essentially turning off surface reaction (1) which subsequently slows down or inhibits reactions (2) to (5) due to the decrease of educt production. During nighttime, the O_3 adsorption flux decreases due to O_3-depleting reactions and the absence of gas-phase O_3 sources. On the other hand, high surface saturation leads to an increase in the desorption flux of surface O_3,

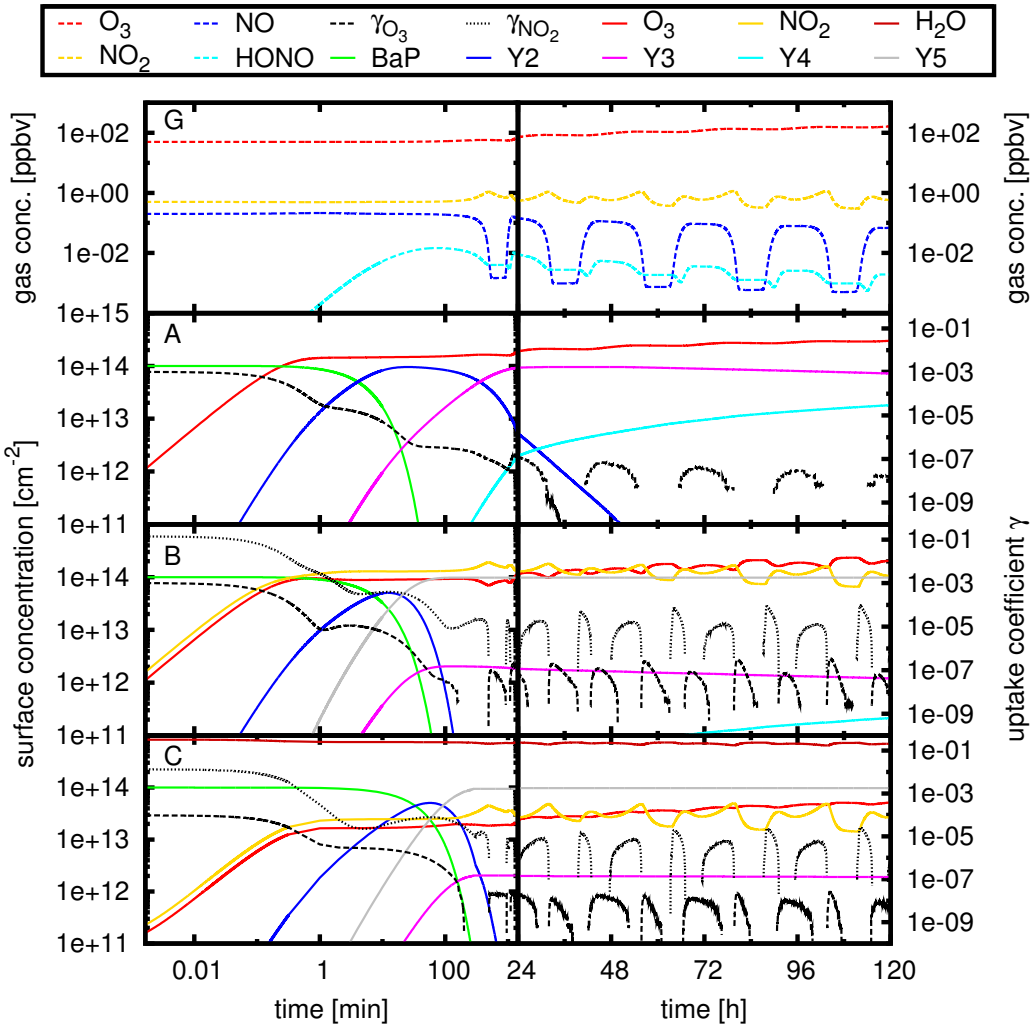

Figure 4.2: The temporal evolution of gas-phase component concentrations (G), surface component concentrations, and uptake coefficients for the adsorption and surface reaction of O_3 (A), the co-adsorption of O_3 and NO_2 (B), and the co-adsorption of O_3, NO_2 and H_2O (C) following the surface reactions defined in Table 4.1 is plotted on a logarithmic timescale for day one (left panels) and on a linear timescale for the four following days (right panels). The temporal evolution of gas-phase components (G) is identical for scenarios A, B, and C, since the effect of the heterogeneous reactions on the gas phase is negligible in these scenarios.

so that the desorption flux can temporarily exceed the adsorption flux. This results in negative γ_{O_3}-values which represent the direct response to the diurnal cycle of gas-phase O_3 as depicted in Fig. 4.2G and are indicated by the discontinuations along the abscissa in Fig. 4.2A. The value of γ_{O_3}decreases by more than five orders of magnitude and then becomes negative.

The surface chemistry of scenario B is shown in Fig. 4.2B. In this scenario, two gas-phase species, O_3 and NO_2, adsorb onto the soot surface. Initial adsorption of gas-phase species, chemical consumption of BaP and surface components, and chemical production of surface components proceed similar to scenario A. Although NO_2 gas-phase concentrations are lower, the initial NO_2 uptake exceeds that of O_3 due to a larger accommodation coefficient for NO_2 of $\alpha_{s,0,NO_2} = 0.14$ compared to $\alpha_{s,0,O_3} = 0.001$ for O_3. In comparison to scenario A, the O_3 surface concentration is reduced in scenario B due to the co-adsorption of NO_2. Also concentrations of the other surface components are different compared to the ones in scenario A. The lifetime of Y2 decreases by almost two days due the added Y5-producing reaction with NO_2. The Y3 concentration is reduced by almost half in comparison to scenario A, since not all Y2 are converted into Y3 anymore. As given in Table 4.1, the reaction rates for the reactions of NO_2 with Y2 and Y3 are faster than the reaction rates for the reactions of O_3 with Y2 and Y3. Therefore, NO_2 converts Y2 into Y5 and Y3 into HONO faster than O_3 converts Y2 to Y3 and further to Y4. This delays Y4 production by over two days. The proportionality between adsorption flux and gas-phase concentration in Eq. (4.7) relates the adsorbents' uptake coefficients and surface concentrations to their gas-phase concentrations. This becomes evident after the initial surface saturation at around one minute of simulation time and, more pronounced, after six hours. Since the NO_2 adsorption flux initially exceeds that of O_3, more NO_2 molecules than O_3 molecules are occupying surface sites. Therefore the NO_2 surface concentration exhibits the same temporal evolution as the NO_2 gas-phase concentration, which can be seen by comparing Fig. 4.2B to Fig. 4.2G. The O_3 surface concentration increases when surface sites become available from a decrease in the NO_2 surface concentration due to a decrease in the NO_2 gas-phase concentration. The resulting alternating evolution of O_3 and NO_2 surface concentrations also induces an alternating evolution of O_3 and NO_2 uptake coefficients, with maxima ranging from $1{\times}10^{-5}$ to 1×10^{-4} for γ_{NO_2}, and from $5{\times}10^{-8}$ to $3{\times}10^{-7}$ for γ_{O_3} on days two to five. However, these values are three orders of magnitude smaller than the initial uptake coefficients. This indicates that 99.9% of the uptake occurs within the first six hours.

The surface chemistry of scenario C is shown in Fig. 4.2C. In this scenario, also water vapor, in addition to NO_2 and O_3, co-adsorbs onto the soot

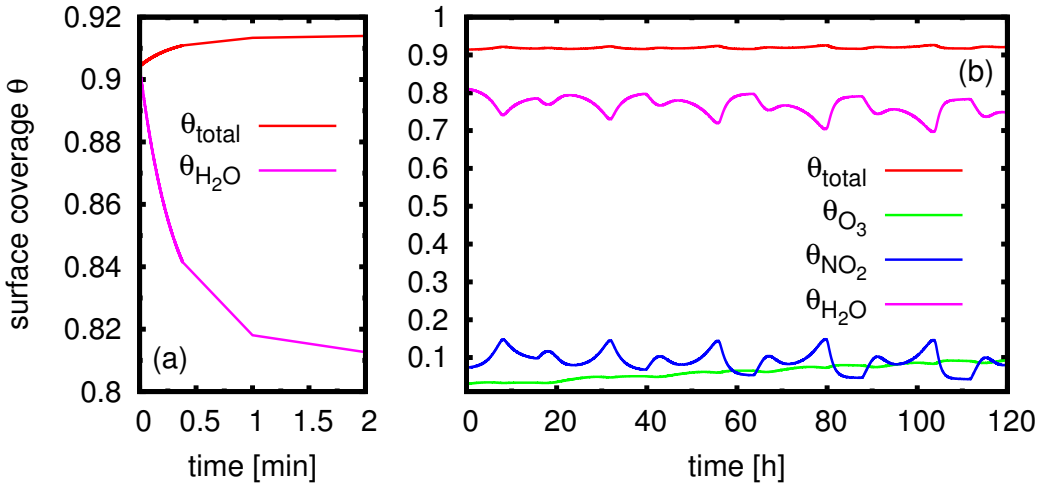

Figure 4.3: The temporal evolution of the soot surface coverage θ in scenario C is shown for the first 2 min (a), and for the entire simulation period of five days (b). The total surface coverage is indicated by θ_{total}, and the fractional surface coverages of O_3, NO_2, and H_2O by θ_{O_3}, θ_{NO_2}, and θ_{H_2O}, respectively. Input parameters and surface reactions for scenario C are given in Table 4.1.

surface, but it does not take part in chemical surface reactions. H_2O has a gas-phase concentration of about 20,000 ppmv. This corresponds to 64% RH and is six and eight orders of magnitude larger than the gas-phase concentrations of O_3 and NO_2, respectively. Due to its high partial pressure, H_2O adsorbs rapidly onto the soot surface. Figure 4.3(a) shows that the H_2O surface coverage is initially over 90%, but decreases to below 82% within the first 2 min of simulation time. Figure 4.3(b) indicates that H_2O constantly occupies about 75% of the total surface for the course of the simulation. This reduces the adsorption fluxes of O_3 and NO_2 and results in a decrease in the surface concentrations and uptake coefficients of O_3 and NO_2 by almost one order of magnitude and half an order of magnitude, respectively, as can be seen by comparison with Fig. 4.2B. Since O_3 and NO_2 adsorption have little influence on the total surface coverage, their gas-phase uptakes and surface concentrations are not as interdependent as in scenario B. Consequently, both the O_3 and the NO_2 surface concentrations mimic closely their respective gas-phase concentrations, which are depicted in Fig. 4.2G. Lower surface concentrations of O_3 and NO_2 also result in slower surface reactions, thereby delaying the production of higher order surface components by over half an order of magnitude. For this reason, the uptake coefficients exhibit only two plateaus on the first day, one due to the initial uptake and one governed by the reactions of O_3

with BaP and NO_2 with Y2. On days two to five, the evolution of O_3 and NO_2 uptake coefficients is similar to the one in scenario B, but in comparison to scenario B, maximum γ-values are reduced by up to one order of magnitude.

We investigated the effect of high NO-emissions on the gas phase and particle surface composition of scenario B by increasing the NO emission 10-fold, from 2.68 pptv min^{-1} to 26.8 pptv min^{-1}. The simulation results are shown in Fig. 4.4. Figure 4.4G shows the temporal evolution of the gas-phase concentrations of O_3, NO_2, NO, and HONO for this model scenario. While the NO gas-phase concentration increases from 0.2 ppbv to 97 ppbv during the five days simulation period, more NO can react with O_3 to produce NO_2 and O_2 leading to a strong nighttime titration of O_3 from the second to the fifth day. Figure 4.4B* presents the soot particle's surface concentrations. As can be seen in Fig. 4.4B*, the O_3 gas-phase depletion is accompanied by a decrease in the O_3 surface concentration. During periods of O_3 depletion, γ_{O_3} becomes negative, since surface desorption exceeds the reduced adsorption from the gas phase. The overall decrease in the O_3 surface concentration delays the production of the surface component Y4 until the fifth day of the simulation period. The decrease in the O_3 surface coverage yields increases in the NO_2 surface concentration resulting in NO_2 saturation with a maximum surface concentration of $1/\sigma_{NO2} = 3 \times 10^{14}$ cm^{-2}. Although only the NO emission rate was changed compared to scenario B, the particle surface compositions of this scenario and of scenario B are significantly different. While in scenario B (see Fig. 4.2B) the O_3 surface concentration is almost double the amount of the NO_2 surface concentration at the end of the five day simulation period, the sorption layer surface in the high NO emission scenario is almost entirely filled with NO_2 molecules (see Fig. 4.4B*). This clearly demonstrates that temporal changes in the gas-phase composition can lead to large differences in the particle surface composition.

The variations in the adsorbents' surface concentrations and uptake coefficients after the first day of the simulation period exemplify the differences to uptake scenarios that do not account for a dynamic gas-phase chemistry, such as the Models Systems Solid 1 and 2 discussed in Ammann and Pöschl [117]. However, as shown in Fig. 4.2, variations in the adsorbents' gas-phase concentrations have a direct effect on the adsorbents' surface concentrations and, consequently, on their uptake coefficients. By accounting for variable gas-phase concentrations in our coupled PRA framework, we can resolve variations in the uptake coefficient over atmospherically relevant time scales and study the effect of different gas-phase scenarios on the particle surface chemistry.

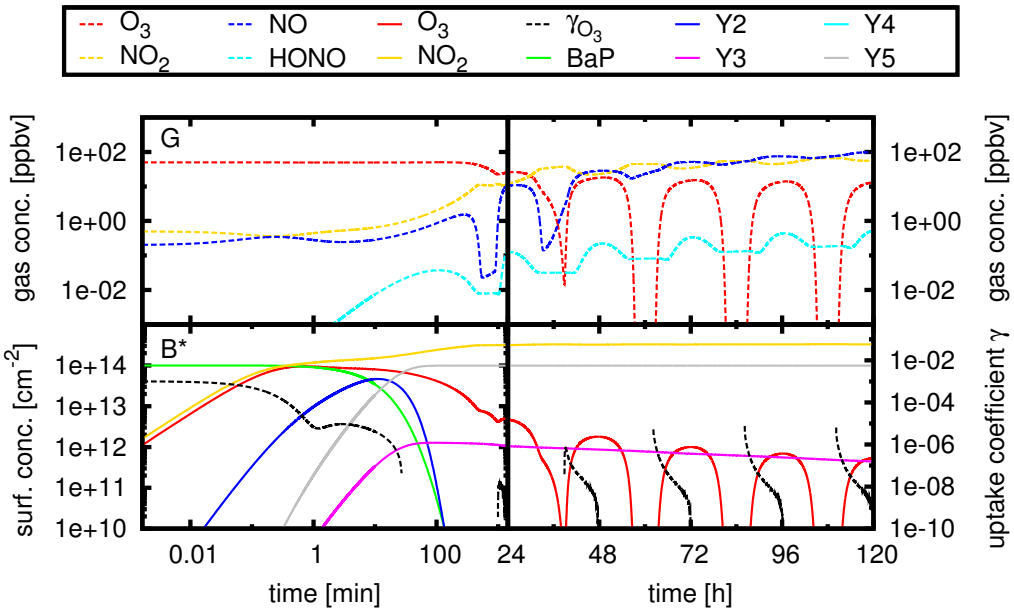

Figure 4.4: The temporal evolution of gas-phase component concentrations (G), surface component concentrations, and uptake coefficients for scenario B* are shown and plotted on a logarithmic timescale for day one (left panels) and on a linear timescale for the four following days (right panels). Scenario B* corresponds to scenario B with a 10-fold increase of the NO emission rates.

BaP Lifetime

The consumption of the soot's BaP coating can be regarded as an initial surface oxidation process due to the reaction with O_3 and NO_2. The efficiency of the heterogeneous kinetics of this oxidation processes can be quantified by the BaP half-life. Figure 4.5 shows the temporal evolution of the BaP concentration for scenarios A, B, C, and scenario C* with the BaP half-lives highlighted by the intersection with the horizontal dotted black line. Scenario C* represents the co-adsorption of O_3 and H_2O following the surface reactions (1) to (3) as given in Table 4.1. It is meant to serve as an additional comparison to scenario A to identify the influence of the co-adsorption of H_2O. Figure 4.5 indicates that the half-life of BaP surface molecules in scenario A is about 4 min. The addition of the co-adsorbing species NO_2 in scenario B extends the half-life by 54% to 6.2 min. Taking into account H_2O physisorption and atmospheric relative humidity of 64% in scenario C increases the half-life of BaP to 32.5 min as indicated in Fig. 4.5. Without the NO_2 co-adsorption in scenario C*, the BaP half-life is 30 min, 10% less than in scenario C. This indicates that the

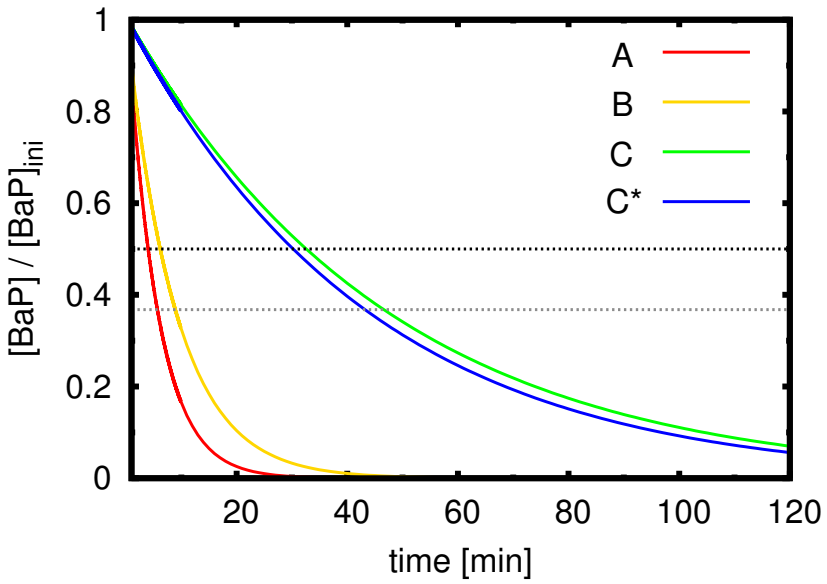

Figure 4.5: The temporal evolution of the ratio of actual BaP surface concentration to initial BaP concentration is shown for scenarios A, B, C, and C*. Scenario A represents the adsorption of O_3, scenario B the co-adsorption of O_3 and NO_2, scenario C the co-adsorption of O_3, NO_2 and H_2O, and scenario C* the co-adsorption of O_3 and H_2O. Scenarios A, B, and C follow the surface reactions given in Table 4.1; scenario C* follows the surface reactions (1) to (3) given in Table 4.1. The intersection with the horizontal dotted lines indicate BaP half-life (dotted black line) and BaP lifetime (dotted grey line).

H_2O co-adsorption is responsible for over 90% of the increase in BaP half-life between scenarios A and C. The reason for this is the rapid adsorption of H_2O on the surface where it occupies a large portion of the available surface sites resulting in a high fractional surface coverage of H_2O, as illustrated in Fig. 4.3. The reactive surface sites occupied by H_2O are not available anymore for the adsorption of O_3 and subsequent BaP consumption via surface reaction (1). Compared to scenarios A and B, the co-adsorption of water vapor leads to a more than five-fold increase in BaP half-life between scenarios C and B, and more than a seven-fold increase between scenarios C* and A.

The sensitivity of the BaP half-life on the adsorption of H_2O is influenced by the H_2O concentration and therefore by RH. Figure 4.6 shows that the BaP half-life increases linearly with RH. An increase from 0% RH to 25% RH results in an almost threefold increase in the BaP half-life from 6 min to 17 min for scenario C. Also shown in Fig. 4.6 are the half-lives of scenarios P and P*. Scenario P* represents BaP half-lives as a function of RH derived

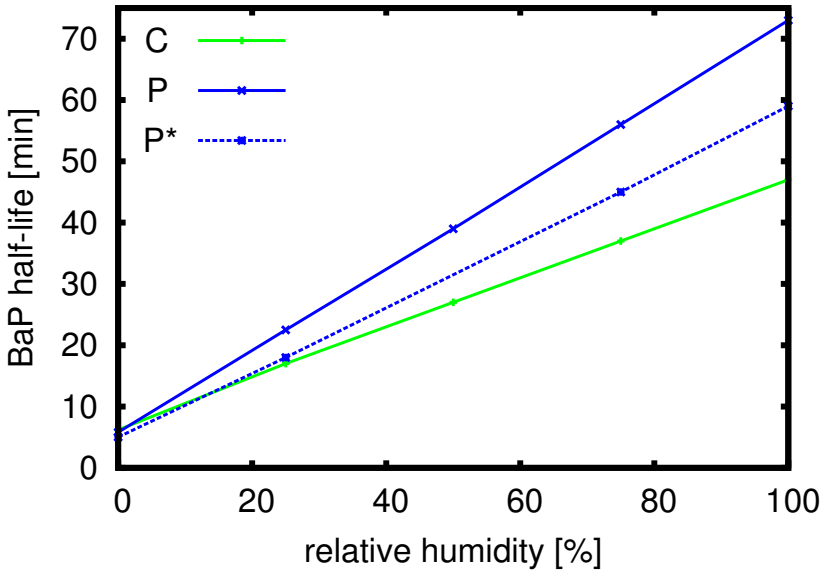

Figure 4.6: The BaP half-life is plotted as a function of relative humidity for scenarios C, P, and P*. Scenario C represents the co-adsorption of O_3, NO_2 and H_2O following the surface reactions given in Table 4.1 with an initial gas-phase O_3 concentration of 50 ppbv, an initial BaP surface concentration of 1×10^{14} cm^{-2}, and a temperature of 298.15 K. Scenario P represents the co-adsorption of O_3 and H_2O following surface reactions (1) to (3) from Table 4.1 with a constant gas-phase O_3 concentration of 30 ppbv, an initial BaP surface concentration of 1.8×10^{13} cm^{-2}, and a temperature of 296 K corresponding to the boundary conditions of an aerosol flow tube experiment conducted by Pöschl et al. [60]. Scenario P* represents the experimentally derived BaP half-lives from the aerosol flow tube experiment [60] with the same boundary conditions as used in scenario P.

from experimental data from the ozonolysis of soot coated with BaP [60]. Scenario P represents our modeling results using the experimental conditions of Pöschl et al. [60] as input parameters. These are a 30 ppbv constant gas-phase O_3 concentration, an initial BaP surface concentration of 1.8×10^{13} cm^{-2}, a temperature of 296 K, and O_3 and H_2O as adsorbing species. Other input parameters are identical to the ones listed in Table 4.1. Figure 4.6 shows that the simulated BaP half-lives in scenario P are slightly longer than the ones inferred from laboratory measurements [60] given by scenario P*. The simulated BaP half-lives in scenario P are 5.8 min for 0% RH, 22.5 min for 25% RH, and 56 min for 75% RH. The BaP half-lives in scenario P* as derived by Pöschl et al. [60] are 5 min for 0% RH, 18 min for 25%, and 45 min for

75% RH. Reasons for the longer simulated lifetimes in scenario P could be parameter sensitivity or physio-chemical processes that were not accounted for in our model approach. Regarding the former, a 20% reduction in the value for the effective molecular cross section of H_2O would result in half-lives in agreement with the measurements of Pöschl et al. [60]. Regarding the latter, physiochemical processes that are not captured in our model framework are, e.g., the diffusion of adsorbents through surface H_2O which could lead to surface oxidation and a reduction in the BaP half-life even though most reactive sites are occupied by H_2O. Also, changes in the soot particle's hydrophilicity could result in changes of the residence time of surface H_2O, subsequently affecting particle oxidation. A variation of the H_2O desorption time, τ_{H_2O}, of about $\pm 10\%$ due to possible changes in particle hydrophilicity changes the BaP lifetime by about ± 5 min.

O_3 Gas-Phase Feedback

In this section, we assess the gas-phase O_3 feedback from scenarios A, B, C, and from the emission scenarios A_{4x}, B_{4x}, C_{4x}, and A_{24x}, B_{24x}, C_{24x}. Figure 4.7 shows the temporal evolution of the gas-phase O_3 concentrations in these scenarios and a base scenario which does not include any heterogeneous reactions on soot. The diurnal cycle of gas-phase O_3 and the potential decreases in the gas-phase O_3 concentration due to the heterogeneous reactions implemented in our model scenarios can be clearly identified.

The gas-phase uptake in scenarios A, B, and C cause no significant decrease in the gas-phase O_3 concentration with respect to the base scenario. Detail 1 in Fig. 4.7 resolves the differences among scenarios A, B, C. The strongest O_3 depletion among these scenarios is 0.33 ppb in scenario B, which is less than 2‰ in comparison to the base scenario after the five days modeling period. The difference to the weakest O_3 depleting scenario C is less than 1‰. This insignificance of the gas-phase O_3 feedback from the non-emission scenarios is in agreement with previous studies [34, 63, 158] which considered O_3 depletion on soot surfaces as probably negligible under conditions relevant to the upper troposphere and lower stratosphere.

Figure 4.7 shows a larger gas-phase O_3 reduction for the low emission scenarios A_{4x}, B_{4x}, and C_{4x} in comparison to the non-emission scenarios A, B, C and the base scenario. Detail 2 in Fig. 4.7 indicates the strongest O_3 reduction for scenario B_{4x}, in which the O_3 concentration is 7.88 ppbv or 4.8% less than in the base scenario after the five days modeling period. The difference in O_3 concentration between scenarios B_{4x} and A_{4x} is less than 1%. In scenario C_{4x}, the O_3 concentration is decreased by 2.6% with respect to the base scenario, which is almost half the decrease of scenario B_{4x}.

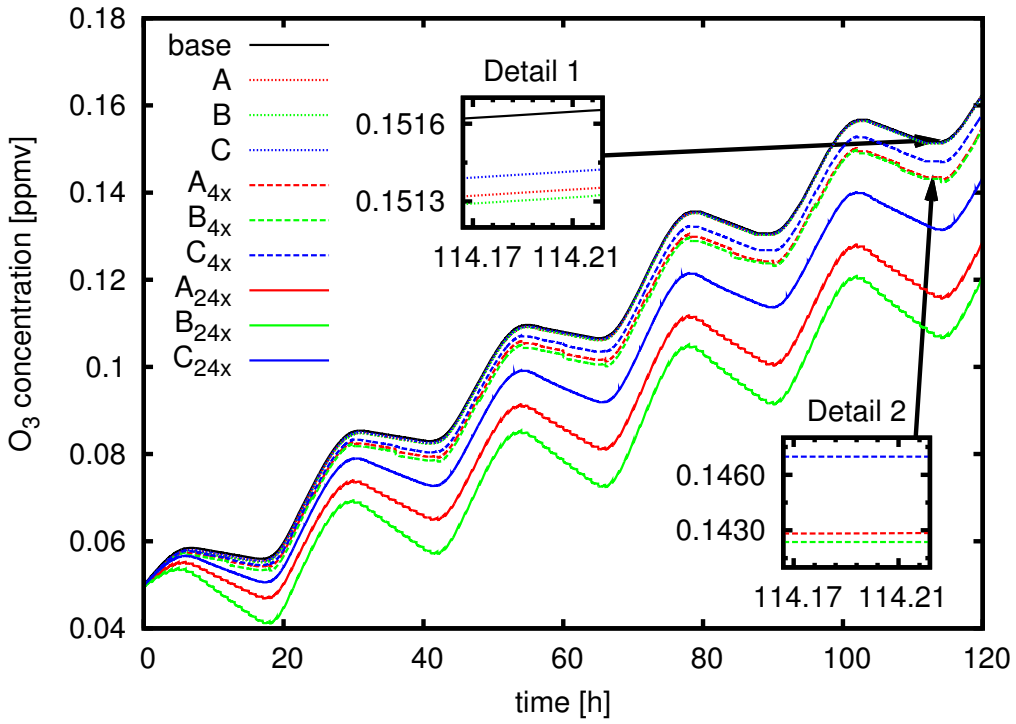

Figure 4.7: The temporal evolution of the gas-phase O_3 concentration is shown for a base scenario with no heterogeneous chemistry, for the model scenarios A, B, C, and the corresponding low and high emission scenarios A_{4x}, B_{4x}, C_{4x} and A_{24x}, B_{24x}, C_{24x}, respectively. Detail 1 shows an enlarged view of the results of the base scenario and model scenarios A, B, and C. Detail 2 shows an enlarged view of the results for the low emissions scenarios A_{4x}, B_{4x}, C_{4x}. Input parameters for the A, B, and C-scenarios are given in Table 4.1.

The high emission scenarios A_{24x}, B_{24x}, and C_{24x} exhibit the largest O_3 reductions. Figure 4.7 shows the lowest O_3 concentration for scenario B_{24x}, which is 41.6 ppbv or 25.6% less than the O_3 concentration for the base scenario after the five days modeling period. The scenarios A_{24x} and C_{24x} exhibit a decrease in O_3 concentration with respect to the base scenario of 33.8 ppbv and 19.2 ppbv, respectively. These reductions in the tropospheric O_3 concentration indicate that these heterogeneous reactions may have an impact on urban O_3 concentrations.

Figure 4.7 also shows clear differences in O_3 concentrations between the specific co-adsorption scenarios. The scenarios C, C_{4x}, and C_{24x} are associated with the least O_3 depletion in comparison to the A and B-scenarios. This is due to the co-adsorption of water vapor which hinders direct O_3 uptake by

constantly occupying over 75% of the total reactive surface as discussed in section 4.1.4. In terms of gas-phase O_3 reduction, the A-scenarios, in which only O_3 is taken up, do not deplete gas-phase O_3 concentrations as much as the B-scenarios, in which less O_3 is taken up by the soot surface directly. However, the additional NO_2 uptake in the B-scenarios affects the gas-phase NO_x-O_3 production cycle leading to a lower O_3 concentration than in cases with no NO_2 uptake. Consequently, no clear relationship between the number of adsorbing species and the resulting O_3 depletion can be established. As can also be seen from Fig. 4.7, the relative difference in gas-phase O_3 concentrations between the A, B, and C-scenarios increases disproportionately from the non-emission and low emission scenarios to the high emission scenarios. This highlights the non-linear behavior of the gas-phase O_3 depletion due to the co-adsorption of the interdependent species O_3 and NO_2, and the rapid co-adsorption of H_2O.

Since there is a wide range of measured uptake coefficients for NO_2 on soot, ranging from smaller than 4×10^{-8} to 0.12 [72], we simulated the B-scenarios with accommodation coefficients of $\alpha_{NO_2}=10^{-6}$ [69] and $\alpha_{NO_2}=10^{-3}$ [70]. These lower initial uptake coefficients yield, within 1 ppbv, the same gas-phase feedback as the A-scenarios, which have no NO_2 co-adsorption implemented. Thus, the gas-phase feedback from the co-adsorption of NO_2 obeying an accommodation coefficient smaller than 10^{-3} is negligible.

It should be noted that the feedback on the gas-phase O_3 concentration from the desorption of HONO in surface reaction (5) given in Table 4.1 was found to be negligible for all model scenarios due to the small production rate in relation to gas-phase production. The HONO production rate from desorption is 0.22 $ppmv^{-1}$ min^{-1} which is five orders of magnitude smaller than the gas-phase production rate of NO with OH. In the mornings, the gas-phase HONO production temporarily decreases due to low OH concentrations, but surface desorption is still one order of magnitude smaller than the gas-phase production and thus does not exert a significant influence.

The error in both emission scenarios from neglecting gas-phase uptake on disregarded surface sites can be estimated with reference to section 4.1.4 and Fig. 4.2. Figure 4.2 shows that, for each adsorption scenario, the uptake coefficients decrease by more than three orders of magnitude or 99.9% within the first six hours of simulation time. Therefore, the error in the low emission scenarios from neglecting gas-phase uptake on soot surfaces that are older than six hours is not significant. After one hour of simulation time, the uptake coefficients fall by one to two orders of magnitude, depending on the scenario. Thus, up to 10% of gas-phase uptake is neglected in the high emission scenarios due to an hourly replenishing time, which results in a small underestimate of the total gas-phase uptake.

In the next section, we compare the gas-phase feedback from heterogeneous chemistry obtained in this section for the dynamic uptake coefficient approach with the gas-phase feedback obtained from the use of constant uptake coefficients.

Constant Uptake Parameterizations of O_3 Gas-Phase Feedback

To study the gas-phase feedback from a heterogeneous modeling approach employing constant uptake coefficients, we implement the experimentally determined constant uptake coefficients of $\gamma_{O_3} = 1 \times 10^{-3}$ for O_3 uptake [60], $\gamma_{NO_2} = 0.14$ for NO_2 uptake [71], and $\gamma_{H_2O} = 0.4 \times 10^{-3}$ for the uptake of water vapor [67] into the non-emission scenarios A, B, and C. These γ_{Xi}-values represent initial uptake coefficients that were previously implemented in our model as accommodation coefficients. The gas-phase loss is computed according to Eq. (4.12) with the same input parameters, particle surface concentration and gas-phase concentrations that were previously used in scenarios A, B, and C. We denote these constant uptake coefficient scenarios by A_{const}, B_{const}, C_{const}. Application of constant uptake coefficients reduced the computation time by a factor of about 18 compared to a dynamic uptake approach and needed roughly the same time as a simulation without any heterogeneous reactions implemented.

Figure 4.8 shows the temporal evolution of the gas-phase O_3 concentration for scenarios A_{const}, B_{const}, C_{const} and for a base scenario without heterogeneous chemistry. After two hours of modeling time, the gas-phase O_3 concentration in the constant uptake coefficient scenarios A_{const}, B_{const}, and C_{const} falls by more than one order of magnitude and is approaching zero. This fast depletion of O_3 is due to the fact that the gas-phase uptake is not limited by surface saturation, which otherwise would decrease by reducing the uptake coefficients according to Eq. (4.11). The uptake is now solely determined by the adsorbents' constant uptake coefficients, their molecular velocities, and their gas-phase concentrations via Eq. (4.12). This results also in a different ordering of scenarios in terms of their O_3 depletion efficiency when compared to the dynamic uptake scenarios. Scenario A_{const} shows the least gas-phase O_3 depletion, since it employs the lowest uptake coefficient. Scenarios B_{const} and C_{const} show the same O_3 depletion, since in this constant uptake coefficient approach, the co-adsorption of water vapor in scenario C_{const} does not reduce the gas-phase uptake of O_3 and NO_2 which therefore is the same as in scenario B_{const}.

Clearly, these constant uptake coefficient scenarios do not represent the underlying physical and chemical processes and result in an unrealistically high gas-phase O_3 depletion which may not describe typical urban plume conditions.

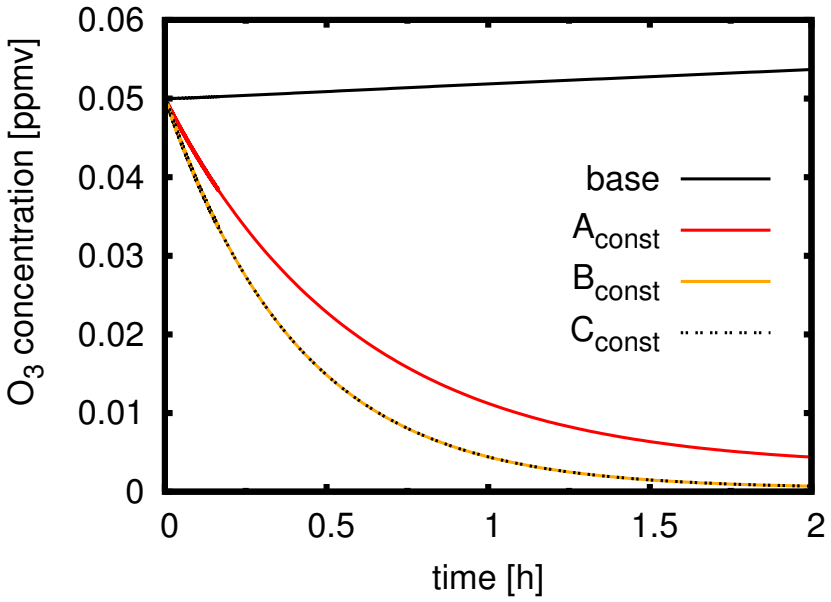

Figure 4.8: The temporal evolution of the gas-phase O_3 concentration is shown for a base scenario with no heterogeneous chemistry and for the constant uptake scenarios A_{const}, B_{const}, C_{const}. Scenarios A_{const}, B_{const}, C_{const} use constant uptake coefficients of $\gamma_{O_3} = 1 \times 10^{-3}$ [60, 65], $\gamma_{NO_2} = 0.14$ [71, 117], and $\gamma_{H_2O} = 0.4 \times 10^{-3}$ [60, 67] but are otherwise equivalent to scenarios A, B, and C as defined in Table 4.1.

In addition to using the initial uptake coefficients as constant uptake values, we also attempted to parameterize the uptake process by several time-specific uptake values modeled after the temporal evolution of the uptake coefficients as shown in Fig. 4.2. Neither a 3-step uptake parametrization, nor a 2-step one using an initial uptake value from laboratory measurements and subsequent values from our model was successful in capturing the O_3 depleting effect. Application of a single constant uptake value for each adsorbent yielded acceptable agreement with the gas-phase O_3 concentration of the respective model scenarios, if an uptake value was chosen significantly different from the laboratory measurements and model results. However, this approach is only successful for a certain time frame and certain boundary conditions, such as initial gas-phase concentrations. Furthermore, the adsorbent-specific uptake values determined in such a way, could not be used to capture the combined effect on the O_3 concentration of two or more adsorbents. Thus, the uptake values obtained in this manner are heavily scenario dependent and therefore of little use in general atmospheric models. These difficulties in obtaining a

simplified and thus computationally more efficient description of the uptake process clearly indicate the underlying complexity of the involved physical-chemical mechanisms, emphasizing the need for a detailed modeling framework to accurately resolve the uptake process.

4.1.5 Conclusions

The PRA framework [12], which allows a dynamic uptake coefficient treatment, was coupled to a box model version of the gas-phase solver RADM2 [13] to model heterogeneous reactions of O_3, NO_2, and water vapor on soot coated with benzo[a]pyrene for a period of five days. Gas-phase reactions and emissions were based on an urban plume scenario [100]. This allowed us to study, in detail, the heterogeneous kinetics and its dependency on diurnal changes in gas-phase composition due to photochemical processes.

A detailed analysis of surface chemistry showed that the O_3 and NO_2 uptake coefficients vary by more than five orders of magnitude due to competition for reactive surface sites and changes in gas-phase composition. Within the first six hours of simulation time, the uptake coefficients decrease by more than three orders of magnitude or 99.9%. From day two to five, periodic peaks of the uptake coefficient follow the diurnal cycle of the adsorbents' gas-phase concentrations.

The half-life of BaP was found to increase with the number of co-adsorbing species. Physisorption of water vapor increased the BaP half-life by a factor of five to seven by permanently occupying about 75% of the surface and thereby delaying the surface reactions of O_3 and NO_2. The BaP half-life increases linearly with RH and the linearity is preserved under changes in O_3 and BaP concentrations, temperature, and number of adsorbing species. Our results show that even at low RH, the adsorption of water vapor can play a major role in soot surface chemistry. An increase from 0% RH to 25% RH increases the BaP half-life by a factor of three.

This study indicates the importance of the co-adsorption of water vapor for heterogeneous chemistry also for aerosol particles other than soot coated with BaP. Since BaP belongs to the group of polycyclic aromatic hydrocarbons which are known to be hydrophobic [159], an even greater impact of water vapor co-adsorption on surface chemistry can be expected for more hydrophilic surfaces. While our model does not capture changes in hydrophilicity, it assesses surface oxidation which is thought to influence the activation of tropospheric aerosols as cloud condensation nuclei (CCN) [61, 90, 137, 160, 161]. Our modeling approach is able to estimate surface oxidation times, such as the BaP half-life, in an atmospheric context and may therefore be used in part to derive CCN activation times.

We also assessed the feedback of heterogeneous uptake on the gas-phase O_3 concentration. The different co-adsorption scenarios with no soot emissions implemented showed no significant feedback on the gas-phase composition. However, two emission scenarios in which reactive surface sites are replenished every six hours and every hour induced significant changes in the gas-phase O_3 concentration. The largest O_3 depletions were observed for the hourly high emission scenario with a reduction in O_3 concentration of up to 41.6 ppbv or 25% for the co-adsorption of O_3 and NO_2. It also resulted in a reduction of 33.8 ppbv or 21% for the scenario with the adsorption of O_3, and of 19.2 ppbv or 11.8% for the scenario with the co-adsorption of O_3, NO_2 and water vapor. In comparison, the low emission scenarios replenishing reactive sites every six hours showed a decrease in gas-phase O_3 concentration of maximum 7.8 ppbv or 5%. Hence, our conceptual study employing soot particles in an urban environment indicates that heterogeneous chemistry has the potential to significantly alter the gas-phase composition.

Our model results indicate that the uptake is sensitive to the co-adsorbing species and their interactions with each other. The scenario with the most O_3 uptake from the exclusive adsorption of O_3 is surpassed in overall gas-phase O_3 reduction by the scenario in which O_3 and NO_2 co-adsorb. This is due to the additional O_3 reduction induced by the gas-phase reactions between O_3 and NO_2. This exemplifies the non-linear feedbacks obtained from a co-adsorption scheme.

Although heterogeneous reactions can be an important source for nitrous acid (HONO) [162], the desorption of HONO from surface reactions of NO_2 on soot particles was found to be negligible for the gas-phase O_3 concentration.

We compared the dynamic uptake coefficient approach with a constant uptake coefficients approach. The use of experimentally determined reactive uptake coefficients which were kept constant in these model scenarios led to an almost complete gas-phase O_3 depletion after two hours of modeling time which is highly unrealistic for an urban plume scenario. Since surface conditions and reactions were not related to the uptake dynamics in these constant uptake coefficient scenarios, the co-adsorption of water vapor had no impact on the efficiency of gas-phase O_3 depletion which ignores the underlying physical and chemical picture and is in contrast to the results from the dynamic uptake coefficient approach.

It should be noted that modeling studies used constant uptake coefficients, but employed consumable reactive sites on the soot surface to account for surface passivation [115]. This approach yields a more physical picture of the gas-phase uptake, but it still lacks the accurate description of the heterogeneous kinetics involving the interdependence of gas-phase and adsorbed surface

species. Our study showed that the superposition of fixed reactive uptake coefficients, despite being experimentally determined, can result in erroneous results for the overall uptake efficiency and thus gas-phase composition.

Other modeling studies used empirical parameterizations of the uptake coefficient as a function of relative humidity, temperature, and aerosol type [120, 121]. As such, the parametrization of N_2O_5 hydrolysis yields gas-phase concentrations in good agreement with climatological observations [120]. This may be due to the fact that the N_2O_5 hydrolysis in aqueous aerosol particles follows an absorption type reaction mechanism [143, 144, 163], i.e., the uptake can be dominated by dissolution of the gas-phase species into the particle governed by Henry's law constant and by subsequent reaction in the bulk [2]. In such heterogeneous processes, gas-phase species do not compete for reactive surface sites, which therefore have no effect on the subsequent uptake. In contrast, heterogeneous reactions following adsorption kinetics may predominantly occur at the surface of solid or crystalline particles [90] and aqueous surfaces coated by an organic surfactant [164]. This limits the available number of reactive surface sites in comparison to the bulk liquid. Therefore, higher order reactive uptake processes such as Langmuir-Hinshelwood surface reactions will not be correctly represented by the application of constant reactive uptake coefficients.

This study clearly emphasizes the need for laboratory data of physical and chemical parameters for atmospherically relevant adsorbents and aerosols to predict, in detail, the effects of heterogeneous chemistry on the gas-phase and aerosol composition.

Acknowledgements The authors are grateful for helpful discussions with M. Ammann.

Bibliography

[115] Aklilu, Y. A. and Michelangeli, D. V.: Box model investigation of the effect of soot particles on ozone downwind from an urban area through heterogeneous reactions, Environ. Sci. Technol., 38, 5540–5547, doi:10.1021/es035079x, 2004.

[117] Ammann, M. and Pöschl, U.: Kinetic model framework for aerosol and cloud surface chemistry and gas-particle interactions - Part 2: Exemplary practical applications and numerical simulations, Atmos. Chem. Phys. , 7, 6025–6045, 2007.

[116] Ammann, M., Rössler, E., Baltensperger, U., and M., K.: Heterogeneous reaction of NO_2 on bulk soot samples, Laboratory of Radio- and Environmental Chemistry Annual Report 1997, Paul Scherrer Institute, Switzerland, 24, 1997.

[68] Ammann, M., Kalberer, M., Jost, D., Tobler, L., Rössler, E., Piguet, D., Gaggeler, H., and Baltensperger, U.: Heterogeneous production of nitrous acid on soot in polluted air masses, Nature, 395, 157–160, 1998.

[33] Arens, F., Gutzwiller, L., Baltensperger, U., Gaggeler, H., and Ammann, M.: Heterogeneous reaction of NO_2 on diesel soot particles, Environ. Sci. Technol., 35, 2191–2199, 2001.

[150] Arens, F., Gutzwiller, L., Gaggeler, H. W., and Ammann, M.: The reaction of NO_2 with solid anthrarobin (1,2,10-trihydroxy-anthracene), Phys. Chem. Chem. Phys., 4, 3684–3690, doi:10.1039/b201713j, 2002.

[127] Atkinson, R., Baulch, D. L., Cox, R. A., Crowley, J. N., Hampson, Jr. R. F., Kerr, J. A., Rossi, M. J., and Troe, J.: Summary of Evaluated Kinetic and Photochemical Data for Atmospheric Chemistry, Web Version, URL `www.iupac-kinetic.ch.cam.ac.uk`, University of Cambridge, UK, 2001.

[72] Aubin, D. G. and Abbatt, J. P. D.: Interaction of NO_2 with hydrocarbon soot: Focus on HONO yield, surface modification, and mechanism, J. Phys. Chem. A, 111, 6263–6273, doi:10.1021/jp068884h, 2007.

[149] Bernstein, J. A., Alexis, N., Barnes, C., Bernstein, I. L., Bernstein, J. A., Nel, A., Peden, D., Diaz-Sanchez, D., Tarlo, S. M., and Williams, P. B.: Health effects of air pollution, J. Allergy Clin. Immun., 114, 1116–1123, doi:10.1016/j.jaci.2004.08.030, 2004.

[151] Bertram, A. K. and Ivanov, A. V. and Hunter, M. and Molina, L. T. and Molina, M. J.: The reaction probability of OH on organic surfaces of tropospheric interest, J. Phys. Chem. A, 105, 9415–9421, 2001.

[15] Bey, I., Jacob, D. J., Yantosca, R. M., Logan, J. A., Field, B. D., Fiore, A. M., Li, Q. B., Liu, H. G. Y., Mickley, L. J., and Schultz, M. G.: Global modeling of tropospheric chemistry with assimilated meteorology: Model description and evaluation, J. Geophys. Res-Atmos., 106, 23 073–23 095, 2001.

[136] Bond, T. C., Streets, D. G., Yarber, K. F., Nelson, S. M., Woo, J. H., and Klimont, Z.: A technology-based global inventory of black and organic carbon emissions from combustion, J. Geophys. Res.-Atmos., 109, doi: 10.1029/2003JD003697, 2004.

[140] Brown, S. S., Ryerson, T. B., Wollny, A. G., Brock, C. A., Peltier, R., Sullivan, A. P., Weber, R. J., Dube, W. P., Trainer, M., Meagher, J. F., Fehsenfeld, F. C., and Ravishankara, A. R.: Variability in nocturnal nitrogen oxide processing and its role in regional air quality, Science, 311, 67–70, doi:10.1126/science.1120120, 2006.

[93] Chang, J. S., Brost, R. A., Isaksen, I. S. A., Madronich, S., Middleton, P., Stockwell, W. R., and Walcek, C. J.: A Three-Dimensional Eulerian Acid Deposition Model - Physical Concepts and Formulation, J. Geophys. Res.-Atmos., 92, 14 681–14 700, 1987.

[15] Cheung, J. L., Li, Y. Q., Boniface, J., Shi, Q., Davidovits, P., Worsnop, D. R., Jayne, J. T., and Kolb, C. E.: Heterogeneous interactions of NO_2 with aqueous surfaces, J. Phys. Chem. A, 104, 2655–2662, 2002.

[135] Choi, W. and Leu, M. T.: Nitric acid uptake and decomposition on black carbon (soot) surfaces: Its implications for the upper troposphere and lower stratosphere, J. Phys. Chem. A, 102, 7618–7630, 1998.

[17] Cosman, L. M., Knopf, D. A., and Bertram, A. K.: N_2O_5 reactive uptake on aqueous sulfuric acid solutions coated with branched and straight-chain insoluble organic surfactants, J. Phys. Chem. A, 112, 2386–2396, 2008.

[8] Crutzen, P. J. and Arnold, F.: Nitric-acid cloud formation in the cold antarctic stratosphere - a major cause for the springtime ozone hole, Nature, 324, 651–655, 1986.

[80] Danckwerts, P. V.: Absorption by simultaneous diffusion and chemical reaction into particles of various shapes and into falling drops, T. Faraday. Soc., 47, 1014–1023, 1951.

[121] Davis, J. M., Bhave, P. V., and Foley, K. M.: Parameterization of N_2O_5 reaction probabilities on the surface of particles containing ammonium, sulfate, and nitrate, Atmos. Chem. Phys, 8, 5295–5311, 2008.

[138] Dentener, F. J., Carmichael, G. R., Zhang, Y., Lelieveld, J., and Crutzen, P. J.: Role of mineral aerosol as a reactive surface in the global troposphere, J. Geophys. Res-Atmos., 101, 22 869–22 889, 1996.

[128] Derwent, R. G. and Jenkin, M. E.: Hydrocarbons and the Long-range Transport of Ozone and PAN Across Europe, Atmos. Environ. A-Gen., 25, 1661–1678, 1991.

[63] Disselkamp, R. S., Carpenter, M. A., Cowin, J. P., Berkowitz, C. M., Chapman, E. G., Zaveri, R. A., and Laulainen, N. S.: Ozone loss in soot aerosols, J. Geophys. Res-Atmos., 105, 9767–9771, 2000.

[24] Donaldson, D. J. and Vaida, V.: The Influence of Organic Films at the Air-Aqueous Boundary on Atmospheric Processes, Chem. Rev., 106, 1445–1461, doi:10.1021/cr040367c, 2006.

[38] Dymarska, M., Murray, B. J., Sun, L. M., Eastwood, M. L., Knopf, D. A., and Bertram, A.: Deposition ice nucleation on soot at temperatures relevant for the lower troposphere, J. Geophys. Res-Atmos., 111, D04204, doi:10.1029/2005JD006627, 2006.

[118] EPA, U. S.: 2006 Edition of the Drinking Water Standards and Health Advisories, U.S. Environmental Protection Agency, Washington, DC, epa 822-r-06-013 edn., 18pp., 2006.

[119] EPA, U. S.: Air Quality Criteria for Ozone and Related Photochemical Oxidants (Final), U.S. Environmental Protection Agency, Washington, DC, epa/600/r-05/004af-cf edn., 821 pp., 2006.

[120] Evans, M. J. and Jacob, D. J.: Impact of new laboratory studies of N_2O_5 hydrolysis on global model budgets of tropospheric nitrogen oxides, ozone, and OH, Geophys. Res. Lett., 32, L09813, doi:10.1029/2005GL022469, 2005.

[146] Finlayson-Pitts, B. J. and Pitts, J. N.: Tropospheric air pollution: Ozone, airborne toxics, polycyclic aromatic hydrocarbons, and particles, Science, 276, 1045–1052, 1997.

[2] Finlayson-Pitts, B. J. and Pitts, J. N.: Chemistry of the Upper and Lower Atmosphere, Academic Press, San Diego, 969pp., 2000.

[147] Franze, T., Weller, M. G., Niessner, R., and Pöschl, U.: Enzyme immunoassays for the investigation of protein nitration by air pollutants, Analyst, 128, 824–831, doi:10.1039/b303132b, 2003.

[148] Franze, T., Weller, M. G., Niessner, R., and Pöschl, U.: Protein nitration by polluted air, Environ. Sci. Technol., 39, 1673–1678, doi: 10.1021/es0488737, 2005.

[83] Fuchs, N. A. and Sutugin, A. G.: High-dispersed aerosols, in: Topics in current aerosol research,, edited by: Hidy, G. M. and Brock, J. R., Pergamon, New York, 1971.

[71] Gerecke, A., Thielmann, A., Gutzwiller, L., and Rossi, M. J.: The chemical kinetics of HONO formation resulting from heterogeneous interaction of NO_2 with flame soot, Geophys. Res. Lett., 25, 2453–2456, 1998.

[122] Grell, G. A., Peckham, S. E., Schmitz, R., McKeen, S. A., Frost, G., Skamarock, W. C., and Eder, B.: Fully coupled "online" chemistry within the WRF model, Atmos. Env., 39, 6957–6975, 2005.

[78] Gross, S. and Bertram, A. K.: Reactive Uptake of NO_3, N_2O_5, NO_2, HNO_3, and O_3 on Three Types of Polycyclic Aromatic Hydrocarbon Surfaces, J. Phys. Chem. A, 112, 3104–3113, 2008.

[155] Gross, S. and Bertram, A. K.: Products and kinetics of the reactions of an alkane monolayer and a terminal alkene monolayer with NO_3 radicals, J. Geophys. Res.-Atmos., 114, doi:10.1029/2008JD010987, 2009.

[163] Hanson, D. R. and Ravishankara, A. R.: The reaction probabilities of $ClONO_2$ and N_2O_5 on 40-percent to 75-percent sulfuric-acid-solutions, J. Geophys. Res.-Atmos., 96, 17 307–17 314, 1991.

[153] Hearn, J. D. and Smith G. D.: A mixed-phase relative rates technique for measuring aerosol reaction kinetics, Geophys. Res. Lett., 33, doi:10.1029/2006GL026963, 2006.

[157] Homann, K. H.: Fullerenes and soot formation - New pathways to large particles in flames, Angew. Chem., Int. Ed, 37, 2435–2451, 1998.

[158] Kamm, S., Mohler, O., Naumann, K. H., Saathoff, H., and Schurath, U.: The heterogeneous reaction of ozone with soot aerosol, Atmos. Environ., 33, 4651–4661, 1999.

[137] Kanakidou, M., Seinfeld, J. H., Pandis, S. N., Barnes, I., Dentener, F. J., Facchini, M. C., Van Dingenen, R., Ervens, B., Nenes, A., Nielsen, C. J., Swietlicki, E., Putaud, J. P., Balkanski, Y., Fuzzi, S., Horth, J., Moortgat, G. K., Winterhalter, R., Myhre, C. E. L., Tsigaridis, K., Vignati, E., Stephanou, E. G., and Wilson, J.: Organic aerosol and global climate modelling: a review, Atmos. Chem. Phys., 5, 1053–1123, 2005.

[141] Karagulian, F., Santschi, C., and Rossi, M. J.: The heterogeneous chemical kinetics of N_2O_5 on $CaCO_3$ and other atmospheric mineral dust surrogates, Atmos. Chem. Phys., 6, 1373–1388, 2006.

[70] Kirchner, U. and Scheer, V. and Vogt, R.: FTIR spectroscopic investigation of the mechanism and kinetics of the heterogeneous reactions of NO_2 and HNO_3 with soot, J. Phys. Chem. A, 104, 8908–8915, 2000.

[69] Kleffmann, J., Becker, K. H., Lackhoff, M., and Wiesen, P.: Heterogeneous conversion of NO_2 on carbonaceous surfaces, Phys. Chem. Chem. Phys., 1, 5443–5450, 1999.

[143] Knopf, D. A., Cosman, L. M., Mousavi, P., Mokamati, S., and Bertram, A. K.: A novel flow reactor for studying reactions on liquid surfaces coated by organic monolayers: Methods, validation, and initial results, J. Phys. Chem. A, 111, 11021–11032, 2007.

[142] Knopf, D. A., Mak, J., Gross, S., and Bertram, A. K.: Does atmospheric processing of saturated hydrocarbon surfaces by NO_3 lead to volatilization?, Geophys. Res. Lett., 33, doi:10.1029/2006GL026884, 2006.

[100] Kuhn, M., Builtjes, P. J. H., Poppe, D., Simpson, D., Stockwell, W. R., Andersson-Skold, Y., Baart, A., Das, M., Fiedler, F., Hov, O., Kirchner, F., Makar, P. A., Milford, J. B., Roemer, M. G. M., Ruhnke, R., Strand, A., Vogel, B., and Vogel, H.: Intercomparison of the gas-phase chemistry

in several chemistry and transport models, Atmos. Environ., 32, 693–709, 1998.

[131] Letzel, T., Pöschl, U., Rosenberg, E., Grasserbauer, M., and Niessner, R.: In-source fragmentation of partially oxidized mono- and polycyclic aromatic hydrocarbons in atmospheric pressure chemical ionization mass spectrometry coupled to liquid chromatography, Rapid Commun. Mass Spectrom., 13, 2456–2468, 1999.

[59] Letzel, T., Rosenberg, E., Wissiack, R., Grasserbauer, M., and Niessner, R.: Separation and identification of polar degradation products of benzo[a]pyrene with ozone by atmospheric pressure chemical ionization-mass spectrometry after optimized column chromatographic clean-up, J. Chromatogr., A, 855, 501–514, 1999.

[132] Letzel, T., Pöschl, U., Wissiack, R., Rosenberg, E., Grasserbauer, M., and Niessner, R.: Phenyl-modified reversed-phase liquid chromatography coupled to atmospheric pressure chemical ionization mass spectrometry: A universal method for the analysis of partially oxidized aromatic hydrocarbons, Anal. Chem., 73, 1634–1645, doi:10.1021/ac001079t, 2001.

[156] Massman, W. J.: A review of the molecular diffusivities of H_2O, CO_2, CH_4, CO, O_3, SO_2, NH_3, N_2O, NO, and NO_2 in air, O_2 and N_2 near STP, Atmos. Environ., 32, 1111–1127, 1998.

[10] Molina, M. J., Tso, T. L., Molina, L. T., and Wang, F. C. Y.: Antarctic Stratospheric Chemistry of Chlorine Nitrate, Hydrogen Chloride and Ice - Release of Active Chlorine, Science, 238, 1253–1257, 1987.

[152] Molina, M. J., Ivanov, A. V., Trakhtenberg, S. and Molina, L. T.: Atmospheric evolution of organic aerosol, Geophys. Res. Lett., 31, doi: 10.1029/2004GL020910, 2004.

[34] Nienow, A. M. and Roberts, J. T.: Heterogeneous chemistry of carbon aerosols, Annu. Rev. Phys. Chem., 57, 105–128, doi:10.1146/annurev.physchem.57.032905.104525, 2006.

[130] Nishino, J.: Adsorption of water vapor and carbon dioxide at carboxylic functional groups on the surface of coal, Fuel, 80, 757–764, 2001.

[145] Osthoff, H. D., Roberts, J. M., Ravishankara, A. R., Williams, E. J., Lerner, B. M., Sommariva, R., Bates, T. S., Coffman, D., Quinn, P. K., Dibb, J. E., Stark, H., Burkholder, J. B., Talukdar, R. K., Meagher, J., Fehsenfeld, F. C., and Brown, S. S.: High levels of nitryl chloride in

the polluted subtropical marine boundary layer, Nature Geoscience, 1, 324–328, doi:10.1038/ngeo177, 2008.

[154] Park, J. H., Ivanov A. V., and Molina, M. J.: Effect of relative humidity on OH uptake by surfaces of atmospheric importance, J. Phys. Chem. A, 112, 6968–6977, 2008.

[160] Petters, M. D., Prenni, A. J., Kreidenweis, S. M., DeMott, P. J., Matsunaga, A., Lim, Y. B., and Ziemann, P. J.: Chemical aging and the hydrophobic-to-hydrophilic conversion of carbonaceous aerosol, Geophys. Res. Lett., 33, 1107–1118, 2006.

[37] Popovicheva, O. B., Persiantseva, N. M., Tishkova, V., Shonija, N. K., and Zubareva, N. A.: Quantification of water uptake by soot particles, Environ. Res. Lett., 3, 025009, doi:10.1088/1748-9326/3/2/025009, 2008.

[133] Pöschl, U.: Formation and decomposition of hazardous chemical components contained in atmospheric aerosol particles, J. Aerosol Med., 15, 203–212, 2002.

[29] Pöschl, U.: Atmospheric aerosols: Composition, transformation, climate and health effects, Angew. Chem., Int. Ed, 44, 7520–7540, doi:10.1002/anie.200501122, 2005.

[60] Pöschl, U., Letzel, T., Schauer, C., and Niessner, R.: Interaction of ozone and water vapor with spark discharge soot aerosol particles coated with benzo[a]pyrene: O_3 and H_2O adsorption, benzo[a]pyrene degradation, and atmospheric implications, J. Phys. Chem. A, 105, 4029–4041, 2001.

[12] Pöschl, U., Rudich, Y., and Ammann, M.: Kinetic model framework for aerosol and cloud surface chemistry and gas-particle interactions - Part 1: General equations, parameters, and terminology, Atmos. Chem. Phys., 7, 5989–6023, 2007.

[67] Rogaski, C. A., Golden, D. M., and Williams, L. R.: Reactive uptake and hydration experiments on amorphous carbon treated with NO_2, SO_2, O_3, HNO_3, and H_2SO_4, Geophys. Res. Lett., 24, 381–384, 1997.

[159] Rogge, W. F., Mazurek, M. A., Hildemann, L. M., Cass, G. R., and Simoneit, B. R. T.: Quantification of urban organic aerosols at a molecular-level - identification, abundance and seasonal-variation, Atmos. Environ. A-Gen., 27, 1309–1330, 1993.

[90] Rudich, Y.: Laboratory perspectives on the chemical transformations of organic matter in atmospheric particles, Chem. Rev., 103, 5097–5124, doi:10.1021/cr020508f, 2003.

[61] Rudich, Y., Donahue, N. M., and Mentel, T. F.: Aging of organic aerosol: Bridging the gap between laboratory and field studies, Annu. Rev. Phys. Chem., 58, 321–352, doi:10.1146/annurev.physchem.58.032806.104432, 2007.

[21] Saathoff, H., Naumann, K. H., Riemer, N., Kamm, S., Mohler, O., Schurath, U., Vogel, H., and Vogel, B.: The loss of NO_2, HNO_3, NO_3/N_2O_5, and $HO_2/HOONO_2$ on soot aerosol: A chamber and modeling study, Geophys. Res. Lett., 28, 1957–1960, 2001.

[82] Schwartz, S. E.: NATO ASI Series, chapter: Mass-transport considerations pertinent to aqueous phase reactions of gases in liquid-water clouds, Chemistry of Multiphase Atmospheric 15 Systems, vol. G6, 415 pp., Springer, Berlin, Germany, 1986.

[81] Schwartz, S. E. and Freiberg, J. E.: Mass-transport limitation to the rate of reaction of gases in liquid droplets - Application to oxidation of SO_2 in aqueous-solutions, Atmos. Environ., 15, 1129–1144, 1981.

[16] Seinfeld, J. H. and Pandis, S.: Atmospheric Chemistry and Physics: From Air Pollution to Climate Change, Wiley-Interscience, New York, 2006.

[139] Seisel, S., Borensen, C., Vogt, R., and Zellner, R.: Kinetics and mechanism of the uptake of N_2O_5 on mineral dust at 298 K, Atmos. Chem. Phys., 5, 3423–3432, 2005.

[161] Shilling, J. E., King, S. M., Mochida, M., and Martin, S. T.: Mass spectral evidence that small changes in composition caused by oxidative aging processes alter aerosol CCN properties, J. Phys. Chem. A, 111, 3358–3368, doi:10.1021/jp068822r, 2007.

[62] Smith, D. M. and Chughtai, A. R.: Reaction kinetics of ozone at low concentrations with n-hexane soot, J. Geophys. Res-Atmos., 101, 19 607–19 620, 1996.

[11] Solomon, S., Mills, M., Heidt, L. E., Pollock, W. H., and Tuck, A. F.: On the evaluation of ozone depletion potentials, J. Geophys. Res-Atmos., 97, 825–842, 1992.

[162] Stemmler, K., Ammann, M., Donders, C., Kleffmann, J., and George, C.: Photosensitized reduction of nitrogen dioxide on humic acid as a source of nitrous acid, Nature, 440, 195–198, doi:10.1038/nature04603, 2006.

[65] Stephens, S., Rossi, M. J., and Golden, D. M.: The heterogeneous reaction of ozone on carbonaceous surfaces, Int. J. Chem. Kinet., 18, 1133–1149, 1986.

[13] Stockwell, W. R., Middleton, P., Chang, J. S., and Tang, X. Y.: The 2nd generation regional acid deposition model chemical mechanism for regional air-quality modeling, J. Geophys. Res-Atmos., 95, 16 343–16 367, 1990.

[80] Stockwell, W. R., Kirchner, F., Kuhn, M. and Seefeld, S.: A new mechanism for regional atmospheric chemistry modeling, J. Geophys. Res.-Atmos., 102, 25847–25879, 1997.

[134] Tabor, K., Gutzwiller, L., and Rossi, M. J.: Heterogeneous Chemical-Kinetics of NO_2 on Amorphous-Carbon at Ambient-Temperature, J. Phys. Chem., 98, 6172–6186, 1994.

[66] Thomas, E. R., Frost, G. J., and Rudich, Y.: Reactive uptake of ozone by proxies for organic aerosols: Surface-bound and gas-phase products, J. Geophys. Res-Atmos., 106, 3045–3056, 2001.

[14] Tie, X., Brasseur, G., Emmons, L., Horowitz, L., and Kinnison, D.: Effects of aerosols on tropospheric oxidants: A global model study, J. Geophys. Res-Atmos., 106, 22 931–22 964, 2001.

[123] Tie, X., Madronich, S., Li, G. H., Ying, Z., Zhang, R., Garcia, A. R., Lee-Taylor, J., and Liu, Y.: Characterizations of chemical oxidants in Mexico City: A regional chemical dynamical model (WRF-Chem) study, Atmos. Env., 41, 1989–2008, 2007.

[35] Van Gulijk, C., Marijnissen, J. C. M., Makkee, M., Moulijn, J. A., and Schmidt-Ott, A.: Measuring diesel soot with a scanning mobility particle sizer and an electrical low-pressure impactor: performance assessment with a model for fractal-like agglomerates, J. Aerosol. Sci., 35, 633–655, doi:10.1016/j.jaerosci.2003.11.004, 2004.

[114] Vogel, B., Vogel, H., Kleffmann, J., and Kurtenbach, R.: Measured and simulated vertical profiles of nitrous acid - Part II. Model simulations and indications for a photolytic source, Atmos. Environ., 37, 2957–2966, doi:10.1016/S1352-2310(03)00243-7, 2003.

Here ends the reprint of the academic paper:

M. Springmann, D. A. Knopf, and N. Riemer. Detailed Heterogeneous Chemistry in an Urban Plume Box Model: Reversible Co-Adsorption of O_3, NO_2, and H_2O on Soot coated with Benzo[a]pyrene. *Atmospheric Chemistry and Physics Discussions*, 9(2):1005510099, 2009. ISSN 1680-7367. URL http://www.atmos-chem-phys-discuss.net/9/10055/2009/. [1]

In the following, further model results of this study will be presented and discussed.

4.2 Gas-Phase Feedback: NO_x and HONO

In this section, the gas-phase feedback on the NO, NO_2, and HONO concentrations is assessed for the high soot emission scenarios A_{24x}, B_{24x}, and C_{24x}. Since the gas-phase feedback is expected to be greatest for the high emission scenarios, the obtained results represent upper values for the conditions of this modeling study.

4.2.1 NO_x Gas-Phase Feedback

Figure 4.9 shows the temporal evolution of the NO and NO_2 gas concentrations for the high soot emission scenarios and a base scenario with no heterogeneous reactions on soot for the five day simulation period. Both concentrations follow a diurnal cycle, which was described in section 2.1. The heterogeneous reactions and surface replenishments in scenarios A_{24x}, B_{24x}, and C_{24x} lead to increases in the NO and NO_2 gas-phase concentrations. The increases are greatest for scenario B_{24x}, although the most NO_2 is taken up by the soot surface in this scenario.

The NO_2 concentrations in the high-emission scenarios start to differ from the base scenario concentration in the first night of the simulation period. The increase in the NO_2 concentration with respect to the one in the base scenario amounts then to 0.3 ppbv or 43% in scenario B_{24x}, 0.09 ppbv or 13.0% in scenario A_{24x}, and 0.11 ppbv or 16% in scenario C_{24x}, while the difference during daytime is within 10%. This nighttime NO_2 increase is due to the nighttime reaction (2.7) between NO_2 and O_3. Since the gas-phase O_3 concentration is decreased in the high-emission scenarios, as shown in Figure 4.7, the reaction rate of reaction (2.7) is lowered. Thus, less NO_2 is lost by this reaction, which results in relative increases in the NO_2 concentrations in the high-emission scenarios. These increases are nearly compensated during daytime, since the NO_2 chemistry is then dominated by the NO_2 photolysis (2.1), whose rate does not directly depend on the O_3 concentration.

The NO concentration in the high emission scenarios is increased on both the day and the night. On the last day of the simulation period, the increase is 28 pptv or 40.1% in scenario B_{24x}, 21 pptv or 30% in scenario A_{24x}, and 11 pptv or 16% in scenario C_{24x} with respect to the base scenario. During the last night, the increase is 0.3 pptv or 68% in scenario B_{24x}, 0.1 pptv or 28% in scenario A_{24x}, and 0.3 pptv or 58% in scenario C_{24x}. These increases can again be explained by a lowered reaction rate with O_3, in this case of reaction (2.3). In contrast to the NO_2 increases, the NO concentration in the high-emission scenarios is also increased at daytime, since reaction (2.3) can also occur then with a non-negligible rate. An additional NO source, in particular

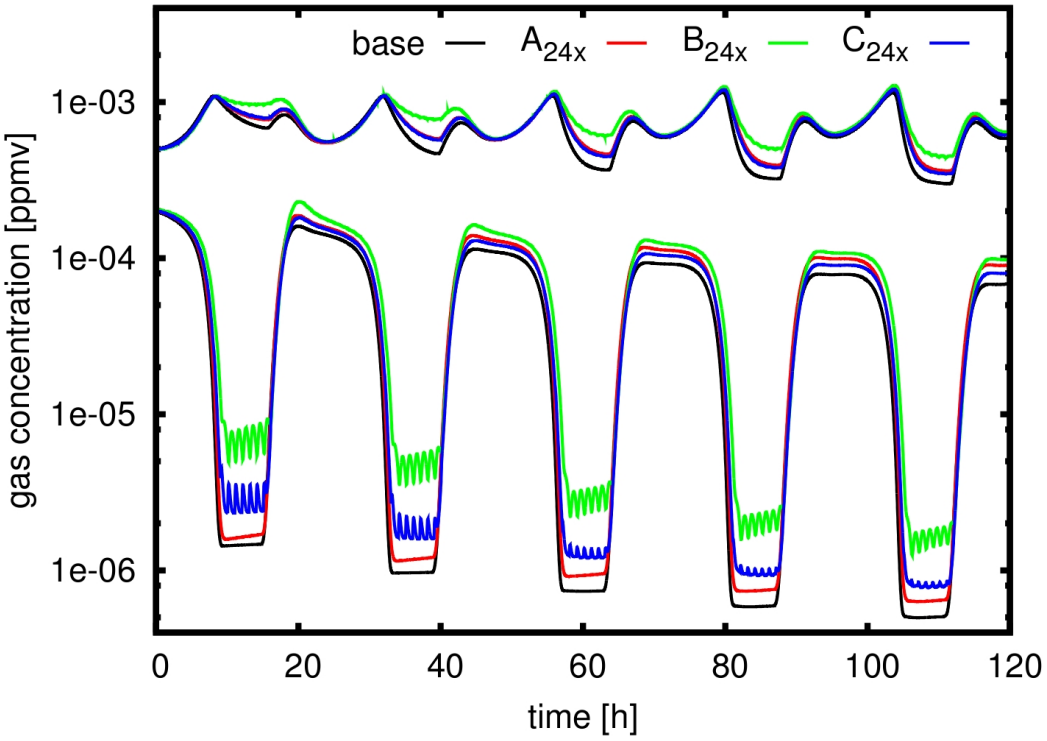

Figure 4.9: Temporal evolution of NO (*lower graphs*) and NO_2 gas-phase concentrations (*upper graphs*) for the high soot emission scenarios A_{24x}, B_{24x}, C_{24x}, and a base scenario with no heterogeneous reactions on soot implemented. Input parameters for the heterogeneous reactions are the same as for scenarios A, B, and C as given in Table 4.1. Exponential smoothing with a smoothing factor of 0.9 was applied to smooth the noise generated from hourly replenishment peaks. The displayed graphs can therefore be regarded as averages.

in the mornings, is the photolysis of NO_2. Since the NO_2 concentration is increased in the high emission scenarios, also the photolysis rate is increased, which leads to higher morning NO concentrations, which can be identified in Figure 4.9, especially for the first three mornings.

NO can also be produced by the photolysis of HONO, which also occurs in the mornings. The temporal evolution of the HONO gas-phase concentration for the high emission scenarios is analyzed next.

4.2.2 HONO Gas-Phase Feedback

In addition to the gas-phase HONO production from the reaction of NO with OH, the heterogeneous reaction scenarios include the surface production and

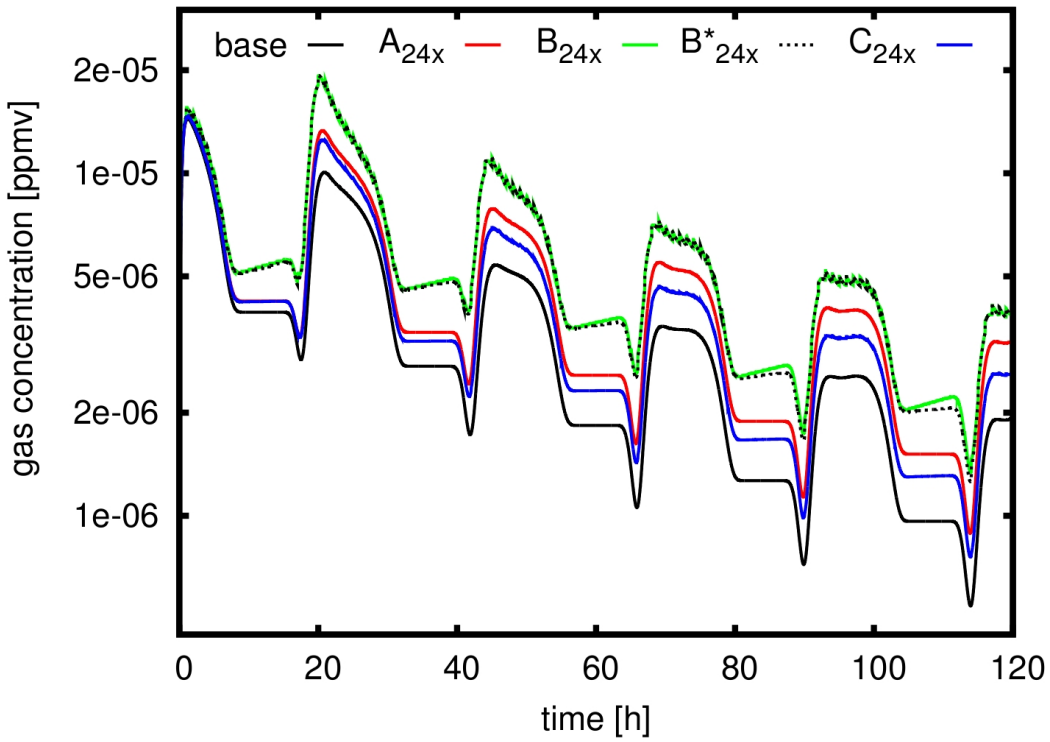

Figure 4.10: Temporal evolution of the HONO gas-phase concentration for the high soot emission scenarios A_{24x}, B_{24x}, B^*_{24x}, C_{24x}, and a base scenario with no heterogeneous reactions on soot implemented. Scenario B^*_{24x} is identical to scenario B_{24x}, but with the HONO desorption from surface reaction SLR5 disabled. Input parameters for the heterogeneous reactios are the same as for scenarios A, B, and C as given in Table 4.1.

subsequent desorption of HONO in surface layer reaction SLR5, as given in Table 4.1. Figure 4.10 shows the temporal evolution of the HONO gas-phase concentration for the high soot emission scenarios A_{24x}, B_{24x}, B^*_{24x}, C_{24x}, and a base scenario with no heterogeneous reactions on soot implemented. Scenario B^*_{24x} is identical to scenario B_{24x}, but with the HONO desorption from surface reaction SLR5 disabled. As can be seen by comparing scenarios B^*_{24x} and B_{24x}, the heterogeneous HONO production does not influence the HONO gas-phase concentration significantly. The maximum difference between the HONO concentrations of both scenarios is 0.15 pptv in the night of the fourth day, which corresponds to an increase in the HONO gas-phase concentration in scenario B_{24x} by 10.6% with respect to scenario B^*_{24x}. During daytime and at the end of the five day simulation period, the difference in HONO

concentrations between scenarios B_{24x} and B^*_{24x} is less than 1%. The heterogeneous HONO production is not significant on the day, because the gas-phase HONO production from NO and OH then exceeds the heterogeneous HONO production by five orders of magnitude, as described in section 4.1.4.

Although not directly, the gas-phase uptake of O_3 and NO_2 influence the HONO gas-phase concentration, as can be seen by comparing scenarios A_{24x}, B_{24x}, and C_{24x} with the base scenario. At the end of the five day modeling period, the HONO gas-phase concentration in scenario B_{24x} shows an increase of 1.9 pptv or 99% with respect to the base scenario, an increase of 1.3 pptv or 67% in scenario A_{24x}, and an increase of 0.7 pptv or 35% in scenario C_{24x}. The reason for these increases are the aforementioned increases in the NO gas-phase concentrations in these scenarios, which result in a faster HONO formation rate from the reaction of NO with OH in the gas phase. The higher HONO concentrations feed also back to higher NO concentrations when HONO photodissociates.

This concludes the evaluation of the gas-phase feedback on the NO_x and HONO concentrations. As shown in this section, the NO, NO_2, and HONO concentrations are significantly increased due to the heterogeneous reactions and surface replenishments in the soot emission scenarios. The next section discusses the potential effects of the chemical aging of soot on the soot surface composition.

4.3 Soot Aging

Soot particles emitted in the urban environment are assumed to be hydrophobic but change their hydrophobic quality due to condensation of ambient gases, coagulation with soluble aerosols, and heterogeneous reactions [61, 165, 166]. The result of the exposure to an oxidizing atmosphere is the transformation of the hydrophobic to a hydrophilic surface, which enables growth by water accretion and the formation of cloud condensation nuclei, thereby influencing the atmospheric radiative budget [167]. In this study, the chemical aging of soot particles due to heterogeneous reactions was studied with respect to changes in the particle surface composition, but changes in the hydrophilicity were not quantified.

The following figures present a sensitivity study on the possible effects of changes in the hydrophilicity, which is modeled by changing the desorption lifetime of the adsorbed water vapor, τ_{d,H_2O}. Changes in τ_{d,H_2O} can be expected to occur with increasing surface oxidation, which was assessed in section 4.1.4 by the BaP half-life. Depending on the scenario, the BaP half-lives ranged from 4 to 32.5 min. For this section's sensitivity study, an arbitrary timescale

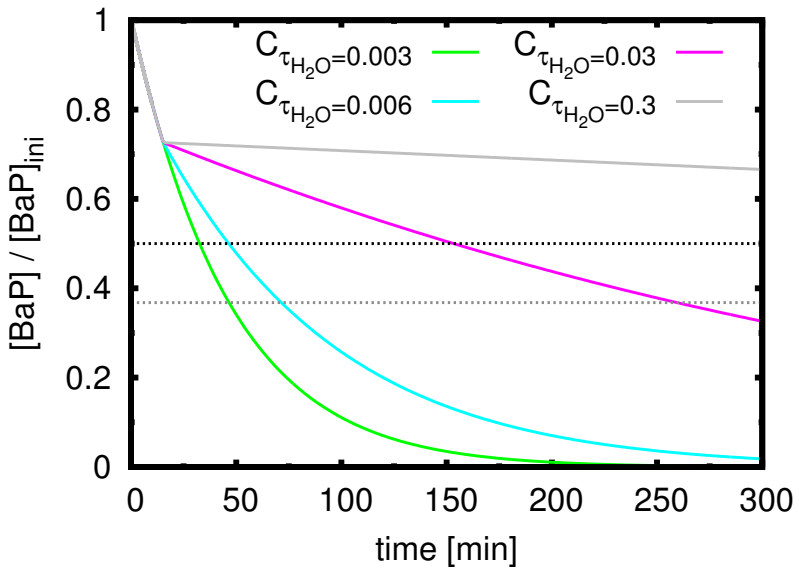

Figure 4.11: Temporal evolution of the ratio of actual BaP surface concentration to initial BaP concentration for scenario C with differing H_2O desorption lifetimes of $\tau_{H_2O} = 0.003$, $\tau_{H_2O} = 0.006$, $\tau_{H_2O} = 0.03$, and $\tau_{H_2O} = 0.3$. Other input parameters for scenario C are given in Table 4.1. The intersection with the horizontal dotted lines indicate the BaP half-life (dotted black line) and the BaP (e-fold) lifetime (dotted grey line).

of 15 min is chosen, after which τ_{d,H_2O} increases 2-fold, 10-fold, or 100-fold. These increases can also be pictured to happen in succession with increasing surface oxidation. Then the BaP half-life can be seen as quantifying the generic oxidation of surface components.

Figure 4.11 shows the temporal evolution of the BaP concentration for scenario C with differing τ_{d,H_2O} after 15 min. The BaP half-lives are highlighted by the intersection with the horizontal dotted black line. Scenario C with an unchanged H_2O desorption time of $\tau_{d,H_2O} = 0.003$ s has a BaP half-life of 32.5 min. When the H_2O desorption lifetime doubles to $\tau_{d,H_2O} = 0.006$ s after 15 min, the BaP half-life increases by 42%; a 10-fold increase to $\tau_{d,H_2O} = 0.03$ s increases the BaP half-life by a factor of 3.7 or 2 h; and a 100-fold increase to $\tau_{d,H_2O} = 0.3$ s increases the BaP half-life by a factor of 37 or 20 h. These increases in the BaP half-life suggest that the surface oxidation is significantly suppressed if the H_2O desorption time increases. A 100-fold increase in τ_{d,H_2O} extends the BaP half-life to timescales that are comparable with timescales of physical aging processes, such as coagulation, which is of the order of 10 to 40 h [166]. When the increase in τ_{d,H_2O} stays below this factor, chemical aging

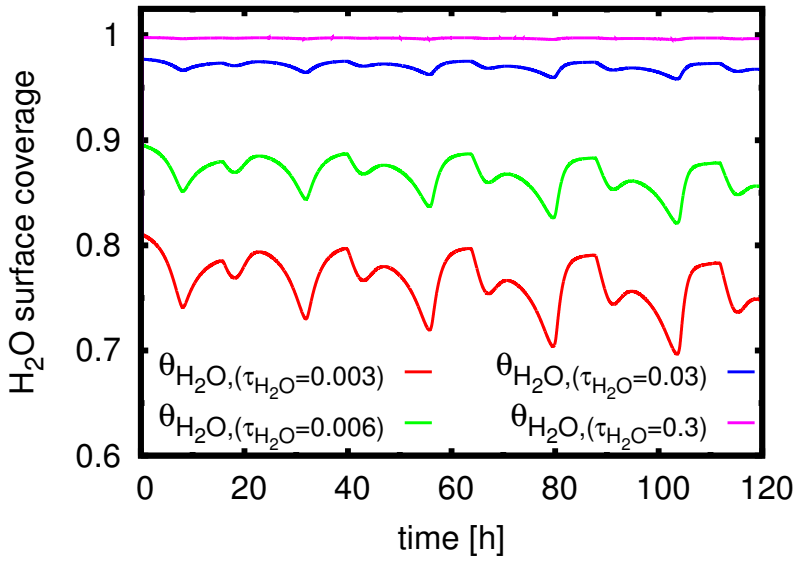

Figure 4.12: Temporal evolution of the H_2O surface coverage θ_{H_2O} in scenario C for differing H_2O desorption lifetimes of $\tau_{H_2O} = 0.003$, $\tau_{H_2O} = 0.006$, $\tau_{H_2O} = 0.03$, and $\tau_{H_2O} = 0.3$. Other input parameters for scenario C are given in Table 4.1.

by heterogeneous reactions occurs on shorter timescales than physical aging processes.

Figure 4.12 shows the temporal evolution of the H_2O surface coverage for scenario C with differing H_2O desorption lifetimes. Increasing the H_2O desorption lifetimes from 0.003 s to 0.006 s, 0.03 s, and 0.3 s, increases the H_2O surface coverage by 14% to 86%, by 29% to 97%, and by 33% to 99.7% respectively. This suggests that when the soot surface becomes more hyrdophilic with a higher H_2O desorption lifetime, the soot particle is almost entirely coated with a layer of water. When adsorption on this water layer is taken into account, it is likely that the sorption layer coverage exceeds one monolayer. Such an increase in sorption layer coverage above one monolayer is characteristic for the transition of hydrophobic to hydrophilic soot [37]. Under these circumstances, even a higher suppression of surface oxidation processes as discussed above can be expected. Then, the influence of the soot particle on the gas-phase depends on the timescale of the aging process and on the efficiency of adsorption on multiple layers of water. Assessing these processes in detail are beyond the scope of this thesis, but should be addressed in future studies.

Chapter 5

Conclusion

The co-adsorption and subsequent surface reactions of O_3, NO_2, and water vapor on soot coated with BaP were modeled for an idealized urban pollution scenario.

The heterogeneous reactions and soot emissions caused significant gas-phase feedbacks. The O_3 gas-phase concentration decreased due to the heterogeneous reactions of O_3, NO_2, water vapor, and high soot emissions by 19 ppbv or 12%, the NO_2 gas-phase concentration increased during nighttime by 0.1 ppbv or 16%, and the NO concentration increased by 11 pptv or 16% during daytime and 0.3 pptv or 58% during nighttime. Especially the absolute magnitude of the O_3 gas-phase feedback suggests that the incorporation of the modeled heterogeneous reactions into air quality models should be considered. Although NO_2 is taken up by soot surfaces during the heterogeneous reactions, the NO_2 gas-phase concentration increased due the gas-phase interdependence of NO_2 and O_3. This shows that the gas-phase feedback is nonlinear for the co-adsorption of interdependent adsorbents. The magnitude of the gas-phase feedbacks was found to be doubled for the co-adsorption of only O_3 and NO_2, which demonstrates the great influence of the co-adsorption of water vapor.

The effect of multiple co-adsorption scenarios on the soot surface chemistry was evaluated. It was shown that the adsorbents' uptake coefficients decrease by 99.9% within the first six hours of simulation time due to surface saturation. Water vapor adsorbs especially rapidly and constantly occupies about 75% of the entire soot surface. This delays surface oxidation, assessed in terms of the half-life of the coating substance BaP, by a factor of up to seven. A linear relationship was found between the BaP half-life and relative humidity (RH). Even increases at low RH levels, from 0% RH to 25% RH, resulted in an increase of the BaP half-life by a factor of three. Higher increases can result from changes in the hydrophilicity of the soot particle, which is expected to occur with increasing surface oxidation. These results suggest that the soot

particle is "deactivated" mainly by the adsorption of water vapor, which can be enhanced by surface oxidation by O_3 and NO_2.

This study coupled for the first time the detailed uptake parametrization of the PRA framework for aerosol chemistry and gas-particle interactions [12] to a dynamic gas-phase model which simulates diurnal changes in the gas-phase composition. The gas-phase coupling of the PRA framework made possible the observation of the nonlinear gas-phase feedbacks, while the implementation of the detailed PRA framework — as opposed to a parametrization of heterogeneous reactions with constant uptake coefficients — into the gas-phase model made possible the observation of the soot deactivation by dynamic decreases in the uptake coefficients. Thus, the detailed parametrization of the uptake process in atmospheric models is necessary to realistically assess the influence of heterogeneous reactions on the gas-phase and surface composition.

Future modeling studies are suggested to investigate the difference between chemical aging by heterogeneous reactions and physical aging by, e.g., coagulation. Laboratory studies on the temporal evolution of the residence time of H_2O on the soot surface would provide the necessary data to model the potential cloud formation of soot particles. More laboratory studies which measure the physiochemical parameters needed for a detailed modeling of the uptake processes are encouraged. These physiochemical parameters are the time-specific accommodation coefficient, the effective molecular cross-section, and the desorption lifetime of each adsorbent. With that information, more modeling studies can be carried out to elucidate the magnitude of gas-phase uptake of other adsorbents and to determine a minimum set of adsorbents that are needed to represent the main effects that heterogeneous reactions have on the gas-phase and surface composition.

Bibliography

[1] M. Springmann, D. A. Knopf, and N. Riemer. Detailed heterogeneous chemistry in an urban plume box model: Reversible co-adsorption of o_3, no_2, and h_2o on soot coated with benzo[a]pyrene. *Atmospheric Chemistry and Physics Discussions*, 9(2):10055–10099, 2009. ISSN 1680-7367. URL `http://www.atmos-chem-phys-discuss.net/9/10055/2009/`.

[2] B. J. Finlayson-Pitts and J. N. Pitts. *Chemistry of the Upper and Lower Atmosphere*. Academic Press, San Diego, 2000.

[3] P. Brimblecombe. Interest in air-pollution among early fellows of royal society. *Notes Rec. R. Soc. Lond.*, 32(2):123–129, 1978. ISSN 0035-9149.

[4] H. Özkaynak and G. D. Thurston. Associations between 1980 united-states mortality-rates and alternative measures of airborne particle concentration. *Risk Anal.*, 7(4):449–461, Dec 1987. ISSN 0272-4332.

[5] C. Arden Pope, III, Majid Ezzati, and Douglas W. Dockery. Fine-Particulate Air Pollution and Life Expectancy in the United States. *N. Engl. J. Med.*, 360(4):376–386, Jan 22 2009. ISSN 0028-4793.

[6] V. Ramanathan and G. Carmichael. Global and regional climate changes due to black carbon. *Nat. Geosci.*, 1(4):221–227, Apr 2008. ISSN 1752-0894. doi: {10.1038/ngeo156}.

[7] M. Z. Jacobson. Strong radiative heating due to the mixing state of black carbon in atmospheric aerosols. *Nature*, 409(6821):695–697, Feb 8 2001. ISSN 0028-0836.

[8] P. J. Crutzen and F. Arnold. Nitric-acid cloud formation in the cold antarctic stratosphere - a major cause for the springtime ozone hole. *Nature*, 324(6098):651–655, Dec 18 1986. ISSN 0028-0836.

[9] S. Solomon, R. R. Garcia, F. S. Rowland, and D. J. Wuebbles. On the depletion of Antarctic ozone. *Nature*, 321(6072):755–758, Jun 19 1986. ISSN 0028-0836.

[10] M. J. Molina, T. L. Tso, L. T. Molina, and F. C. Y. Wang. Antarctic Stratospheric Chemistry of Chlorine Nitrate, Hydrogen Chloride and Ice - Release of Active Chlorine. *Science*, 238(4831):1253–1257, Nov 27 1987. ISSN 0036-8075.

[11] S. Solomon, M. Mills, L. E. Heidt, W. H. Pollock, and A. F. Tuck. On the evaluation of ozone depletion potentials. *J. Geophys. Res-Atmos.*, 97(D1):825–842, Jan 20 1992. ISSN 0148-0227.

[12] U. Pöschl, Y. Rudich, and M. Ammann. Kinetic model framework for aerosol and cloud surface chemistry and gas-particle interactions - Part 1: General equations, parameters, and terminology. *Atmos. Chem. Phys.*, 7(23):5989–6023, 2007. ISSN 1680-7316.

[13] W. R. Stockwell, P. Middleton, J. S. Chang, and X. Y. Tang. The 2nd generation regional acid deposition model chemical mechanism for regional air-quality modeling. *J. Geophys. Res-Atmos.*, 95(D10):16343–16367, Sep 20 1990. ISSN 0148-0227.

[14] X. Tie, G. Brasseur, L. Emmons, L. Horowitz, and D. Kinnison. Effects of aerosols on tropospheric oxidants: A global model study. *J. Geophys. Res-Atmos.*, 106(D19):22931–22964, Oct 16 2001. ISSN 0747-7309.

[15] I. Bey, D. J. Jacob, R. M. Yantosca, J. A. Logan, B. D. Field, A. M. Fiore, Q. B. Li, H. G. Y. Liu, L. J. Mickley, and M. G. Schultz. Global modeling of tropospheric chemistry with assimilated meteorology: Model description and evaluation. *J. Geophys. Res-Atmos.*, 106(D19):23073–23095, Oct 16 2001. ISSN 0747-7309.

[16] J. H. Seinfeld and S. Pandis. *Atmospheric Chemistry and Physics: From Air Pollution to Climate Change*. Wiley-Interscience, New York, 2006.

[17] F. E. Blacet. Photochemistry in the lower atmosphere. *Industrial and Engineering Chemistry*, 44(6):1339–1342, 1952. ISSN 0019-7866.

[18] M. Lenner. Nitrogen-dioxide in exhaust emissions from motor-vehicles. *Atmos. Environ.*, 21(1):37–43, 1987. ISSN 1352-2310.

[19] F. W. Lurmann, H. H. Main, K. T. Knapp, L. Stockburger, R. A. Rasmussen, and K. Fung. *Analysis of the ambient VOC data collected in the Southern California Air Quality Study*. Final Report to the California Air Resources Board under Contract A832-130, 1992.

[20] Carter W. P. L. *Development of ozone reactivity scales for volatile organic compounds*. U.S. Environmental Protection Agency, U. S. Environmental Protection Agency, Research Triangle Park, NC, epa-600/3-91-050 edition, 1991.

[21] H. Saathoff, K. H. Naumann, N. Riemer, S. Kamm, O. Mohler, U. Schurath, H. Vogel, and B. Vogel. The loss of NO_2, HNO_3, NO_3/N_2O_5, and $HO_2/HOONO_2$ on soot aerosol: A chamber and modeling study. *Geophys. Res. Lett.*, 28(10):1957–1960, May 15 2001. ISSN 0094-8276.

[22] JS Lighty, JM Veranth, and AF Sarofim. Combustion aerosols: Factors governing their size and composition and implications to human health. *J. Air Waste Manage. Assoc.*, 50(9):1565–1618, Sep 2000. ISSN 1047-3289.

[23] K. T. Whitby and G. M. Sverdrup. California Aerosols: Their Physical and Chemical Characteristics. *Adv. Environ. Sci. Technol.*, 8:477–525, 1980.

[24] M. Z. Jacobson. *Atmospheric Pollution - History, Science, and Regulation*. Cambridge University Press, Cambridge, 2002.

[25] Todd L. Watterson, Jared Sorensen, Randy Martin, and Roger A. Coulombe, Jr. Effects of PM2.5 collected from Cache Valley Utah on genes associated with the inflammatory response in human lung cells. *J. Toxicol. Env. Health Part A*, 70(20):1731–1744, 2007. ISSN 1528-7394. doi: {10.1080/15287390701457746}.

[26] H. Yu, Y. J. Kaufman, M. Chin, G. Feingold, L. A. Remer, T. L. Anderson, Y. Balkanski, N. Bellouin, O. Boucher, S. Christopher, P. DeCola, R. Kahn, D. Koch, N. Loeb, M. S. Reddy, M. Schulz, T. Takemura, and M. Zhou. A review of measurement-based assessments of the aerosol direct radiative effect and forcing. *Atmos. Chem. Phys.*, 6:613–666, Feb 27 2006. ISSN 1680-7316.

[27] F Raes, R Van Dingenen, E Vignati, J Wilson, JP Putaud, JH Seinfeld, and P Adams. Formation and cycling of aerosols in the global troposphere. *Atmos. Environ.*, 34(25):4215–4240, 2000. ISSN 1352-2310.

[28] J. Williams, M. de Reus, R. Krejci, H. Fischer, and J. Strom. Application of the variability-size relationship to atmospheric aerosol studies: estimating aerosol lifetimes and ages. *Atmos. Chem. Phys.*, 2:133–145, Jun 12 2002. ISSN 1680-7324.

[29] U Pöschl. Atmospheric aerosols: Composition, transformation, climate and health effects. *Angew. Chem., Int. Ed*, 44(46):7520–7540, 2005. ISSN 1433-7851. doi: 10.1002/anie.200501122.

[30] G. T. Wolff and P. E. Korsog. Estimates of the contributions of sources to inhalable particulate concentrations in detroit. *Atmos. Environ.*, 19 (9):1399–1409, 1985. ISSN 1352-2310.

[31] R. S. Hamilton and T. A. Mansfield. Airborne particulate elemental carbon - its sources, transport and contribution to dark smoke and soiling. *Atmos. Environ. A-Gen.*, 25(3-4):715–723, 1991. ISSN 0004-6981.

[32] T. V. Nunes and C. A. Pio. carbonaceous aerosols in industrial and coastal atmospheres. *Atmos. Environ. A-Gen.*, 27(8):1339–1346, Jun 1993. ISSN 0004-6981.

[33] F. Arens, L. Gutzwiller, U. Baltensperger, H.W. Gaggeler, and M. Ammann. Heterogeneous reaction of NO_2 on diesel soot particles. *Environ. Sci. Technol.*, 35(11):2191–2199, Jun 1 2001. ISSN 0013-936X.

[34] A. M. Nienow and J. T. Roberts. Heterogeneous chemistry of carbon aerosols. *Annu. Rev. Phys. Chem.*, 57:105–128, 2006. ISSN 0066-426X. doi: 10.1146/annurev.physchem.57.032905.104525.

[35] C. Van Gulijk, J. C. M. Marijnissen, M. Makkee, J. A. Moulijn, and A. Schmidt-Ott. Measuring diesel soot with a scanning mobility particle sizer and an electrical low-pressure impactor: performance assessment with a model for fractal-like agglomerates. *J. Aerosol. Sci.*, 35(5):633–655, May 2004. ISSN 0021-8502. doi: 10.1016/j.jaerosci.2003.11.004.

[36] S. Brunauer, P. H. Emmett, and E. Teller. Adsorption of gases in multimolecular layers. *J. Am. Chem. Soc.*, 60:309–319, Jan-Jun 1938. ISSN 0002-7863.

[37] O. B. Popovicheva, N. M. Persiantseva, V. Tishkova, N. K. Shonija, and N. A. Zubareva. Quantification of water uptake by soot particles. *Environ. Res. Lett.*, 3(2), Apr-Jun 2008. ISSN 1748-9326. doi: 10.1088/1748-9326/3/2/025009.

[38] M. Dymarska, B. J. Murray, L. M. Sun, M. L. Eastwood, D. A. Knopf, and A.K. Bertram. Deposition ice nucleation on soot at temperatures relevant for the lower troposphere. *J. Geophys. Res-Atmos.*, 111(D4), Feb 25 2006. ISSN 0148-0227. doi: 10.1029/2005JD006627.

[39] H. Burtscher, A. Leonardi, D. Steiner, U. Baltensperger, and A. Weber. Aging of combustion particles in the atmosphere - results from a field-study in zurich. *Water Air Soil Pollut.*, 68(1-2):137–147, May 1993. ISSN 0049-6979.

[40] D. Steiner, H. Burtscher, and H. Gross. Structure and disposition of particles from a spark-ignition engine. *Atmos. Environ. A-Gen.*, 26(6): 997–1003, Apr 1992. ISSN 0004-6981.

[41] D. S. Covert and J. Heintzenberg. Measurement of the degree of internal external mixing of hygroscopic compounds and soot in atmospheric aerosols. *Sci. Total Environ.*, 36(Jun):347–352, 1984. ISSN 0048-9697.

[42] E. Andrews and S. M. Larson. Effect of surfactant layers on the size changes of aerosol-particles as a function of relative-humidity. *Environ. Sci. Technol.*, 27(5):857–865, May 1993. ISSN 0013-936X.

[43] J. W. Cook, C. L. Hewett, and I. Hieger. The isolation of a cancer-producing hydrocarbon from coal tar. parts i, ii, and iii. *J. Chem. Soc.*, pages 395–405, 1933.

[44] J. Leitner, M. B. Shimkin, and M. J. Shear. Production of subcutaneous sarcomas in mice with tars extracted from atmospheric dusts. *J. Nathl. Cancer inst.*, pages 155–165, 1942.

[45] J. Leitner and M. J. Shear. Quantitative experiments on the production of subcutaneous tumors in strain A. Mice with marginal doses of 3,4-Benzpyrene. *J. Nathl. Cancer inst.*, pages 455–477, 1943.

[46] R. E. Waller. The benzopyrene content of town air. *Br. J. Cancer*, pages 8–21, 1952.

[47] P. Kotin, H. L. Falk, and M. Thomas. The production of skin tumors in mice with oxidation products of aliphatic hydrocarbons. *Cancer*, pages 905–909, 1956.

[48] International Ageency for Research on Cancer (IARC). Evaluation of Carcinogenic Risk of Chemicals to Humans. *Polynuclear Aromatic Compounds, Part 1*, 32, 1984.

[49] United States EPA. *Provisional Guidance for Quantitative Risk Assessment of Polycyclic Aromatic Hydrocarbons*. Office of Research and Development, Washington, DC, epa 600/r-93-089 edition, 1993.

[50] J. O. Allen, N. M. Dookeran, K. Taghizadeh, A. L. Lafleur, K. A. Smith, and A. F. Sarofim. Measurement of oxygenated polycyclic aromatic hydrocarbons with a size-segregated urban aerosol. *Environ. Sci. Technol.*, 31:2064–2070, 1997.

[51] S. O. Baek, Goldstone M. E., P. W. W. Kirk, J. N. Lester, and R. Perry. Concentrations of particulate and gaseous polycyclic aromatic hydrocarbons in London air following a reduction in the lead content of petrol in the United Kingdom. *Sci. Total Environ.*, 111:169–199, 1992.

[52] T. D Behymer and R. A. Hites. Photolysis of polycyclic aromatic-hydrocarbons adsorbed on simulated atmospheric particulates. *Environ. Sci. Technol.*, 19(10):1004–1006, 1985. ISSN 0013-936X.

[53] R. Dabestani. Photophysical and photochemical behavior of poly- cyclic aromatic hydrocarbons on silica surfaces. *Inter-Am. Photochem. Soc. Newsl.*, 20:24–36, 1997.

[54] M. E. Sigman, R. Arce, C. Rayes, J. T. Barbas, and R. Dabestani. Environmental organic photochemistry: Pah photolysis at solid-air interfaces. *Div. Environ. Chem., Prepr. Ext. Abstr.*, 37:313–315, 1997.

[55] W. A. Korfmacher, E. L. Wehry, G. Mamantov, and D. F. S. Natusch. Resistance to photochemical decomposition of polycyclic aromatic-hydrocarbons vapor-adsorbed on coal fly-ash. *Environ. Sci. Technol.*, 14(9):1094–1099, 1980. ISSN 0013-936X.

[56] T. D. Behymer and R. A. Hites. Photolysis of polycyclic aromatic-hydrocarbons adsorbed on fly-ash. *Environ. Sci. Technol.*, 22(11):1311–1319, Nov 1988. ISSN 0013-936X.

[57] J. N. Pitts, K. A. Vancauwenberghe, D. Grosjean, J. P. Schmid, D. R. Fitz, W. L. Belser, G. B. Knudson, and P. M. Hynds. Atmospheric reactions of polycyclic aromatic-hydrocarbons - facile formation of mutagenic nitro-derivatives. *Science*, 202(4367):515–519, 1978. ISSN 0036-8075.

[58] S. E. Ottinger, K. Mayura, S. L. Lemke, K. S. McKenzie, N. Y. Wang, L. F. Kubena, and T. D. Phillips. Utilization of electrochemically generated ozone in the degradation and detoxication of benzo[a]pyrene. *J. Toxicol. Env. Health Pt A*, 57(8):565–583, Aug 27 1999. ISSN 0098-4108.

[59] T. Letzel, E. Rosenberg, R. Wissiack, M. Grasserbauer, and R. Niessner. Separation and identification of polar degradation products of

benzo[a]pyrene with ozone by atmospheric pressure chemical ionization-mass spectrometry after optimized column chromatographic clean-up. *J. Chromatogr., A*, 855(2):501–514, Sep 10 1999. ISSN 0021-9673.

[60] U. Pöschl, T. Letzel, C. Schauer, and R. Niessner. Interaction of ozone and water vapor with spark discharge soot aerosol particles coated with benzo[a]pyrene: O_3 and H_2O adsorption, benzo[a]pyrene degradation, and atmospheric implications. *J. Phys. Chem. A*, 105(16):4029–4041, Apr 26 2001. ISSN 1089-5639.

[61] Y. Rudich, N. M. Donahue, and T. F. Mentel. Aging of organic aerosol: Bridging the gap between laboratory and field studies. *Annu. Rev. Phys. Chem.*, 58:321–352, 2007. ISSN 0066-426X. doi: 10.1146/annurev.physchem.58.032806.104432.

[62] D. M. Smith and A. R. Chughtai. Reaction kinetics of ozone at low concentrations with n-hexane soot. *J. Geophys. Res-Atmos.*, 101(D14):19607–19620, Aug 27 1996. ISSN 0148-0227.

[63] R. S. Disselkamp, M. A. Carpenter, J. P. Cowin, C. M. Berkowitz, E. G. Chapman, R. A. Zaveri, and N. S. Laulainen. Ozone loss in soot aerosols. *J. Geophys. Res-Atmos.*, 105(D8):9767–9771, Apr 27 2000. ISSN 0747-7309.

[64] S. Lelievre, Y. Bedjanian, N. Pouvesle, J. L. Delfau, C. Vovelle, and G. LeBras. Heterogeneous reaction of ozone with hydrocarbon flame soot. *Phys. Chem. Chem. Phys.*, 6(6):1181–1191, Mar 21 2004. ISSN 1463-9076. doi: {10.1039/b316895f}.

[65] S. Stephens, M. J. Rossi, and D. M. Golden. The heterogeneous reaction of ozone on carbonaceous surfaces. *Int. J. Chem. Kinet.*, 18(10):1133–1149, Oct 1986. ISSN 0538-8066.

[66] E. R. Thomas, G. J. Frost, and Y. Rudich. Reactive uptake of ozone by proxies for organic aerosols: Surface-bound and gas-phase products. *J. Geophys. Res-Atmos.*, 106(D3):3045–3056, Feb 16 2001. ISSN 0747-7309.

[67] C. A. Rogaski, D. M. Golden, and L. R. Williams. Reactive uptake and hydration experiments on amorphous carbon treated with NO_2, SO_2, O_3, HNO_3, and H_2SO_4. *Geophys. Res. Lett.*, 24(4):381–384, Feb 15 1997. ISSN 0094-8276.

[68] M. Ammann, M. Kalberer, D. T. Jost, L. Tobler, E. Rossler, D. Piguet, H.W. Gaggeler, and U. Baltensperger. Heterogeneous production of nitrous acid on soot in polluted air masses. *Nature*, 395(6698):157–160, Sep 10 1998. ISSN 0028-0836.

[69] J. Kleffmann, K. H. Becker, M. Lackhoff, and P. Wiesen. Heterogeneous conversion of NO_2 on carbonaceous surfaces. *Phys. Chem. Chem. Phys.*, 1(24):5443–5450, Dec 15 1999. ISSN 1463-9076.

[70] U. Kirchner, V. Scheer, and R. Vogt. FTIR spectroscopic investigation of the mechanism and kinetics of the heterogeneous reactions of NO_2 and HNO_3 with soot. *J. Phys. Chem. A*, 104(39):8908–8915, Oct 5 2000. ISSN 1089-5639.

[71] A. Gerecke, A. Thielmann, L. Gutzwiller, and M. J. Rossi. The chemical kinetics of HONO formation resulting from heterogeneous interaction of NO_2 with flame soot. *Geophys. Res. Lett.*, 25(13):2453–2456, Jul 1 1998. ISSN 0094-8276.

[72] D. G. Aubin and J. P. D. Abbatt. Interaction of NO_2 with hydrocarbon soot: Focus on HONO yield, surface modification, and mechanism. *J. Phys. Chem. A*, 111(28):6263–6273, Jul 19 2007. ISSN 1089-5639. doi: 10.1021/jp068884h.

[73] J. Jäger and V. Hanüs. Reaction of solid carrier-adsorbed polycyclic aromatic-hydrocarbons with gaseous low-concentrated nitrogen-dioxide. *J. Hyg. Epidemiol. Microbiol. Immunol.*, 24(1):1–15, 1980. ISSN 0022-1732.

[74] E. Weingartner, H. Burtscher, and U. Baltensperger. Hygroscopic properties of carbon and diesel soot particles. *Atmos. Environ.*, 31(15):2311–2327, Aug 1997. ISSN 1352-2310.

[75] A. R. Chughtai, N. J. Miller, D. M. Smith, and J. R. Pitts. Carbonaceous particle hydration III. *J. Atmos. Chem.*, 34(2):259–279, Oct 1999. ISSN 0167-7764.

[76] A. R. Chughtai, G. R. Williams, M. M. O. Atteya, N. J. Miller, and D. M. Smith. Carbonaceous particle hydration. *Atmos. Environ.*, 33 (17):2679–2687, Aug 1999. ISSN 1352-2310.

[77] Y. Bedjanian, S. Lelievre, and G. Le Bras. Experimental study of the interaction of HO_2 radicals with soot surface. *Phys. Chem. Chem. Phys.*, 7(2):334–341, 2005. ISSN 1463-9076. doi: {10.1039/b414217a}.

[78] Simone Gross and Allan K. Bertram. Reactive uptake of NO3, N2O5, NO2, HNO3, and O-3 on three types of polycyclic aromatic hydrocarbon surfaces. *J. Phys. Chem. A*, 112(14):3104–3113, Apr 10 2008. ISSN 1089-5639. doi: {10.1021/jp7107544}.

[79] J. Troe. Specific rate constants k(E,J) for unimolecular bond fissions. *J. Chem. Phys.*, 79(12):6017–6029, 1983. ISSN 0021-9606.

[80] P. V. Danckwerts. Absorption by simultaneous diffusion and chemical reaction into particles of various shapes and into falling drops. *T. Faraday. Soc.*, 47(9):1014–1023, 1951.

[81] S. E. Schwartz and J. E. Freiberg. Mass-transport limitation to the rate of reaction of gases in liquid droplets - Application to oxidation of SO_2 in aqueous-solutions. *Atmos. Env.*, 15(7):1129–1144, 1981. ISSN 1352-2310.

[82] S. E. Schwartz. *NATO ASI Series*, volume G6, chapter Chemistry of Multiphase Atmospheric Systems, page 415. Springer, Berlin, 1986.

[83] N. A. Fuchs, A. G. Sutugin, and E. I. Komtsev. Formation of highly dispersed, uncoagulated condensation aerosols. *Colloid J. Russ. Acad+*, 33(4):485–&, 1971.

[84] M. Ammann, U. Pöschl, and Y. Rudich. Effects of reversible adsorption and Langmuir-Hinshelwood surface reactions on gas uptake by atmospheric particles. *Phys. Chem. Chem. Phys.*, 5(2):351–356, 2003. ISSN 1463-9076. doi: {10.1039/b208708a}.

[85] J. T. Jayne, J. A. Gardner, P. Davidovits, D. R. Worsnop, M. S. Zahniser, and C. E. Kolb. The effect of h2o2 content on the uptake of so2(g) by aqueous droplets. *J. Geophys. Res.-Atmos.*, 95(D12):20559–20563, Nov 20 1990. ISSN 0148-0227.

[86] L. T. Chu, M. T. Leu, and L. F. Keyser. Heterogeneous reactions of hocl+hcl-]cl2+h2o and clono2+hcl-]cl2+hno3 on ice surfaces at polar stratospheric conditions. *J. Phys. Chem.*, 97(49):12798–12804, Dec 9 1993. ISSN 0022-3654.

[87] Z. Krivacsy, A. Gelencser, G. Kiss, E. Meszaros, A. Molnar, A. Hoffer, T. Meszaros, Z. Sarvari, D. Temesi, B. Varga, U. Baltensperger, S. Nyeki, and E. Weingartner. Study on the chemical character of water soluble organic compounds in fine atmospheric aerosol at the Jungfraujoch. *J. Atmos. Chem.*, 39(3):235–259, 2001. ISSN 0167-7764.

[88] S. M. Clegg and J. P. D. Abbatt. Oxidation of SO_2 by H_2O_2 on ice surfaces at 228 K: a sink for SO_2 in ice clouds. *Atmos. Chem. Phys.*, 1: 73–78, Nov 22 2001. ISSN 1680-7324.

[89] H. Z. Zhang, Y. Q. Li, P. Davidovits, L. R. Williams, J. T. Jayne, C. E. Kolb, and D. R. Worsnop. Uptake of gas-phase species by 1-octanol. 2. Uptake of hydrogen halides and acetic acid as a function of relative humidity and temperature. *J. Phys. Chem. A*, 107(33):6398–6407, Aug 21 2003. ISSN 1089-5639. doi: {10.1021/jp034254t}.

[90] Y. Rudich. Laboratory perspectives on the chemical transformations of organic matter in atmospheric particles. *Chem. Rev.*, 103(12):5097–5124, Dec 2003. ISSN 0009-2665. doi: 10.1021/cr020508f.

[91] S. A. Teukolsky W. H. Press, B. P. Flannery and W. T. Vetterling. *Numerical Recipes in FORTRAN: The Art of Scientific Computing*. Cambridge University Press, Cambridge, England, 2nd edition, 1992.

[92] C. W. Gear. Automatic integration of ordinary differential equations. *Commun. ACM*, 14(3):176–&, 1971. ISSN 0001-0782.

[93] J. S. Chang, R. A. Brost, I. S. A. Isaksen, S. Madronich, P. Middleton, W. R. Stockwell, and C. J. Walcek. A Three-Dimensional Eulerian Acid Deposition Model - Physical Concepts and Formulation. *J. Geophys. Res.-Atmos.*, 92(D12):14681–14700, Dec 20 1987.

[94] J. G. Calvert and S. Madronich. Theoretical-study of the initial products of the atmospheric oxidation of hydrocarbons. *J. Geophys. Res.-Atmos.*, 92(D2):2211–2220, Feb 20 1987.

[95] M. E. Jenkin, S. M. Saunders, and M. J. Pilling. The tropospheric degradation of volatile organic compounds: A protocol for mechanism development. *Atmos. Environ.*, 31(1):81–104, Jan 1997. ISSN 1352-2310.

[96] SW Wang, PG Georgopoulos, G Li, and H Rabitz. Condensing complex atmospheric chemistry mechanisms. 1. The direct constrained approximate lumping (DCAL) method applied to alkane photochemistry. *Environ. Sci. Technol.*, 32(13):2018–2024, Jul 1 1998. ISSN 0013-936X.

[97] F. W. Lurmann, A. C. Lloyd, and R. Atkinson. A chemical mechanism for use in long-range transport acid deposition computer modeling. *J. Geophys. Res.-Atmos.*, 91(D10):905–936, Sep 20 1986.

[98] M. W. Gery, G. Z. Whitten, J. P. Killus, and M. C. Dodge. A photochemical kinetics mechanism for urban and regional scale computer modeling. *J. Geophys. Res.-Atmos.*, 94(D10):12925–12956, Sep 20 1989.

[99] J. Olson, M. Prather, T. Berntsen, G. Carmichael, R. Chatfield, P. Connell, R. Derwent, L. Horowitz, S. X. Jin, M. Kanakidou, P. Kasibhatla, R. Kotamarthi, M. Kuhn, K. Law, J. Penner, L. Perliski, S. Sillman, F. Stordal, A. Thompson, and O. Wild. Results from the Intergovernmental Panel on Climatic Change Photochemical Model Intercomparison (PhotoComp). *J. Geophys. Res.-Atmos.*, 102(D5):5979–5991, Mar 20 1997.

[100] M. Kuhn, P. J. H. Builtjes, D. Poppe, D. Simpson, W. R. Stockwell, Y. Andersson-Skold, A. Baart, M. Das, F. Fiedler, O. Hov, F. Kirchner, P. A. Makar, J. B. Milford, M. G. M. Roemer, R. Ruhnke, A. Strand, B. Vogel, and H. Vogel. Intercomparison of the gas-phase chemistry in several chemistry and transport models. *Atmos. Environ.*, 32(4):693–709, Feb 1998. ISSN 1352-2310.

[101] X. Tie, L. Emmons, L. Horowitz, G. Brasseur, B. Ridley, E. Atlas, C. Stround, P. Hess, A. Klonecki, S. Madronich, R. Talbot, and J. Dibb. Effect of sulfate aerosol on tropospheric NOx and ozone budgets: Model simulations and TOPSE evidence. *J. Geophys. Res.-Atmos.*, 108(D4), Feb 13 2003. ISSN 0747-7309. doi: {10.1029/2001JD001508}.

[102] J. S. Gaffney, N. A. Marley, M. M. Cunningham, and P. V. Doskey. Measurements of peroxyacyl nitrates (PANS) in Mexico City: implications for megacity air quality impacts on regional scales. *Atmos. Environ.*, 33 (30):5003–5012, Dec 1999. ISSN 1352-2310.

[103] K. Toyota, Y. Kanaya, M. Takahashi, and H. Akimoto. A box model study on photochemical interactions between VOCs and reactive halogen species in the marine boundary layer. *Atmos. Chem. Phys.*, 4:1961–1987, Sep 30 2004. ISSN 1680-7324.

[104] M. C. Dodge. Combined effects of organic-reactivity and nmhc NOx ratio on photochemical oxidant formation - a modeling study. *Atmos. Environ.*, 18(8):1657–1665, 1984. ISSN 1352-2310.

[105] S. Sillman, J. A. Logan, and S. C. Wofsy. A regional scale-model for ozone in the united-states with subgrid representation of urban and power-plant plumes. *J. Geophys. Res.-Atmos.*, 95(D5):5731–5748, Apr 20 1990. ISSN 0148-0227.

[106] D. W. Dockery and C. A. Pope. Acute respiratory effects of particulate air-pollution. *Annu. Rev. Public Health*, 15:107–132, 1994. ISSN 0163-7525.

[107] C. Pilinis and J. H. Seinfeld. Continued development of a general equilibrium-model for inorganic multicomponent atmospheric aerosols. *Atmos. Environ.*, 21(11):2453–2466, 1987. ISSN 1352-2310.

[108] F. W. Lurmann, A. S. Wexler, S. N. Pandis, S. Musarra, N. Kumar, and J. H. Seinfeld. Modelling urban and regional aerosols - II. Application to California's South Coast Air Basin. *Atmos. Environ.*, 31(17):2695–2715, Sep 1997. ISSN 1352-2310.

[109] Z. Y. Meng, D. Dabdub, and J. H. Seinfeld. Size-resolved and chemically resolved model of atmospheric aerosol dynamics. *J. Geophys. Res.-Atmos.*, 103(D3):3419–3435, Feb 20 1998. ISSN 0747-7309.

[110] B. Aumont, S. Madronich, M. Ammann, M. Kalberer, U. Baltensperger, D. Hauglustaine, and F. Brocheton. On the NO_2 plus soot reaction in the atmosphere. *J. Geophys. Res.-Atmos.*, 104(D1):1729–1736, Jan 20 1999. ISSN 0747-7309.

[111] T. Staffelbach, A. Neftel, and L. W. Horowitz. Photochemical oxidant formation over southern Switzerland - 2. Model results. *J. Geophys. Res.-Atmos.*, 102(D19):23363–23373, Oct 20 1997.

[112] VR Kotamarthi, JS Gaffney, NA Marley, and PV Doskey. Heterogeneous NOx chemistry in the polluted PBL. *Atmos. Environ.*, 35(26):4489–4498, Sep 2001. ISSN 1352-2310.

[113] S. Lelievre, Y. Bedjanian, G. Laverdet, and G. LeBras. Heterogeneous reaction of NO_2 with hydrocarbon flame soot. *J. Phys. Chem. A*, 108(49): 10807–10817, Dec 9 2004. ISSN 1089-5639. doi: {10.1021/jp0469970}.

[114] B. Vogel, H. Vogel, J. Kleffmann, and R. Kurtenbach. Measured and simulated vertical profiles of nitrous acid - Part II. Model simulations and indications for a photolytic source. *Atmos. Environ.*, 37(21):2957–2966, Jul 2003. ISSN 1352-2310. doi: {10.1016/S1352-2310(03)00243-7}.

[115] Y. A. Aklilu and D. V. Michelangeli. Box model investigation of the effect of soot particles on ozone downwind from an urban area through heterogeneous reactions. *Environ. Sci. Technol.*, 38(21):5540–5547, Nov 1 2004. ISSN 0013-936X. doi: 10.1021/es035079x.

[116] M. Ammann, E. Rossler, U. Baltensperger, and Kalberer M. Heterogeneous reaction of NO_2 on bulk soot samples. *Laboratory of Radio- and Environmental Chemistry Annual Report 1997*, 24, 1997.

[117] M. Ammann and U. Pöschl. Kinetic model framework for aerosol and cloud surface chemistry and gas-particle interactions - Part 2: Exemplary practical applications and numerical simulations. *Atmos. Chem. Phys.* , 7(23):6025–6045, 2007. ISSN 1680-7316.

[118] United States EPA. *2006 Edition of the Drinking Water Standards and Health Advisories*. U.S. Environmental Protection Agency, Washington, DC, epa 822-r-06-013 edition, 2006.

[119] United States EPA. *Air Quality Criteria for Ozone and Related Photochemical Oxidants (Final)*. U.S. Environmental Protection Agency, Washington, DC, epa/600/r-05/004af-cf edition, 2006.

[120] M. J. Evans and D. J. Jacob. Impact of new laboratory studies of N_2O_5 hydrolysis on global model budgets of tropospheric nitrogen oxides, ozone, and OH. *Geophys. Res. Lett.*, 32(9), May 13 2005. ISSN 0094-8276. doi: 10.1029/2005GL022469.

[121] J. M. Davis, P. V. Bhave, and K. M. Foley. Parameterization of N_2O_5 reaction probabilities on the surface of particles containing ammonium, sulfate, and nitrate. *Atmos. Chem. Phys*, 8:5295–5311, 2008.

[122] G. A. Grell, S. E. Peckham, R. Schmitz, S. A. McKeen, G. Frost, W. C. Skamarock, and B. Eder. Fully coupled "online" chemistry within the wrf model. *Atmos. Env.*, 39:6957–6975, 2005.

[123] X. Tie, S. Madronich, G. H. Li, Z. Ying, R. Zhang, A. R. Garcia, J. Lee-Taylor, and Y. Liu. Characterizations of chemical oxidants in mexico city: A regional chemical dynamical model (WRF-chem) study. *Atmos. Env.*, 41:1989–2008, 2007.

[124] W. R. Stockwell. A homogeneous gas-phase mechanism for use in a regional acid deposition model. *Atmos. Environ.*, 20(8):1615–1632, 1986. ISSN 1352-2310.

[125] J. A. Leone and J. H. Seinfeld. Comparative-analysis of chemical-reaction mechanisms for photochemical smog. *Atmos. Environ.*, 19(3): 437–464, 1985. ISSN 1352-2310.

[126] J. G. Calvert, A. Lazrus, G. L. Kok, B. G. Heikes, J. G. Walega, J. Lind, and C. A. Cantrell. Chemical mechanisms of acid generation in the troposphere. *Nature*, 317(6032):27–35, 1985. ISSN 0028-0836.

[127] R. Atkinson, D. L. Baulch, R. A. Cox, J. N. Crowley, Hampson Jr. R. F., J. A. Kerr, M. J. Rossi, and J. Troe. Summary of evaluated kinetic and photochemical data for atmospheric chemistry. Web Version, 2001. URL `www.iupac-kinetic.ch.cam.ac.uk,UniversityofCambridge,UK`.

[128] R. G. Derwent and M. E. Jenkin. Hydrocarbons and the Long-range Transport of Ozone and PAN Across Europe. *Atmos. Environ. A-Gen.*, 25(8):1661–1678, 1991. ISSN 0004-6981.

[129] G. J. McRae, W. R. Goodin, and J. H. Seinfeld. Development of a 2nd-generation mathematical-model for urban air-pollution - 1. model formulation. *Atmos. Environ.*, 16(4):679–696, 1982. ISSN 1352-2310.

[130] J. Nishino. Adsorption of water Vapor and carbon dioxide at carboxylic functional groups on the surface of coal. *Fuel*, 80(5):757–764, Apr 2001. ISSN 0016-2361.

[131] T. Letzel, U. Pöschl, E. Rosenberg, M. Grasserbauer, and R. Niessner. In-source fragmentation of partially oxidized mono- and polycyclic aromatic hydrocarbons in atmospheric pressure chemical ionization mass spectrometry coupled to liquid chromatography. *Rapid Commun. Mass Spectrom.*, 13(24):2456–2468, 1999. ISSN 0951-4198.

[132] T. Letzel, U. Pöschl, R. Wissiack, E. Rosenberg, M. Grasserbauer, and R. Niessner. Phenyl-modified reversed-phase liquid chromatography coupled to atmospheric pressure chemical ionization mass spectrometry: A universal method for the analysis of partially oxidized aromatic hydrocarbons. *Anal. Chem.*, 73(7):1634–1645, Apr 1 2001. ISSN 0003-2700. doi: 10.1021/ac001079t.

[133] U. Pöschl. Formation and decomposition of hazardous chemical components contained in atmospheric aerosol particles. *J. Aerosol Med.*, 15(2): 203–212, SUM 2002. ISSN 0894-2684.

[134] K. Tabor, L. Gutzwiller, and M. J. Rossi. Heterogeneous Chemical-Kinetics of NO_2 on Amorphous-Carbon at Ambient-Temperature. *J. Phys. Chem.*, 98(24):6172–6186, Jun 16 1994. ISSN 0022-3654.

[135] W. Choi and M. T. Leu. Nitric acid uptake and decomposition on black carbon (soot) surfaces: Its implications for the upper troposphere and

lower stratosphere. *J. Phys. Chem. A*, 102(39):7618–7630, Sep 24 1998. ISSN 1089-5639.

[136] T. C. Bond, D. G. Streets, K. F. Yarber, S. M. Nelson, J. H. Woo, and Z. Klimont. A technology-based global inventory of black and organic carbon emissions from combustion. *J. Geophys. Res.-Atmos.*, 109(D14), Jul 24 2004. ISSN 0148-0227. doi: 10.1029/2003JD003697.

[137] M. Kanakidou, J. H. Seinfeld, S. N. Pandis, I. Barnes, F. J. Dentener, M. C. Facchini, R. Van Dingenen, B. Ervens, A. Nenes, C. J. Nielsen, E. Swietlicki, J. P. Putaud, Y. Balkanski, S. Fuzzi, J. Horth, G. K. Moortgat, R. Winterhalter, C. E. L. Myhre, K. Tsigaridis, E. Vignati, E. G. Stephanou, and J. Wilson. Organic aerosol and global climate modelling: a review. *Atmos. Chem. Phys.*, 5:1053–1123, Mar 30 2005. ISSN 1680-7324.

[138] F. J. Dentener, G. R. Carmichael, Y. Zhang, J. Lelieveld, and P. J. Crutzen. Role of mineral aerosol as a reactive surface in the global troposphere. *J. Geophys. Res-Atmos.*, 101(D17):22869–22889, Oct 20 1996. ISSN 0148-0227.

[139] S. Seisel, C. Borensen, R. Vogt, and R. Zellner. Kinetics and mechanism of the uptake of N_2O_5 on mineral dust at 298 K. *Atmos. Chem. Phys.*, 5:3423–3432, Dec 19 2005. ISSN 1680-7324.

[140] S. S. Brown, T. B. Ryerson, A. G. Wollny, C. A. Brock, R. Peltier, A. P. Sullivan, R. J. Weber, W. P. Dube, M. Trainer, J. F. Meagher, F. C. Fehsenfeld, and A. R. Ravishankara. Variability in nocturnal nitrogen oxide processing and its role in regional air quality. *Science*, 311(5757): 67–70, Jan 6 2006. ISSN 0036-8075. doi: 10.1126/science.1120120.

[141] F. Karagulian, C. Santschi, and M. J. Rossi. The heterogeneous chemical kinetics of N_2O_5 on $CaCO_3$ and other atmospheric mineral dust surrogates. *Atmos. Chem. Phys.*, 6:1373–1388, May 2 2006. ISSN 1680-7316.

[142] D. A. Knopf, J. Mak, S. Gross, and A. K. Bertram. Does atmospheric processing of saturated hydrocarbon surfaces by NO_3 lead to volatilization? *Geophys. Res. Lett.*, 33(17), Sep 14 2006. ISSN 0094-8276. doi: 10.1029/2006GL026884.

[143] D. A. Knopf, L. M. Cosman, P. Mousavi, S. Mokamati, and A. K. Bertram. A novel flow reactor for studying reactions on liquid surfaces coated by organic monolayers: Methods, validation, and initial results. *J. Phys. Chem. A*, 111(43):11021–11032, 2007.

[144] L. M. Cosman, D. A. Knopf, and A. K. Bertram. N_2O_5 reactive uptake on aqueous sulfuric acid solutions coated with branched and straight-chain insoluble organic surfactants. *J. Phys. Chem. A*, 112(11):2386–2396, 2008.

[145] H. D. Osthoff, J. M. Roberts, A. R. Ravishankara, E. J. Williams, B. M. Lerner, R. Sommariva, T. S. Bates, D. Coffman, P. K. Quinn, J. E. Dibb, H. Stark, J. B. Burkholder, R. K. Talukdar, J. Meagher, F. C. Fehsenfeld, and S. S. Brown. High levels of nitryl chloride in the polluted subtropical marine boundary layer. *Nat. Geosci.*, 1(5):324–328, May 2008. ISSN 1752-0894. doi: {10.1038/ngeo177}.

[146] B. J. Finlayson-Pitts and J. N. Pitts. Tropospheric air pollution: Ozone, airborne toxics, polycyclic aromatic hydrocarbons, and particles. *Science*, 276(5315):1045–1052, May 16 1997. ISSN 0036-8075.

[147] T. Franze, M. G. Weller, R. Niessner, and U. Pöschl. Enzyme immunoassays for the investigation of protein nitration by air pollutants. *Analyst*, 128(7):824–831, 2003. ISSN 0003-2654. doi: 10.1039/b303132b.

[148] T. Franze, M. G. Weller, R. Niessner, and U. Pöschl. Protein nitration by polluted air. *Environ. Sci. Technol.*, 39(6):1673–1678, Mar 15 2005. ISSN 0013-936X. doi: 10.1021/es0488737.

[149] J. A. Bernstein, N. Alexis, C. Barnes, I. L. Bernstein, J. A. Bernstein, A. Nel, D. Peden, D. Diaz-Sanchez, S. M. Tarlo, and P. B. Williams. Health effects of air pollution. *J. Allergy Clin. Immun.*, 114(5):1116–1123, Nov 2004. ISSN 0091-6749. doi: 10.1016/j.jaci.2004.08.030.

[150] F. Arens, L. Gutzwiller, H. W. Gaggeler, and M. Ammann. The reaction of NO_2 with solid anthrarobin (1,2,10-trihydroxy-anthracene). *Phys. Chem. Chem. Phys.*, 4(15):3684–3690, 2002. ISSN 1463-9076. doi: 10.1039/b201713j.

[151] A. K. Bertram, A. V. Ivanov, M. Hunter, L. T. Molina, and M. J. Molina. The reaction probability of oh on organic surfaces of tropospheric interest. *J. Phys. Chem. A*, 105:9415–9421, 2001.

[152] M. J. Molina, A. V. Ivanov, S. Trakhtenberg, and L. T. Molina. Atmospheric evolution of organic aerosol. *Geophys. Res. Lett.*, 31, 2004. doi: 10.1029/2004GL020910.

[153] J. D. Hearn and Smith G. D. A mixed-phase relative rates technique for measuring aerosol reaction kinetics. *Geophys. Res. Lett.*, 33, 2006. doi: 10.1029/2006GL026963.

[154] J. H. Park, A. V. Ivanov, and M. J. Molina. Effect of relative humidity on oh uptake by surfaces of atmospheric importance. *J. Phys. Chem. A*, 112:6968–6977, 2008.

[155] S. Gross and A. K. Bertram. Products and kinetics of the reactions of an alkane monolayer and a terminal alkene monolayer with no_3 radicals. *J. Geophys. Res.-Atmos.*, 114, 2009. doi: 10.1029/2008JD010987.

[156] W. J. Massman. A review of the molecular diffusivities of H_2O, CO_2, CH_4, CO, O_3, SO_2, NH_3, N_2O, NO, AND NO_2 in air, O_2 AND N_2 near STP. *Atmos. Environ.*, 32(6):1111–1127, Mar 1998. ISSN 1352-2310.

[157] K. H. Homann. Fullerenes and soot formation - New pathways to large particles in flames. *Angew. Chem., Int. Ed*, 37(18):2435–2451, 1998. ISSN 1433-7851.

[158] S. Kamm, O. Mohler, K. H. Naumann, H. Saathoff, and U. Schurath. The heterogeneous reaction of ozone with soot aerosol. *Atmos. Environ.*, 33(28):4651–4661, Dec 1999. ISSN 1352-2310.

[159] W. F. Rogge, M. A. Mazurek, L. M. Hildemann, G. R. Cass, and B. R. T. Simoneit. Quantification of urban organic aerosols at a molecular-level - identification, abundance and seasonal-variation. *Atmos. Environ. A-Gen.*, 27(8):1309–1330, Jun 1993. ISSN 0004-6981.

[160] M. D. Petters, A. J. Prenni, S. M. Kreidenweis, P. J. DeMott, A. Matsunaga, Y. B. Lim, and P. J. Ziemann. Chemical aging and the hydrophobic-to-hydrophilic conversion of carbonaceous aerosol. *Geophys. Res. Lett.*, 33(24):1107–1118, 2006.

[161] J. E. Shilling, S. M. King, M. Mochida, and S. T. Martin. Mass spectral evidence that small changes in composition caused by oxidative aging processes alter aerosol CCN properties. *J. Phys. Chem. A*, 111(17): 3358–3368, May 3 2007. ISSN 1089-5639. doi: 10.1021/jp068822r.

[162] K. Stemmler, M. Ammann, C. Donders, J. Kleffmann, and C. George. Photosensitized reduction of nitrogen dioxide on humic acid as a source of nitrous acid. *Nature*, 440(7081):195–198, Mar 9 2006. ISSN 0028-0836. doi: 10.1038/nature04603.

[163] D. R. Hanson and A. R. Ravishankara. The reaction probabilities of $ClONO_2$ and N_2O_5 on 40-percent to 75-percent sulfuric-acid-solutions. *J. Geophys. Res.-Atmos.*, 96(D9):17307–17314, Sep 20 1991. ISSN 0148-0227.

[164] D. J. Donaldson and V. Vaida. The influence of organic films at the air-aqueous boundary on atmospheric processes. *Chem. Rev.*, 106:1445–1461, 2006. doi: 10.1021/cr040367c.

[165] H Naoe and K Okada. Mixing properties of submicrometer aerosol particles in the urban atmosphere - with regard to soot particles. *Atmos. Environ.*, 35(33):5765–5772, Nov 2001. ISSN 1352-2310.

[166] N. Riemer, H. Vogel, and B. Vogel. Soot aging time scales in polluted regions during day and night. *Atmos. Chem. Phys.*, 4:1885–1893, Sep 15 2004. ISSN 1680-7324.

[167] G. B. Ellison, A. F. Tuck, and V. Vaida. Atmospheric processing of organic aerosols. *J. Geophys. Res.-Atmos.*, 104(D9):11633–11641, May 20 1999. ISSN 0747-7309.

Appendix A

Units

In gas-phase reactions, concentrations are usually expressed in $\frac{\text{(molecules)}}{\text{cm}^3}$ or, in the context of gaseous pollutants, in parts per million by volume (ppmv). Both units can be converted into each other by using the ideal gas law $pV = Nk_\text{B}T$, where p is the pressure (in hPa; 1 hPa = 100 Pa), V the volume, $k_\text{B} = 1.381 \times 10^{23}$ J K^{-1} the Boltzmann constant, N the number of molecules, and T the temperature. With this, the conversion from ppmv to cm^{-3} is: 1 ppmv $= 10^{-6}\frac{N}{V} = 10^{-6}\frac{p}{Tk_\text{B}} = 2.46 \times 10^{13}$ cm^{-3}.

Appendix B

Resistor Model Formulation of Surface Reactions

Under steady-state conditions, Langmuir-Hinshelwood surface reactions can be expressed in resistor-model form. Without the loss of generality, it is assumed that the Langmuir-Hinshelwood surface reaction occurs between a surface component Y and a gas-phase molecule species X after adsorption onto the surface (without accounting for gas-phase diffusion processes, although they could be easily included). The elementary processes governing the uptake are adsorption, desorption, and surface reactions.

Under steady-state conditions, the rate of adsorption equals the rate of desorption. The resulting *Langmuir equilibrium* can be described by an Langmuir equilibrium constant K, which relates the filled surface sites, here expressed by the surface coverage with the molecules X, θ_{X}, to the empty surface sites, expressed by the complement, $1 - \theta_{\mathrm{X}}$, and the particle concentration in the gas phase, $[\mathrm{X}]_{\mathrm{g}}$:

$$K = \frac{\theta_{\mathrm{X}}}{(1 - \theta_{\mathrm{X}})[\mathrm{X}]_{\mathrm{g}}} \,. \tag{B.1}$$

Rearranging this leads to the Langmuir equation:

$$\theta_{\mathrm{X}} = \frac{K[\mathrm{X}]_{\mathrm{g}}}{1 + K[\mathrm{X}]_{\mathrm{g}}} \,. \tag{B.2}$$

To express the Langmuir equilibrium constant, as it is commonplace, in terms of rate constants, the adsorption and desorption fluxes (2.41) and (2.45) can be divided by the included concentrations to obtain the respective rate

constants:

$$k_{\mathrm{a}} = \frac{1}{4}\alpha_0\omega_{\mathrm{X}} \,, \tag{B.3}$$

$$k_{\mathrm{d}} = \frac{1}{\tau_{\mathrm{X}}} \,. \tag{B.4}$$

Applying the steady-state condition, i. e. equating the rate of adsorption with the rate of desorption, yields:

$$k_{\mathrm{a}}[\mathrm{X}]_{\mathrm{g}}(1-\theta_{\mathrm{X}}) = k_{\mathrm{d}}[\mathrm{X}]_{\mathrm{s}} \,. \tag{B.5}$$

Using $\theta_{\mathrm{X}} = [\mathrm{X}]_{\mathrm{s}}\sigma_{\mathrm{X}} \Leftrightarrow [\mathrm{X}]_{\mathrm{s}} = \theta_{\mathrm{X}}/\sigma_{\mathrm{X}}$, (B.5) can be cast into the form of (B.1) with an Langmuir equilibrium constant of:

$$K = \frac{\sigma_{\mathrm{X}}k_{\mathrm{a}}}{k_{\mathrm{d}}} \,. \tag{B.6}$$

A bimolecular surface reaction with a rate of:

$$r_{\mathrm{s}} = k_{\mathrm{s}}[\mathrm{Y}]_{\mathrm{s}}[\mathrm{X}]_{\mathrm{s}} = k_{\mathrm{s}}^1[\mathrm{X}]_{\mathrm{s}} \,, \tag{B.7}$$

where k_{s}^1 the apparent first-order rate constant for that reaction, shifts the adsorption-desorption equilibrium to:

$$k_{\mathrm{a}}[\mathrm{X}]_{\mathrm{g}}(1-\theta_{\mathrm{X}}) = (k_{\mathrm{d}} + k_{\mathrm{s}}^1)\frac{\theta_{\mathrm{X}}}{\sigma_{\mathrm{X}}} \tag{B.8}$$

with

$$K' = \frac{\sigma_{\mathrm{X}}k_{\mathrm{a}}}{k_{\mathrm{d}} + k_{\mathrm{s}}^1} \,. \tag{B.9}$$

The uptake coefficient can be obtained by dividing the net loss on the surface, which in the adsorption-desorption equilibrium is only due to the surface reaction, by the collision flux of molecules X with the surface:

$$\gamma_{\mathrm{X}} = \frac{k_{\mathrm{s}}^1[\mathrm{X}]_{\mathrm{s}}}{\frac{1}{4}\omega_{\mathrm{X}}[\mathrm{X}]_{\mathrm{g}}} \,. \tag{B.10}$$

Using $[\mathrm{X}]_{\mathrm{s}} = \theta_{\mathrm{X}}/\sigma_{\mathrm{X}}$, inserting the K'-replaced version of (B.2), and using (B.9) and (B.3) yields:

$$\gamma_{\mathrm{X}} = \frac{\alpha_0 k_{\mathrm{s}}^1}{(k_{\mathrm{d}} + k_{\mathrm{s}}^1) + \frac{1}{4}\alpha_0\sigma_{\mathrm{X}}\omega_{\mathrm{X}}[\mathrm{X}]_{\mathrm{g}}} \,. \tag{B.11}$$

This can be inverted and rearranged to:

$$\frac{1}{\gamma_{\mathrm{X}}} = \frac{1}{\alpha_0} + \frac{1}{k_{\mathrm{s}}^1}\left[\frac{k_{\mathrm{d}}}{\alpha_0} + \frac{\sigma_{\mathrm{X}}\omega_{\mathrm{X}}[\mathrm{X}]_{\mathrm{g}}}{4}\right] , \tag{B.12}$$

which is now in the resistance model form of:

$$\frac{1}{\gamma_{\mathrm{X}}} = \frac{1}{\alpha_0} + \frac{1}{\Gamma_{\mathrm{s}}} \tag{B.13}$$

with

$$\frac{1}{\Gamma_{\mathrm{s}}} = \frac{1}{k_{\mathrm{s}}^1}\left[\frac{k_{\mathrm{d}}}{\alpha_0} + \frac{\sigma_{\mathrm{X}}\omega_{\mathrm{X}}[\mathrm{X}]_{\mathrm{g}}}{4}\right] = \frac{\omega_{\mathrm{X}}\sigma_{\mathrm{X}}(1 + K[\mathrm{X}]_{\mathrm{g}})}{4k_{\mathrm{s}}[\mathrm{Y}]_{\mathrm{s}}K} . \tag{B.14}$$

This completes the derivation for a Langmuir-Hinshelwood surface reaction term for the resistor model. Competitive co-adsorption of multiple species and multiple surface reactions can be inserted into this derivation in a straightforward manner.

However, expression (B.14) is only valid for an adsorption-desorption equilibrium, which may not be realized for all steps of the uptake process and the subsequent surface reactions.

Appendix C

Chemical Species and Reactions in RADM2

The following lists of chemical species and reactions included in the RADM2 mechanism have been adapted from Stockwell et al. [13].

TABLE 1. RADM2 Chemical Species List

	Species	Definition	Carbon Number*	Molecular Weight *
		Stable Inorganic Compounds		
	Nitrogen			
1.	NO_2	Nitrogen dioxide		46
2.	NO	Nitric oxide		30
3.	HONO	Nitrous acid		47
4.	NO_3	Nitrogen trioxide		62
5.	N_2O_5	Nitrogen pentoxide		108
6.	HNO_4	Pernitric acid		79
7.	HNO3	Nitric acid		63
	Oxidants			
8.	O_3	Ozone		48
9.	H_2O_2	Hydrogen peroxide		34
	Sulfur			
10.	SO_2	Sulfur dioxide		64
11.	SULF	Sulfuric acid		98
	Carbon oxides			
12.	CO	Carbon monoxide		28
13.	CO_2	Carbon dioxide (product only)		44
14.	H_2	Hydrogen (product only)		2
		Inorganic Short-Lived Intermediates		
	Atomic species			
15.	O^3P	Ground state oxygen atom		16
16.	O^1D	Excited state oxygen atom		16
	Odd hydrogen			
17.	HO	Hydroxy radical		17
18.	HO_2	Hydroperoxy radical		33
		Abundant Stable Species		
19.	O_2	Oxygen		32
20.	N_2	Nitrogen		28
21.	H_2O	Water		18
		Stable Organic Compounds		
	Alkanes			
22.	CH_4	Methane	1.0	16
23.	ETH	Ethane	2.0	30
24.	HC3	Alkanes with HO rate constant (298, 1 atm) between $2.7x10^{-13}$ and $3.4x10^{-12}$	2.9	44
25.	HC5	Alkanes with HO rate constant (298, 1 atm) between $3.4x10^{-12}$ and $6.8x10^{-12}$	4.8	72
26.	HC8	Alkanes with HO rate constant (298, 1 atm) greater than $6.8x10^{-12}$	7.9	114

TABLE 1. (continued)

	Species	Definition	Carbon Number*	Molecular Weight *
	Alkenes			
27.	OL2	Ethene	2.0	28
28.	OLT	Terminal alkenes	3.8	42
29.	OLI	Internal alkenes	4.8	56
30.	ISO	Isoprene	5.0	68
	Aromatic			
31.	TOL	Toluene and less reactive aromatics	7.1	92
32.	CSL	Cresol and other hydroxy substituted aromatics	6.6	108
33.	XYL	Xylene and more reactive aromatics	8.9	106
	Carbonyls			
34.	HCHO	Formaldehyde	1.0	30
35.	ALD	Acetaldehyde and higher aldehydes	2.4	44
36.	KET	Ketones	3.9	72
37.	GLY	Glyoxal	2.0	58
38.	MGLY	Methylglyoxal	3.0	72
39.	DCB	Unsaturated Dicarbonyl	4.2	87
	Organic nitrogen			
40.	PAN	Peroxyacetyl nitrate and higher PANs	2.0	121
41.	TPAN	H(CO)CH=CHCO3NO2	4.0	147
42.	ONIT	Organic nitrate	4.0	119
	Organic peroxides			
43.	OP1	Methyl hydrogen peroxide	1.0	48
44.	OP2	Higher organic peroxides	2.0	62
45.	PAA	Peroxyacetic acid	2.0	76
	Organic acids			
46.	ORA1	Formic acid	1.0	46
47.	ORA2	Acetic acid and higher acids	2.0	60
		Organic Short-Lived Intermediates		
	Peroxy radicals from alkanes			
48.	MO2	Methyl peroxy radical	1.0	47
49.	ETHP	Peroxy radical formed from alkane, ETH	2.0	61
50.	HC3P	Peroxy radical formed from alkane, HC3	2.9	75
51.	HC5P	Peroxy radical formed from alkane, HC5	4.8	103
52.	HC8P	Peroxy radical formed from alkane, HC8	7.9	145
	Peroxy radicals from alkenes			
53.	OL2P	Peroxy radical formed from alkene, OL2	2.0	77
54.	OLTP	Peroxy radical formed from alkene, OLT	3.8	91
55.	OLIP	Peroxy radical formed from alkene, OLIP	4.8	105
	Peroxy radicals from aromatics			
56.	TOLP	Peroxy radical formed from aromatic, TOL	7.1	141
57.	XYLP	Peroxy radical formed from aromatic, XYL	8.9	155
	Peroxy radicals with carbonyl groups			
58.	ACO_3	Acetylperoxy radical	2.0	75
59.	KETP	Peroxy radical formed from ketone, KET	3.9	103
60.	TCO_3	$H(CO)CH=CHCO_3$	4.0	115
	Peroxy radicals involving nitrogen			
61.	OLN	NO3-alkene adduct	3.0	136
62.	XNO_2	Accounts for additional organic nitrate formation affected by the lumped organic species	—	—
63.	XO_2	Accounts for additional NO to NO2 conversions affected by the lumped organic species	—	—

*Carbon number and molecular weight are representative averages when more than one emitted chemical is included in RADM class.

TABLE 2*a*. The RADM2 Chemical Mechanism: Photolysis Reactions

		Rate Constant*	Cross Section	Quantum Yield
1.	$NO_2 + h\nu \rightarrow O^3P + NO$	7.72×10^{-3}	*Bass et al.* [1976]; *Davenport* [1978]	*Gardner et al.* [1987]
2.	$O_3 + h\nu \rightarrow O^1D + O_2$	1.70×10^{-5}	*DeMore* et al. [1988]	*Moortgat and Kudzus* [1978]; scaled by 0.9
3.	$O_3 + h\nu \rightarrow O^3P + O_2$	4.22×10^{-4}	Same reference as reaction 2	Total yield for O^1D and O^3P assumed unity
4.	$HONO + h\nu \rightarrow HO + NO$	1.39×10^{-3}	*Stockwell and Calvert* [1978]	Assumed = 1 over UV absorption range
5.	$HNO_3 + h\nu \rightarrow HO + NO_2$	2.75×10^{-7}	*Molina and Molina* [1981]	Assumed = 1 over UV absorption range
6.	$HNO_4 + h\nu \rightarrow HO_2 + NO_2$	4.58×10^{-6}	*Molina and Molina* [1981]	Assumed = 1 over UV absorption range
7.	$NO_3 + h\nu \rightarrow NO + O_2$	2.02×10^{-2}	$\lambda < 570$ *Graham and Johnston* [1978]; $\lambda > 570$ average of *Graham and Johnston* [1978] and Ravishankara and *Wine* [1983]	*Magnotta and Johnston* [1980]; *Graham and Johnston* [1978]; scaled to a total yield of unity
8.	$NO_3 + h\nu \rightarrow NO_2 + O^3P$	1.64×10^{-1}	Same references as reaction 7	Same references as reaction 7
9.	$H_2O_2 + h\nu \rightarrow 2\ HO$	5.67×10^{-6}	Average of *Lin et al.* [1978] and *Molina and Molina* [1981]	Assumed = 1 over UV absorption range
10.	$HCHO + h\nu \rightarrow H_2 + CO$	3.32×10^{-5}	Average of *Moortgat et al.* [1980,1983] and *Bass et al.* [1980]	Moortgat et al. [1983]; Horowitz and Calvert [1978]; Pressure dependent†
11.	$HCHO + h\nu \rightarrow 2\ HO_2 + CO$	2.18×10^{-5}	Same references as reaction 10	Same references as reaction 10
12.	$ALD + h\nu \rightarrow MO_2 + HO_2 + CO$	3.55×10^{-6}	Average of *Calvert and Pitts* [1966] and Meyrahn [1984]	*Meyrahn et al.* [1981]; Pressure dependent†
13.	$OP1 + h\nu \rightarrow HCHO + HO_2 + HO$	5.57×10^{-6}	*Molina and Arguello* [1979]	Assumed = 1 over UV absorption range
14.	$OP2 + h\nu \rightarrow ALD + HO_2 + HO$	5.57×10^{-6}	Same reference as reaction 13	Same reference as reaction 13

TABLE 2*a*. (continued)

		Rate Constant*	Cross Section	Quantum Yield
15.	PAA + *hv* -> MO_2 + CO_2 + HO	1.59×10^{-6}	H_2O_2 cross section scaled by 0.28; *Giguere and Olmos* [1956]	Assumed = 1 over UV absorption range
16.	KET + *hv* -> ACO_3 + ETHP	6.07×10^{-7}	Methyl ethyl ketone; *Calvert and Pitts* [1966]	*Gardner et al.* [1984]
17.	GLY + *hv* -> 0.13 HCHO + 1.87 CO	4.98×10^{-5}	*Plum et al.* [1983]	*Plum et al.* [1983]
18.	GLY + *hv* -> 0.45 HCHO + 1.55 CO + 0.80 HO_2	5.17×10^{-5}	Same reference as reaction 17	*Langford and Moore* [1984]
19.	MGLY + *hv* -> ACO_3 + HO_2 + CO	1.44×10^{-4}	*Plum et al.* [1983]	*Plum et al.* [1983]; *Langford and Moore* [1984]
20.	DCB + *hv* -> 0.98 HO_2 + TCO_3 + 0.02 ACO_3	4.30×10^{-4}	See text	See text
21.	ONIT + *hv* -> 0.20 ALD + 0.80 KET + HO_2 + NO_2	7.95×10^{-7}	*Calvert and Pitts* [1966]	Assumed = 1 over UV absorption range

*Photolysis rate constants (sec^{-1}) are given for solar zenith angle 40°, June 21, summer surface 40° north latitude.
†Pressure dependence given by $\varphi_{\lambda,p} = \varphi_{\lambda,1atm}/\{\varphi_{\lambda,1atm} + [1 - \varphi_{\lambda,760}]P/P_{1atm}\}$

TABLE 2*b*. The RADM2 Chemical Mechanism: Thermal Reactions; $k = A \exp[-E/(RT)]$

		A*	E/R	Note
1.	$O^3P + NO_2$ -> NO + O_2	6.5×10^{-12}	-120.	a
2.	$O^1D + N_2$ -> O^3P + N_2	1.8×10^{-11}	-110.	a
3.	$O^1D + O_2$ -> O^3P + O_2	3.2×10^{-11}	-70.	a
4.	$O^1D + H_2O$ -> 2 HO	2.2×10^{-10}	0.	a
5.	O_3 + NO -> NO_2 + O_2	2.0×10^{-12}	1400.	a
6.	O_3 + HO-> HO_2 + O_2	1.6×10^{-12}	940.	a
7.	$O_3 + HO_2$ -> HO + 2 O_2	1.1×10^{-14}	500.	a
8.	HO_2 + NO -> NO_2 + HO	3.7×10^{-12}	-240.	a
9.	H_2O_2 + HO -> HO_2 + H_2O	3.3×10^{-12}	200.	a
10.	NO + NO + O_2 -> NO_2 + NO_2	3.3×10^{-39}	-530.	b
11.	$O_3 + NO_2$ -> NO_3	1.4×10^{-13}	2500.	a
12.	NO_3 + NO -> NO_2 + NO_2	1.7×10^{-11}	-150.	a
13.	$NO_3 + NO_2$ -> NO + NO_2 + O_2	2.5×10^{-14}	1230.	b
14.	$NO_3 + HO_2$ -> HNO_3 + O_2	2.5×10^{-12}		c
15.	$N_2O_5 + H_2O$ -> 2 HNO_3	2.0×10^{-21}		a
16.	HO + HNO_4 -> NO_2 + H_2O + O_2	1.3×10^{-12}	-380.	a, d
17.	HO + HO_2 -> H_2O + O_2	4.6×10^{-11}	-230.	a
18.	CH_4 + HO -> MO_2 + H_2O	6.95×10^{-18}	1280.	e, f
19.	ETH + HO -> ETHP + H_2O	1.37×10^{-17}	444.	e, f
20.	HC3 + HO -> 0.83 HC3P + 0.17 HO_2 + 0.009 HCHO + 0.075 ALD + 0.025 KET + H_2O	1.59×10^{-11}	540.	e, g
21.	HC5 + HO -> HC5P + 0.25 XO_2 + H_2O	1.73×10^{-11}	380.	e, h
22.	HC8 + HO -> HC8P + 0.75 XO_2 + H_2O	3.64×10^{-11}	380.	e, i
23.	OL2 + HO -> OL2P	2.15×10^{-12}	-411.	e

TABLE 2b. (continued)

		A^*	E/R	Note
24.	OLT + HO -> OLTP	5.32×10^{-12}	-504.	e
25.	OLI + HO -> OLIP	1.07×10^{-11}	-549.	e
26.	TOL + HO -> 0.75 TOLP + 0.25 CSL + 0.25 HO_2	2.1×10^{-12}	-322.	e, j
27.	XYL + HO -> 0.83 XYLP + 0.17 CSL + 0.17 HO_2	1.89×10^{-11}	-116.	j, k
28.	CSL + HO -> 0.1 HO_2 + 0.9 XO_2 + 0.9 TCO_3 - 0.9 HO	4.0×10^{-11}		e
29.	HCHO + HO -> HO_2 + CO + H_2O	9.0×10^{-12}		e
30.	ALD + HO -> ACO_3 + H_2O	6.87×10^{-12}	-256.	e
31.	KET + HO -> KETP + H_2O	1.2×10^{-11}	745.	l
32.	GLY + HO -> HO_2 + 2 CO + H_2O	1.15×10^{-11}		b
33.	MGLY + HO -> ACO_3 + CO + H_2O	1.7×10^{-11}		b
34.	DCB + HO -> TCO_3 + H_2O	2.8×10^{-11}		l
35.	OP1 + HO -> 0.5 MO_2 + 0.5 HCHO + 0.5 HO	1.0×10^{-11}		m
36.	OP2 + HO -> 0.5 HC3P + 0.5 ALD + 0.5 HO	1.0×10^{-11}		m
37.	PAA + HO -> ACO_3 + H_2O	1.0×10^{-11}		m
38.	PAN + HO -> HCHO + NO_3 + XO_2	6.85×10^{-18}	444.	f, n
39.	ONIT + HO -> HC3P + NO_2	1.55×10^{-11}	540.	e
40.	ISO + HO -> OLTP	2.55×10^{-11}	-409.	e
41.	ACO_3 + NO_2 -> PAN	2.8×10^{-12}	-181.	l
42.	PAN -> ACO_3 + NO_2	1.95×10^{16}	13543.	b
43.	TCO_3 + NO_2 -> TPAN	4.7×10^{-12}		j
44.	TPAN -> TCO_3 + NO_2	1.95×10^{16}	13543.	j
45.	MO_2 + NO -> HCHO + HO_2 + NO_2	4.2×10^{-12}	-180.	a
46.	HC3P + NO -> 0.75 ALD + 0.25 KET + 0.09 HCHO + 0.036 ONIT + 0.964 NO_2 + 0.964 HO_2	4.2×10^{-12}	-180.	a, b
47.	HC5P + NO -> 0.38 ALD + 0.69 KET + 0.08 ONIT + 0.92 NO_2 + 0.92 HO_2	4.2×10^{-12}	-180.	a, b
48.	HC8P + NO -> 0.35 ALD + 1.06 KET + 0.04 HCHO + 0.24 ONIT + 0.76 NO_2 + 0.76 HO_2	4.2×10^{-12}	-180.	a,b
49.	OL2P + NO -> 1.6 HCHO + HO_2 + NO_2 + 0.2 ALD	4.2×10^{-12}	-180.	a, b, j , m
50.	OLTP + NO -> ALD + HCHO + HO_2 + NO_2	4.2×10^{-12}	-180.	a, b
51.	OLIP + NO -> HO_2 + 1.45 ALD + 0.28 HCHO + 0.10 KET + NO_2	4.2×10^{-12}	-180.	a, b
52.	ACO3 + NO -> MO_2 + NO_2	4.2×10^{-12}	-180.	a, b
53.	TCO3 + NO -> NO_2 + 0.92 HO_2 + 0.89 GLY + 0.11 MGLY + 0.05 ACO3 + 0.95 CO + 2 XO_2	4.2×10^{-12}	-180.	a, b
54.	TOLP + NO -> NO_2 + HO_2 + 0.17 MGLY + 0.16 GLY + 0.70 DCB	4.2×10^{-12}	-180.	a, b, j
55.	XYLP + NO -> NO_2 + HO_2 + 0.45 MGLY + 0.806 DCB	4.2×10^{-12}	-180.	a, b, j
56.	ETHP + NO -> ALD + HO_2 + NO_2	4.2×10^{-12}	-180.	a, b
57.	KETP + NO -> MGLY + NO_2 + HO_2	4.2×10^{-12}	-180.	a, b
58.	OLN + NO -> HCHO + ALD + 2 NO_2	4.2×10^{-12}	-180.	a, b
59.	HCHO + NO_3 -> HO_2 + HNO3 + CO	6.0×10^{-13}	2058.	c
60.	ALD + NO_3 -> ACO_3 + HNO3	1.4×10^{-12}	1900.	a
61.	GLY + NO_3 -> HNO_3 + HO2 + 2 CO	6.0×10^{-13}	2058.	a, l
62.	MGLY + NO_3 -> HNO_3 + ACO_3 + CO	1.4×10^{-12}	1900.	a, l
63.	DCB + NO_3 -> HNO_3 + TCO_3	1.4×10^{-12}	1900.	a, l
64.	CSL + NO_3 -> HNO_3 + XNO_2 + 0.5 CSL	2.2×10^{-11}		l
65.	OL2 + NO_3 -> OLN	2.0×10^{-12}	2923.	l
66.	OLT + NO_3 -> OLN	1.0×10^{-11}	1895.	l
67.	OLI + NO_3 -> OLN	3.23×10^{-11}	975.	l
68.	ISO + NO_3 -> OLN	5.81×10^{-13}		
69.	OL2 + O_3 -> HCHO + 0.42 CO + 0.4 ORA1 + 0.12 HO_2	1.2×10^{-14}	2633.	m, o

TABLE 2*b*. (continued)

		A^*	*E/R*	Note
70.	OLT + O_3 -> 0.53 HCHO + 0.50 ALD + 0.33 CO + 0.20 ORA1 + 0.20 ORA2 + 0.23 HO_2 + 0.22 MO_2 + 0.10 HO + 0.06 CH_4	1.32×10^{-14}	2105.	m, o
71.	OLI + O_3 -> 0.18 HCHO + 0.72 ALD + 0.10 KET + 0.23 CO + 0.06 ORA1 + 0.29 ORA2 + 0.09 CH_4 + 0.26 HO_2 + 0.14 HO + 0.31 MO_2	7.29×10^{-15}	1136.	m, o
72.	ISO + O_3 -> 0.53 HCHO + 0.50 ALD + 0.33 CO + 0.20 ORA1 + 0.20 ORA2 + 0.23 HO_2 + 0.22 MO_2 + 0.10 HO	1.23×10^{-14}	2013.	m, o
73.	HO_2 + MO_2 -> OP1	7.7×10^{-14}	-1300.	a
74.	HO_2 + ETHP -> OP2	7.7×10^{-14}	-1300.	a
75.	HO_2 + HC3P -> OP2	7.7×10^{-14}	-1300.	a
76.	HO_2 + HC5P -> OP2	7.7×10^{-14}	-1300.	a
77.	HO_2 + HC8P -> OP2	7.7×10^{-14}	-1300.	a
78.	HO_2 + OL2P -> OP2	7.7×10^{-14}	-1300.	a
79.	HO_2 + OLTP -> OP2	7.7×10^{-14}	-1300.	a
80.	HO_2 + OLIP -> OP2	7.7×10^{-14}	-1300.	a
81.	HO_2 + KETP -> OP2	7.7×10^{-14}	-1300.	a
82.	HO_2 + ACO_3 -> PAA	7.7×10^{-14}	-1300.	a
83.	HO_2 + TOLP -> OP2	7.7×10^{-14}	-1300.	a
84.	HO_2 + XYLP -> OP2	7.7×10^{-14}	-1300.	a
85.	HO_2 + TCO_3 -> OP2	7.7×10^{-14}	-1300.	a
86.	HO_2 + OLN -> ONIT	7.7×10^{-14}	-1300.	a
87.	MO_2 + MO_2 -> 1.5 HCHO + HO_2	1.9×10^{-13}	-220.	a, l
88.	MO_2 + ETHP -> 0.75 HCHO + HO_2 + 0.75 ALD	1.4×10^{-13}	-220.	a, b
89.	MO_2 + HC3P -> 0.84 HCHO + HO_2 + 0.77 ALD + 0.26 KET	4.2×10^{-14}	-220.	a, b
90.	MO_2 + HC5P -> 0.77 HCHO + HO_2 + 0.41 ALD + 0.75 KET	3.4×10^{-14}	-220.	a, b
91.	MO_2 + HC8P -> 0.80 HCHO + HO_2 + 0.46 ALD + 1.39 KET	2.9×10^{-14}	-220.	a, b
92.	MO_2 + OL2P -> 1.55 HCHO + HO_2 + 0.35 ALD	1.4×10^{-13}	-220.	a, b
93.	MO_2 + OLTP -> 1.25 HCHO + HO_2 + 0.75 ALD	1.4×10^{-13}	-220.	a, b
94.	MO_2 + OLIP -> 0.89 HCHO + HO_2 + 0.725 ALD + 0.55 KET	1.7×10^{-14}	-220.	a, b
95.	MO_2 + KETP -> 0.75 HCHO + HO_2 + 0.75 MGLY	1.7×10^{-14}	-220.	a, b
96.	MO_2 + ACO_3 -> HCHO + 0.5 HO_2 + 0.5 MO_2 + 0.5 ORA2	9.6×10^{-13}	-220.	a, b
97.	MO_2 + TOLP -> HCHO + 2 HO_2 + 0.17 MGLY + 0.16 GLY + 0.70 DCB	1.7×10^{-14}	-220.	a, b
98.	MO_2 + XYLP -> HCHO + 2 HO_2 + 0.45 MGLY + 0.806 DCB	1.7×10^{-14}	-220.	a, b
99.	MO_2 + TCO_3 -> 0.50 HCHO + 0.50 ORA2 + 0.460 HO_2 + 0.445 GLY + 0.055 MGLY + 0.025 ACO_3 + 0.475 CO + XO_2	9.6×10^{-13}	-220.	a, b
100.	MO_2 + OLN -> 1.75 HCHO + 0.5 HO_2 + ALD + NO_2	1.7×10^{-14}	-220.	a, b
101.	ETHP + ACO_3 -> ALD + 0.5 HO_2 + 0.5 MO_2 + 0.5 ORA2	3.4×10^{-13}	-220.	a, b

Table 2*b*. (continued)

		A^*	*E/R*	Note
102.	HC3P + ACO_3 -> 0.77 ALD + 0.26 KET + 0.5 HO_2 + 0.5 MO_2 + 0.5 ORA2	1.0×10^{-13}	-220.	a, b
103.	HC5P + ACO_3 -> 0.4' ALD + 0.75 KET + 0.5 HO_2 + 0.5 MO_2 + 0.5 ORA2	8.4×10^{-14}	-220.	a, b
104.	HC8P + ACO_3 -> 0.46 ALD + 1.39 KET + 0.5 HO_2 + 0.5 MO_2 + 0.5 ORA2	7.2×10^{-14}	-220.	a, b
105.	OL2P + ACO_3 -> 0.8 HCHO + 0.6 ALD + 0.5 HO_2 + 0.5 MO_2 + 0.5 ORA2	3.4×10^{-13}	-220.	a, b
106.	OLTP + ACO_3 -> ALD + 0.5 HCHO + 0.5 HO_2 + 0.5 MO_2 + 0.5 ORA2	3.4×10^{-13}	-220.	a, b
107.	OLIP + ACO_3 -> 0.725 ALD + 0.55 KET + 0.14 HCHO + 0.50 HO_2 + 0.50 MO_2 + 0.50 ORA2	4.2×10^{-14}	-220.	a, b
108.	KETP + ACO_3 -> MGLY + 0.5 HO_2 + 0.5 MO_2 + 0.5 ORA2	4.2×10^{-14}	-220.	a, b
109.	ACO_3 + ACO_3 -> 2 MO_2	1.19×10^{-12}	-220.	a, b
110.	ACO_3 + TOLP -> MO_2 + 0.17 MGLY + 0.16 GLY + 0.7 DCB + HO_2	4.2×10^{-14}	-220.	a, b
111.	ACO_3 + XYLP -> MO_2 + 0.45 MGLY + 0.806 DCB + HO_2	4.2×10^{-14}	-220.	a,b
112.	ACO_3 + TCO3 -> MO_2 + 0.92 HO_2 + 0.89 GLY + 0.11 MGLY + 0.05 ACO_3 + 0.95 CO + 2 XO_2	1.19×10^{-12}	-220.	a,b
113.	ACO3 + OLN-> HCHO + ALD + 0.5 ORA2 + NO_2 + 0.5 MO_2	4.2×10^{-14}	-220.	a, b
114.	OLN + OLN -> 2 HCHO + 2 ALD + 2 NO_2	3.6×10^{-16}	-220.	
115.	XO_2 + HO_2 -> OP2	7.7×10^{-14}	-1300.	a
116.	XO_2 + MO_2 -> HCHO + HO_2	1.7×10^{-14}	-220.	a, b
117.	XO_2 + ACO_3 -> MO_2	4.2×10^{-14}	-220.	a, b
118.	XO_2 + XO_2 ->	3.6×10^{-16}	-220.	a, b
119.	XO_2 + NO-> NO_2	4.2×10^{-12}	-180.	a
120.	XNO_2 + NO_2 -> ONIT	4.2×10^{-12}	-180.	a
121.	XNO_2 + HO_2 -> OP2	7.7×10^{-14}	-1300.	a
122.	XNO_2 + MO_2 -> HCHO + HO_2	1.7×10^{-14}	-220.	a, b
123.	XNO_2 + ACO_3 -> MO_2	4.2×10^{-14}	-220.	a, b
124.	XNO_2 + XNO_2 ->	3.6×10^{-16}	-220.	b

[a] *DeMore et al.* [1988].
[b] *Atkinson and Lloyd* [1984].
[c] *Cantrell et al.* [1985].
[d] *Uselman et al.* [1979].
[e] *Atkinson* [1986].
[f] Rate constant is of the form $k = T^2 A \exp[-E/(RT)]$.
[g] Rate constant taken as *n*-butane.
[h] Rate constant taken as U.S. average.
[i] Rate constant taken as *n*-decane.
[j] Products taken from *Lurmann et al.* [1986].
[k] Rate constant taken as U.S. average.
[l] *Carter et al.* [1986]. The reaction of NO_3 with OL2 artifically forms extra carbon. The amount is likely to be so small that is is not considered to be significant.
[m] *Kerr and Calvert* [1985], *Trainer et al.* [1987].
[n] Rate constant is one half ethane.
[o] *Atkinson and Carter* [1984].

Figure C.1: Chemical species and reactions in RADM2. Adapted from Stockwell et al. [13].

Appendix D

Urban Pollution Scenario

The initial gas concentrations and emissions in RADM2 are adapted from the PLUME1 scenario by Kuhn et al. [100], which was used for model intercomparisons. This scenario was designed to represent the chemistry in the polluted boundary layer with emissions for a variety of trace gases representative for continental European air [100, 128]. The following figures are excerpts from the protocol used for the model intercomparisons. (The intercomparison was initiated by the Chemical Mechanism Working Group (CMWG) of the EUROTRAC-project (European Experiment on Transport and Transformation of Environmentally Relevant Trace Constituents in the Troposphere over Europe).)

APPENDIX: PROTOCOL FOR THE CMWG INTERCOMPARISON

The technical details of the intercomparison are given here in a slightly edited form. It contains all the information necessary to reproduce the calculations for the intercomparison.

CMWG INTERCOMPARISON OF GAS-PHASE CHEMICAL MODULES 1994

Introductory remarks:

This photochemical model comparison (CMWG-intercomp) provides a quantitative basis for evaluating the chemical schemes currently used in the regional modelling of chemistry and transport. This exercise should be useful for all the participants in validating and improving their photochemical simulations.

TASKS:

CALCULATE photochemistry for a "box", i.e., grid-point, as defined below.
BEGIN at local NOON (SZA = 22°) on July 1 (= 0) and integrate for 5 days (= 120 h). CLEAR sky,
ground ALBEDO = 0.10, LATITUDE = 45 N, LON = 0, solar DECLINATION = + 23° (i.e. 1 JULY, 1985).

We will have 5 cases labeled: LAND, BIO, FREE, PLUME/1, PLUME/2

PLUME/1 to be done with prescribed photolysis rates as given below AND EMISSIONS as given below.
PLUME/2 to be done with individual photolysis rates from your own model AND EMISSIONS as given below.

USE EMISSIONS ONLY FOR CASE PUME/1 AND PLUME/2 NO EMISSIONS FOR CASE LAND, BIO, FREE

INITIAL VALUES:

		LAND	BIO	FREE	PLUME/1/2
alt	(km)	0	0	8	0
T	(K)	288.15	288.15	236.21	288.15
p	(mbar)	1013.25	1013.25	356.50	1013.25
N	(# cm^{-3})	2.55E19	2.55E19	1.09E19	2.55E19
H_2O	(%v/v)	1.0	1.0	0.05	1.0
O_3	(ppb)	30	30	100	50
NO	(ppb)	0.1	0.1	0.05	0.2
NO_2	(ppb)	0.1	0.1	0.05	0.5
HNO_3	(ppb)	0.1	0.1	0.1	0.1
CO	(ppb)	100	100	100	200
CH_4	(ppb)	1700	1700	1700	1700
Isoprene	(ppb)	0	1	0	0
H_2	(ppb)	500	500	500	500
H_2O_2	(ppb)	2	2	2	2
HCHO	(ppb)	1	1	0	1
NMHC	(all ppb)	0	0	0	0

EMISSION DATA (for Case PLUME/1 and PLUME/2)
The VOC emissions are based upon the Derwent and Jenkin inventory (*Atmospheric Environment* **25A**(8) 1661–1678, 1991).

To avoid questions concerning the unit of the emisson rate:

$$dc/dt = P - D * c + \text{Emission}$$

therefore "Emission" given in $cm^{-3} s^{-1}$ (Emissions are given as a volume source).

	Species		Emission ($cm^{-3} s^{-1}$)
0	Nitrogen_oxide	NO	1.1E6
0	Nitrogen_dioxide	NO_2	0.0
0	Sulphur_dioxide	SO_2	2.2E5
0	Carbon_monoxide	CO	2.4E6
0	Methane	CH_4	0.0
			VOC = 3.0E6
1	Ethane	C_2H_6	VOC * 0.0340956
2	Propane	C_3H_8	VOC * 0.00554352
3	*n*-Butane	*n*-C_4H_{10}	VOC * 0.0800388
4	*i*-Butane	*i*-C_4H_{10}	VOC * 0.0434109
5	*n*-Pentane	*n*-C_5H_{12}	VOC * 0.0240418
6	*i*-Pentane	*i*-C_5H_{12}	VOC * 0.0371555
7	*n*-Hexane	*n*-C_6H_{14}	VOC * 0.0137236
8	2-Methylpentane	$CH_3C_5H_{11}$	VOC * 0.0155535
9	3-Methylpentane	$CH_3C_5H_{11}$	VOC * 0.0109789
10	2,2-Dimethylbutane	$CH_3CH_3C_4H_8$	VOC * 0.00155535
11	2,3-Dimethylbutane	$CH_3CH_3C_4H_8$	VOC * 0.00494051
12	*n*-Heptane	*n*-C_7H_{16}	VOC * 0.00621589
13	2-Methylhexane	$CH_3C_6H_{13}$	VOC * 0.00519302
14	3-Methylhexane	$CH_3C_6H_{13}$	VOC * 0.00448488
15	*n*-Octane	*n*-C_8H_{18}	VOC * 0.00400313
16	Methylheptanes	$CH_3C_7H_{15}$	VOC * 0.0138039
17	*n*-Nonane	*n*-C_9H_{20}	VOC * 0.00737645
18	Methyloctanes	$H_3C_8H_{17}$	VOC * 0.00301205
19	*n*-Decane	*n*-$C_{10}H_{22}$	VOC * 0.005541
20	Methylnonanes	$CH_3C_9H_{19}$	VOC * 0.00354624
21	*n*-Undecane	*n*-$C_{11}H_{24}$	VOC * 0.00706122
22	*n*-Duodecane	*n*-$C_{12}H_{26}$	VOC * 0.00647971
23	Ethylene	C_2H_4	VOC * 0.0646318
24	Propylene	C_3H_6	VOC * 0.0155491
25	But-1-ene	C_4H_8	VOC * 0.0073062
26	But-2-ene	C_4H_8	VOC * 0.0134884
27	Pent-2-ene	C_5H_{10}	VOC * 0.00809302
28	Pent-1-ene	C_5H_{10}	VOC * 0.00314729
29	2-Methylbut-1-ene	$CH_3C_4H_7$	VOC * 0.00179845
30	3-Methylbut-1-ene	$CH_3C_4H_7$	VOC * 0.00213566
31	2-Methylbut-2-ene	$CH_3C_4H_7$	VOC * 0.00393411
32	Butylene	C_4H_8	VOC * 0.00210756
33	Acetylene	C_2H_2	VOC * 0.0393411
34	Benzene	C_6H_6	VOC * 0.0171487
35	Toluene	$CH_3C_6H_5$	VOC * 0.0624326
36	*o*-Xylene	*o*-$C_6H_4(CH_3)CH_3$	VOC * 0.0126188
37	*m*-Xylene	*p*-$C_6H_4(CH_3)CH_3$	VOC * 0.0163303
38	*p*-Xylene	*m*-$C_6H_4(CH_3)CH_3$	VOC * 0.0163303
39	Ethylbenzene	$C_2H_5C_6H_5$	VOC * 0.010392
40	*n*-Propylbenzene	*n*-$C_3H_7C_6H_5$	VOC * 0.00216376
41	*i*-Propylbenzene	*i*-$C_3H_7C_6H_5$	VOC * 0.00111466
42	1,2,3-Trimethylbenzene	$CH_3CH_3CH_3C_6H_3$	VOC * 0.00255717
43	1,2,4-Trimethylbenzene	$CH_3CH_3CH_3C_6H_3$	VOC * 0.00983527
44	1,3,5-Trimethylbenzene	$CH_3CH_3CH_3C_6H_3$	VOC * 0.00367183
45	*o*-Ethyltoluene	*o*-$CH_3C_6H_4C_2H_5$	VOC * 0.00334399
46	*m*-Ethyltoluene	$CH_3C_6H_4CH_3$	VOC * 0.00467639
47	*p*-Ethyltoluene	*p*-$CH_3C_6H_4C_2H_5$	VOC * 0.00413081
48	Formaldehyde	HCHO	VOC * 0.0196705
49	Acetaldeyde	CH_3CHO	VOC * 0.00178823
50	Proprionaldehyde	C_2H_5CHO	VOC * 0.00149225
51	Butyraldehyde	*n*-C_3H_7CHO	VOC * 0.00079775
52	*i*-Butyraldehyde	$(CH_3)_2CHCHO$	VOC * 0.000710325
53	Valeraldehyde	*n*-C_4H_9CHO	VOC * 3.65964E-05
54	Benzaldehyde	C_6H_5CHO	VOC * 0.000296914
55	Acetone	CH_3COCH_3	VOC * 0.023062
56	Methyl_ethyl_ketone	$CH_3COC_2H_5$	VOC * 0.0316914
57	Methyl_isobutyl_ketone	$CH_3COC_4H_9$	VOC * 0.00778954
58	Methanol	CH_3OH	VOC * 0.0209
59	Ethanol	C_2H_5OH	VOC * 0.174469
60	Methyl_acetate	$CH_3CO_2CH_3$	VOC * 0.00170124
61	Ethyl_acetate	$C_2H_5CO_2CH_3$	VOC * 0.00554352
62	*i*-Propyl_acetate	*i*-$C_3H_7CH_3CO_2$	VOC * 0.0021599
63	*n*-Butyl_acetate	*n*-$C_4H_9CH_3CO_2$	VOC * 0.00244186
64	*i*-Butyl_acetate	*s*-$C_4H_9CH_3CO_2$	VOC * 0.00305233
65	Methane_chloride	CH_3Cl_2	VOC * 0.0112403
66	Methyl_chloroform	CH_3CCl_3	VOC * 0.00943007
67	Tetrachloroethylene	C_2Cl_4	VOC * 0.00671677

PHOTOLYSIS FREQUENCIES

Since the main goal of the intercomparison is the comparison of chemical schemes, we prescribe the photolysis rates. Tl data are based on the radiation transport model by E. P. Roeth (KFA-Juelich). The photolytic processes included are tho from the RADM2. In case your mechanism contains additional photolytic processes scale their rates to a similar photolyt process.

Photolysis rates with products and educts as given from Roeth

P1 $NO_2 \rightarrow O^3P + NO$
J = PHUX (1.07E-02, 1.01319, 0.83330, CHI)

P2 $O_3 \rightarrow O^1D + O_2$
J = PHUX (3.22E-05, 4.45037, 0.78028, CHI)

P3 $O_3 \rightarrow O^3P + O_2$
J = PHUX (5.36E-04, 0.34764, 0.91030, CHI)

P4 $HONO \rightarrow HO + NO$
J = PHUX (8.96E-04, 0.99438, 0.83295, CHI)

P5 $HNO_3 \rightarrow HO + NO_2$
J = PHUX (5.48E-07, 2.86922, 0.79561, CHI)

P6 $HNO_4 \rightarrow HO_2 + NO_2$
J = PHUX (3.90E-06, 2.37354, 0.79830, CHI)

P7 $NO_3 \rightarrow NO + O_2$
J = PHUX (2.74E-02, 0.26226, 0.92849, CHI)

P8 $NO_3 \rightarrow NO_2 + O_3P$
J = PHUX (2.73E-01, 0.29327, 0.92401, CHI)

P9 $H_2O_2 \rightarrow 2HO$
J = PHUX (7.78E-06, 1.91463, 0.79810, CHI)

P10 $HCHO \rightarrow H_2 + CO$
J = PHUX (4.92E-05, 1.60973, 0.80184, CHI)

P11 $HCHO \rightarrow H + HCO$
J = PHUX (4.05E-05, 2.06917, 0.80267, CHI)

P12 $CH_3CHO \rightarrow CH_3 + CHO$
J = PHUX (5.40E-06, 2.52915, 0.79722, CHI)

P13 $CH_3OOH \rightarrow CH_3O + HO$
J = PHUX (6.37E-06, 1.76570, 0.80004, CHI)

P15 $CH_3CO_3H \rightarrow$ products
J = PHUX (6.10E-09, 9.17009, 0.72585, CHI)

P16 $CH_3COCH_3 \rightarrow$ products
J = PHUX (1.32E-05, 2.46350, 0.79768, CHI)

P17 $CHOCHO \rightarrow$ products
J = PHUX (3.11E-03, 0.55016, 0.88313, CHI)

P19 $CH_3COCHO \rightarrow$ products
J = PHUX (1.85E-03, 0.57967, 0.87921, CHI)

P20 $DCB \rightarrow$ products
J = PHUX (6.39E-04, 1.53712, 0.80233, CHI)

P21 $C_2H_5ONO_2 \rightarrow$ products
J = PHUX (7.20E-08, 9.11436, 0.72600, CHI)

P22 $N_2O_5 \rightarrow O_3P + 2NO_2$
J = PHUX (3.79E-05, 1.70537, 0.80153, CHI)

P23 $MeCOEt \rightarrow$ products
J = PHUX (1.36E-05, 2.59915, 0.80212, CHI)

P24 $CH_3COCOCH_3 \rightarrow 2\ CH_3COO_2$

COMMENT scaled according to EMEP Mechanism ratio $J(CH_3COCOCH_3)/J(GLY)$
J = PHUX (1.53E-02, 0.55016, 0.88313, CHI)

```
C.....
      FUNCTION PHUX(X, Y, Z, CHI)
C
C     CALCULATION OF PHOTOLYSIS RATES WITH ALGORITHM FROM ROETHS PROGRAM
C     CHI = SOLAR ZENITH ANGLE (IN RADIAN)
C     X, Y, Z FROM ROETH
C     X IS PHOTOLYSIS RATE IN 1/S FOR CHI = 0
C
C     KUHN 07.09.93
C
      IMPLICIT NONE
      REAL*8 X, Y, Z, CHI, CHIZ, YCHIZ, MINYZ, EYCHIZ, EMINYZ, PHUX
      PARAMETER (MINYZ = - 30, EMINYZ = 9.357623D-14)   !EMINYZ = EXP(MINYZ)
      CHIZ = CHI * Z
      IF (CHIZ.LT.1.57079632679489D0) THEN
         YCHIZ = Y * (1.0 - (1.0/ COS(CHIZ)))
         IF (YCHIZ.GT.MINYZ) THEN
            EYCHIZ = DEXP (YCHIZ)
         ELSE
            EYCHIZ = EMINYZ
         ENDIF
      ELSE
         EYCHIZ = EMINYZ
      ENDIF
      PHUX = X * EYCHIZ
      RETURN
      END
C.....
```

CALCULATED VALUES FOR PHUX (EXAMPLE FOR COMPARISON)

P1 $NO_2 \rightarrow O_3P + NO$
J = PHUX (1.07E-02, 1.01319, 0.83330, CHI)
X = 1.07E-02, Y = 1.01319, Z = 0.83330

NCHI/GRAD	$J(NO_2)/S - 1$
0	0.1070E-01
10	0.1058E-01
20	0.1024E-01
30	0.9636E-02
40	0.8765E-02
50	0.7593E-02
60	0.6094E-02
70	0.4278E-02
80	0.2283E-02
90	0.5883E-03

END OF CMWG INTERCOMPARISON PROTOCOL

Figure D.1: Initial gas concentrations, emissions, and photolysis parameters and calculations. Adapted from Kuhn et al. [100].

Appendix E

RADM2 Code Structure

A version of the RADM2 code with the added heterogeneous chemistry extensions can be downloaded from:

`http://atmos.msrc.sunysb.edu/marco/`

An instruction describing how to compile and run the code can be found in the README file in the RADM directory.

E.1 General Structure

A diagram outlining the general structure of the RADM2 code is shown in Figure E.1.

The files multi_n and plumeNOx1 supply temperature, pressure parameters, as well as initial gas concentrations and emission rates to the main program of the RADM2 program code which is radm_eff. radm_eff initializes the simulation with the supplied values and then starts the integration loop consisting of the stepwise iteration of the subroutine chem. chem computes the rate coefficients of the represented reactions, e. g., via expression (2.16). The photolysis rates are calculated in dependence of the time of day and the solar zenith angle in the subroutine phot. After that, chem calls four subroutines in succession. The first is prate, which computes the reaction rates for each represented reaction, in analogy to expression (2.14). Then the subroutine produ is called, which derives the chemical differential equations from the reactions rates and sorts them with respect to production and loss terms. Next, setdtc sets the chemical time step for the iteration routine in radm_eff, based on limiting the maximum percent change allowed in the species' concentrations. Finally, integ1 is called, which is the chemical integration routine. After the integration is completed,

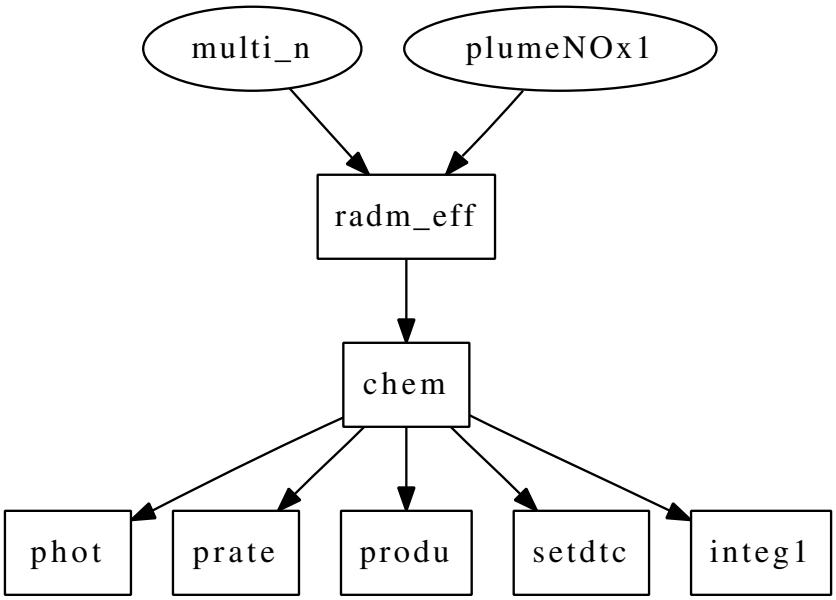

Figure E.1: Code structure of the RADM2 mechanism.

radm_eff advances by one time step and chem is called again. The simulation is completed when the final time is reached.

The following section presents code excerpts that outline the implemented heterogeneous reactions.

E.2 PRA Extension of RADM2

In the extended RADM2-PRA framework, the chem subroutine includes the computation of the pseudo-first order loss coefficient and the net uptake coefficient as shown in Listing E.1. The steps of this computation, exemplified for the gas-phase loss of O_3 are:

- the calculation of the partial and total surface coverage in lines 67–70, in accord with (3.11);
- the calculation of the species mean molecular velocity in line 90 and converting its gas concentration and surface reaction rates in lines 94 and 96–98, respectively;
- the calculation of the uptake coefficient $\gamma_{\mathrm{X}-i}$, which is composed of the calculations of the adsorption, desorption, and collision fluxes, from lines 101–111;

- gas-phase diffusion processes may be calculated in lines 115–121;
- finally, the reaction coefficient for the heterogeneous gas-phase loss is calculated in line 136.

The calculation of the reaction coefficient for the gas-phase loss of NO_2 and H_2O is analogous. The implementation of soot emission scenarios by surface replenishment, which is described in section 3.2.3, is executed in lines 258–285. Comments in the code that are meant to guide the reader start either with a "c" at the beginning of a line, or with a "!" within the line.

The heterogeneous loss rate, i. e. the product of the rate coefficient with the species gas-phase concentration, is calculated in subroutine prate as shown in Listing E.2. In addition to the gas-phase loss rates calculated in lines 17, 20, and 22, the reaction rates for the adsorbents' surface reactions are calculated in the remaining lines of 14–22.

The subroutine produ, with an excerpt shown in Listing E.3, groups the calculated reaction rates to the species' overall loss and production rates, which are equivalent to their chemical differential equation as given in section 3.2.1. The differential equations are then solved, together with the differential equations for the gas-phase and photolysis reactions, as described earlier, in section E.1.

Listing E.1: Excerpt from chem.f

```
1         SUBROUTINE CHEM
2
3         REAL C_O3, RM_O3, O3_CM3, ALPHA_O3
4         REAL GAMMA_O3
5         REAL SIGMA_O3, TAU_O3
6         REAL J_ADS_O3, J_DES_O3, J_COLL_O3
7         REAL KO3_1, KO3_2, KO3_3
8         REAL PROD_O3S, LOSS_O3S1, LOSS_O3S2
9
10        REAL C_NO2, RM_NO2, NO2_CM3, ALPHA_NO2
11        REAL GAMMA_NO2
12        REAL SIGMA_NO2, TAU_NO2
13        REAL J_ADS_NO2, J_DES_NO2, J_COLL_NO2
14        REAL KNO2_1, KNO2_2
15        REAL PROD_NO2S, LOSS_NO2S1, LOSS_NO2S2
16        REAL THETA_S, THETA_O3, THETA_NO2
17        REAL RM_N2O5, C_N2O5, GAMMA_N2O5, SURF_N2O5
18
19        REAL C_H2O, H2O_CM3, ALPHA_H2O
20        REAL GAMMA_H2O
```

```
21          REAL TAU_H2O
22          REAL J_ADS_H2O, J_DES_H2O, J_COLL_H2O
23          REAL PROD_H2OS, LOSS_H2OS1, LOSS_H2OS2
24          REAL THETA_H2O, SIGMA_H2O
25
26          REAL Cg_O3, Cg_NO2, Cg_H2O, F_O3, F_NO2, F_H2O
27          REAL Kn_O3, Kn_NO2, Kn_H2O
28          REAL GAMMA_EFF_O3, GAMMA_EFF_NO2, GAMMA_EFF_H2O
29
30          INTEGER GPDCF_O3, GPDCF_NO2, GPDCF_H2O
31          INTEGER SR_O3, SR_NO2, SR_H2O
32          INTEGER SOOT_EMIT
33          INTEGER z
34
35          PARAMETER (RM_O3 = 48.E-03)
36          PARAMETER (R_GAS = 8.314472)
37          PARAMETER (ALPHA_O3 = 0.001)
38          PARAMETER (SIGMA_O3 = 1.8E-15)
39          PARAMETER (TAU_O3 = 18E0)
40          PARAMETER (KO3_1 = 2.1E-17)
41          PARAMETER (KO3_2 = 2.1E-19)
42          PARAMETER (KO3_3 = 2.1E-21)
43
44          PARAMETER (RM_NO2 = 46.E-03)
45          PARAMETER (ALPHA_NO2 = 0.14)
46          PARAMETER (SIGMA_NO2 = 3.E-15)
47          PARAMETER (TAU_NO2 = 18E0)
48          PARAMETER (KNO2_1 = 7.E-18)
49          PARAMETER (KNO2_2 = 3.7E-3)
50          PARAMETER (GAMMA_N2O5 = 0.02)
51
52          PARAMETER (ALPHA_H2O = 0.0004)
53          PARAMETER (SIGMA_H2O = 1.08E-15)
54          PARAMETER (TAU_H2O = 0.003)
55
56          PARAMETER (Kn_O3 = 2.3524)
57          PARAMETER (Kn_NO2 = 2.1768)
58          PARAMETER (Kn_H2O = 2.1728)
59  C
60  C
61  C ***********************************************************
62  C SURFACE REACTIONS ON SOOT
63  C ***********************************************************
```

```
64  c
65  c IMPLEMENTATION OF ONE SOOT SURFACE
66  c surface coverages:
67            THETA_O3 = SIGMA_O3 * VC(1,1,LO3S)
68            THETA_NO2 = SIGMA_NO2 * VC(1,1,LNO2S)
69            THETA_H2O = SIGMA_H2O * VC(1,1,LH2OS)
70            THETA_S = THETA_O3 + THETA_NO2 + THETA_H2O
71  c
72  c*************************************************************
73  c Adsorption of O3 and sequential surface layer reactions
74  c*************************************************************
75  c         Y1(=BaP), Y2, Y3, Y4: non-volatile components
76  c         SLR1: O3(s)+Y1(ss)-> Y2(ss)
77  c         SLR2: O3(s)+Y2(ss)-> Y3(ss)
78  c         SLR3: O3(s)+Y3(ss)-> Y4(ss)
79  c         neglect surface-bulk transport, gas-surface,
80  c         and surface-bulk reactions
81  c*************************************************************
82  c
83  c         Enable/disable:
84            SR_O3 = 1
85            IF (SR_O3 .eq. 1) THEN
86  c
87  c         MEAN VELOCITY OF MOLECULES in cm/min;
88  c         sqrt[J/(K*mol)*K/(kg/mol)]*cm/m*s/min with J=kg*(m2/s2)
89  c         -> [cm/min]
90              C_O3 = sqrt(8.*R_GAS*T(1,1)/(PI*RM_O3))*100.*60.
91
92  c         CONVERSION OF OZONE CONCENTRATION IN CM-3
93  c         [molecules/cm3]=N*[ppmv]*1e-6 with N=p/(Tk), 1/k=7.242E18
94              O3_CM3 = VC(1,1,LO3)*7.242E12*p(1,1)/T(1,1)
95
96              RK(1,141) = KO3_1 * 60.          ![cm2/min]
97              RK(1,142) = KO3_2 * 60.
98              RK(1,143) = KO3_3 * 60.
99
100 c         Production and loss terms are in [1/(cm2*min)]
101             PROD_O3S = 0.25 * ALPHA_O3 * C_O3 * O3_CM3
102
103             LOSS_O3S1 = 0.25 * ALPHA_O3 * C_O3 * O3_CM3
104       &         * THETA_S
105             LOSS_O3S2 = 1.0*60./TAU_O3 * VC(1,1,LO3S)
106
```

```
107             J_ADS_O3 = PROD_O3S - LOSS_O3S1
108             J_DES_O3 = LOSS_O3S2
109             J_COLL_O3 = 0.25 * C_O3 * O3_CM3
110
111             GAMMA_O3 = (J_ADS_O3 - J_DES_O3)/J_COLL_O3
112
113 c         CALCULATION OF GAS PHASE DIFFUSION CORRECTION FACTOR
114 c         AND EFFECTIVE GAMMA
115             GPDCF_O3 = 1   !enable/disable
116             IF (GPDCF_O3 .eq.1) THEN
117                   F_O3 = 0.75+0.28*Kn_O3/(Kn_O3*(1.+Kn_O3))
118                   Cg_O3 = 1./(1.+F_O3*GAMMA_O3)
119                   GAMMA_EFF_O3 = Cg_O3 * GAMMA_O3
120                   GAMMA_O3 = GAMMA_EFF_O3
121             ENDIF
122 c
123           ELSE
124             GAMMA_O3 = 0.
125             RK(1,141) = 0.
126             RK(1,142) = 0.
127             RK(1,143) = 0.
128             PROD_O3S = 0.
129             LOSS_O3S1 = 0.
130             LOSS_O3S2 = 0.
131             C_O3 = sqrt(8.*R_GAS*T(1,1)/(PI*RM_O3))*100.*60.
132           ENDIF
133 c
134 c         Reaction coefficient for gas-phase loss in min-1;
135 c         VC(1,1,LSOOT)=[SURF] in cm2/cm3
136           RK(1,144) = 0.25 * GAMMA_O3 * C_O3 * VC(1,1,LSOOT)
137 c
138 c
139 c*************************************************************
140 c Adsorption of NO2 and sequential surface layer reactions
141 c*************************************************************
142 c         Y2, Y3, Y5: non-volatile components
143 c         SLR4: NO2(s)+Y2(ss)-> Y5(ss)
144 c         SLR5: NO2(s)+Y3(ss)-> HONO(g)
145 c         neglect surface-bulk transport, gas-surface,
146 c         and surface-bulk reactions
147 c*************************************************************
148 c
149 c         Enable/disable:
```

```
150           SR_NO2 = 1
151           IF (SR_NO2 .eq. 1) THEN
152   c
153   c       MEAN VELOCITY OF MOLECULES in cm/min;
154   c       sqrt[J/(K*mol)*K/(kg/mol)]*cm/m*s/min with J=kg*(m2/s2)
155   c       -> [cm/min]
156             C_NO2 = sqrt(8.*R_GAS*T(1,1)/(PI*RM_NO2))*100.*60.
157
158   C       CONVERSION OF NO2 CONCENTRATION IN CM-3
159   c       [molecules/cm3]=N*[ppmv]*1e-6 with N=p/(Tk), 1/k=7.242E18
160             NO2_CM3 = VC(1,1,LNO2)*7.242E12*p(1,1)/T(1,1)
161   c
162             RK(1,145) = KNO2_1 * 60.
163             RK(1,146) = KNO2_2*VC(1,1,LSOOT)
164          &                 /(7.242E12*p(1,1)/T(1,1)) * 60.
165   c
166   c       Production and loss terms are in [1/(cm2*min)]
167             PROD_NO2S = 0.25 * ALPHA_NO2 * C_NO2 * NO2_CM3
168   c
169             LOSS_NO2S1 = 0.25 * ALPHA_NO2 * C_NO2 * NO2_CM3
170          &       * THETA_S
171             LOSS_NO2S2 = 1.0*60./TAU_NO2 * VC(1,1,LNO2S)
172   c
173             J_ADS_NO2 = PROD_NO2S - LOSS_NO2S1
174             J_DES_NO2 = LOSS_NO2S2
175             J_COLL_NO2 = 0.25 * C_NO2 * NO2_CM3
176   c
177             GAMMA_NO2 = (J_ADS_NO2 - J_DES_NO2)/J_COLL_NO2
178   c
179   c       CALCULATION OF GAS PHASE DIFFUSION CORRECTION FACTOR
180   c       AND EFFECTIVE GAMMA
181             GPDCF_NO2 = 1 !enable/disable
182             IF (GPDCF_NO2 .eq. 1) THEN
183                   F_NO2 = 0.75+0.28*Kn_NO2/(Kn_NO2*(1.+Kn_NO2))
184                   Cg_NO2 = 1./(1.+F_NO2*GAMMA_NO2)
185                   GAMMA_EFF_NO2 = Cg_NO2 * GAMMA_NO2
186                   GAMMA_NO2 = GAMMA_EFF_NO2
187             ENDIF
188   c
189           ELSE
190             GAMMA_NO2 = 0.
191             PROD_NO2S = 0.
192             LOSS_NO2S1 = 0.
```

```
193             LOSS_NO2S2 = 0.
194             RK(1,145) = 0.
195             RK(1,146) = 0.
196             C_NO2 = sqrt(8.*R_GAS*T(1,1)/(PI*RM_NO2))*100.*60.
197           ENDIF
198 c
199 c         Reaction coefficient for gas-phase loss in min-1;
200 c         VC(1,1,LSOOT)=[SURF] in cm2/cm3
201           RK(1, 147) = 0.25 * GAMMA_NO2 * C_NO2 * VC(1,1,LSOOT)
202 c
203 c
204 c*************************************************************
205 c COMPETITIVE ADSORPTION OF H2O ON SOOT
206 c physiosorption; no surface reactions
207 c*************************************************************
208 c
209 c         Enable/disable:
210           SR_H2O = 1
211           IF (SR_H2O .eq. 1) THEN
212 c
213 c         MEAN VELOCITY OF MOLECULES in cm/min;
214 c         sqrt[J/(K*mol)*K/(kg/mol)]*cm/m*s/min with J=kg*(m2/s2)
215 c         -> [cm/min]
216             C_H2O = sqrt(8.*R_GAS*T(1,1)/(PI*18.E-3))*100.*60.
217
218 c         CONVERSION OF H2O CONCENTRATION IN CM-3
219 c         [molecules/cm ]=N*[ppmv]*1e-6 with N=p/(Tk), 1/k=7.242E18
220             H2O_CM3 = VC(1,1,LH2O)*7.242E12*p(1,1)/T(1,1)
221 c
222 c         Production and loss terms are in [1/(cm2*min)]
223             PROD_H2OS = 0.25 * ALPHA_H2O * C_H2O * H2O_CM3
224 c
225             LOSS_H2OS1 = 0.25 * ALPHA_H2O * C_H2O * H2O_CM3
226      &          * THETA_S
227             LOSS_H2OS2 = 1.0*60./TAU_H2O * VC(1,1,LH2OS)
228 c
229             J_ADS_H2O = PROD_H2OS - LOSS_H2OS1
230             J_DES_H2O = LOSS_H2OS2
231             J_COLL_H2O = 0.25 * C_H2O * H2O_CM3
232 c
233             GAMMA_H2O = (J_ADS_H2O - J_DES_H2O)/J_COLL_H2O
234 c
235 c         CALCULATION OF GAS PHASE DIFFUSION CORRECTION FACTOR
```

```
236 c         AND EFFECTIVE GAMMA
237             GPDCF_H2O = 1 !enable/disable
238             IF (GPDCF_H2O .eq. 1) THEN
239                   F_H2O = 0.75+0.28*Kn_H2O/(Kn_H2O*(1.+Kn_H2O))
240                   Cg_H2O = 1./(1.+F_H2O*GAMMA_H2O)
241                   GAMMA_EFF_H2O = Cg_H2O * GAMMA_H2O
242                   GAMMA_H2O = GAMMA_EFF_H2O
243             ENDIF
244 c
245           ELSE
246             GAMMA_H2O = 0.
247             PROD_H2OS = 0.
248             LOSS_H2OS1 = 0.
249             LOSS_H2OS2 = 0.
250             C_H2O = sqrt(8.*R_GAS*T(1,1)/(PI*18.E-3))*100.*60.
251           ENDIF
252 c
253 c         Reaction coefficient for gas-phase loss in min-1;
254 c         VC(1,1,LSOOT)=[SURF] in cm2/cm3
255           RK(1,149) = 0.25 * GAMMA_H2O * C_H2O * VC(1,1,LSOOT)
256 c
257 c
258 c*************************************************************
259 c EMISSION OF NEW SOOT
260 c modeled as emission of surface species Y1
261 c EMISSION SCENARIOS: 4x a day; 24x a day
262 c*************************************************************
263 c
264           SOOT_EMIT = 0
265           IF (SOOT_EMIT .eq. 1) THEN
266 c
267 c EMISSIONS 4x a day:
268 c         DO z=1,20,1
269 c           IF (TIMNOW.ge.(720+360*z).and.TIMNOW.lt.(720.0016+360*z)) THEN
270
271 c EMISSIONS 24x a day:
272           DO z=1,120,1
273             IF (TIMNOW.ge.(720+60*z).and.TIMNOW.lt.(720.0016+60*z)) THEN
274 c
275                   VC(1,1,LH2OS) = 0.
276                   VC(1,1,LNO2S) = 0.
277                   VC(1,1,LO3S) = 0.
278                   VC(1,1,LY5) = 0.
```

```
279                     VC(1,1,LY4) = 0.
280                     VC(1,1,LY3) = 0.
281                     VC(1,1,LY2) = 0.
282                     VC(1,1,LY1) = 1.0E14
283               ENDIF
284             END DO
285             ENDIF
286  c
287  c*************************************************************
288  c END REACTION AT SOOT SURFACE
289  c  ************************************************************
```

Listing E.2: Excerpt from prate.f

```
1  C*************************************************************
2        SUBROUTINE PRATE (K,I)
3  C*************************************************************
4  C**      DESCRIPTION:
5  C**        SUBROUTINE PRATE COMPUTES THE REACTION RATES FOR EACH
6  C**        INDIVIDUAL REACTION IN THE CHEMICAL SOLVER.  THE GENERAL
7  C**        FORMULA FOR THE COMPUTATION RATE OF A SPECIFIC CHEMICAL
8  C**        REACTION IS GIVEN AS SUCH:
9  C**
10 C**           RATE REACTION K = RATE K * REACTANT1 * REACTANT2 ...
11 C*************************************************************
12
13 CN ---- ADDITIONAL REACTIONS ON SOOT SURFACE
14       CRK(J, 141) = RK(J, 141) * VC(J,K, LO3S) * VC(J,K,LY1)
15       CRK(J, 142) = RK(J, 142) * VC(J,K, LO3S) * VC(J,K,LY2)
16       CRK(J, 143) = RK(J, 143) * VC(J,K, LO3S) * VC(J,K,LY3)
17       CRK(J, 144) = RK(J, 144) * VC(J,K, LO3)
18       CRK(J, 145) = RK(J, 145) * VC(J,K, LNO2S) * VC(J,K,LY2)
19       CRK(J, 146) = RK(J, 146) * VC(J,K, LNO2S) * VC(J,K,LY3)
20       CRK(J, 147) = RK(J, 147) * VC(J,K, LNO2)
21 C     CRK(J, 148) = RK(J, 148) * VC(J,K, LSOOT)
22       CRK(J, 149) = RK(J, 149) * VC(J,K, LH2O)
23 12      CONTINUE
24 C
25       RETURN
26       END
27 C*************************************************************
```

Listing E.3: Excerpt from produ.f

```
1  C*************************************************************
```

```
      SUBROUTINE PRODU
C*****************************************************************
C**     DESCRIPTION:
C**       SUBROUTINE PRODU DERIVES THE DIFFERENTIAL EQUATIONS FROM THE
C**       REACTION RATES COMPUTED IN THE PRATE SUBROUTINE.
C*****************************************************************
c
       REAL PROD_O3S, LOSS_O3S1, LOSS_O3S2,
     & PROD_NO2S, LOSS_NO2S1, LOSS_NO2S2,
     & PROD_H2OS, LOSS_H2OS1, LOSS_H2OS2
c
c*****************************************************************
c         O3, NO2, H2O SURFACE REACTION TERMS:
c*****************************************************************
c
c PRODUCTION AND LOSS TERMS OF O3 SURFACE REACTION
c
       DO J = JCS,JCE
          LOSS(J,LO3S)= LOSS_O3S2 + LOSS_O3S1
     1          + CRK(J,141) + CRK(J,142) + CRK(J,143)
          LOSS(J,LY1) = CRK(J,141)
          LOSS(J,LY2) =  CRK(J,142) + CRK(J,145)
          LOSS(J,LY3) =  CRK(J,143) + CRK(J,146)
          LOSS(J,LSOOT) = 0.
       ENDDO

       DO J = JCS,JCE
          PROD(J,LO3S)= PROD_O3S
          PROD(J,LY2) = CRK(J,141)
          PROD(J,LY3) = CRK(J,142)
          PROD(J,LY4) = CRK(J,143)
       ENDDO

c PRODUCTION AND LOSS TERMS OF NO2 SURFACE REACTION
c
       DO J = JCS,JCE
          LOSS(J,LNO2S)= LOSS_NO2S2 + LOSS_NO2S1
     1          + CRK(J,145) + CRK(J,146)
          LOSS(J,LY5) = 0.
          LOSS(J,LY6) = 0.
       ENDDO

       DO J = JCS,JCE
```

```
45            PROD(J,LNO2S)= PROD_NO2S
46            PROD(J,LY5) = CRK(J,145)
47          ENDDO
48
49    c PRODUCTION AND LOSS TERMS OF H2O SURFACE ADSORPTION
50    c
51          DO J = JCS,JCE
52            PROD(J,LH2OS)= PROD_H2OS
53            LOSS(J,LH2OS)= LOSS_H2OS2 + LOSS_H2OS1
54            LOSS(J,LH2O) = CRK(J,149)
55          ENDDO
56    c
57    c*****************************************************************
58    c         END OF O3, NO2, H2O SURFACE TERMS
59    c*****************************************************************
60    c
61    c*****************************************************************
62    c         GAS-PHASE PROD AND LOSS TERMS INFLUENCED BY HET.CHEM.:
63    c*****************************************************************
64    C
65    CDIR$ SHORTLOOP
66          DO 30 J = JCS,JCE
67            LOSS(J,LO3) = CRK(J,2) + CRK(J,5)  + CRK(J,6)  + CRK(J,7)
      +
68          1                    CRK(J,8) + CRK(J,17) + CRK(J,84) + CRK(J, 85)+
69          2                    CRK(J,86)+ CRK(J,87)
70          3                    + CRK(J,144)
71    c                           !gas phase loss due uptake
72       30   CONTINUE
73    C
74    CDIR$ SHORTLOOP
75          DO 42 J = JCS,JCE
76            LOSS(J,LNO2) = CRJ(J,1) + CRK(J,2) + CRK(J,10) + CRK(J,17) +
77          1                    CRK(J,19) + CRK(J,21) + CRK(J,24) + CRK(J,53) +
78          2                    CRK(J,55) + CRK(J,132) + CRK(J,147)
79    c                           !gas phase loss due to uptake
80     42    CONTINUE
81    C
82    CDIR$ SHORTLOOP
83          DO 220 J = JCS,JCE
84            PROD(J,LHONO)= CRK(J,15)
85          &                  + (CRK(J,146)*VC(1,1,LSOOT)/(7.242E12*p(1,1)
86          &                                                /T(1,1)))
```

```
87  c                              !production from NO2 surface reaction
88    220   CONTINUE
89  C
90  c*****************************************************************
91  c          END OF GAS-PHASE PROD AND LOSS TERMS INFLUENCED BY HET.CHEM.
92  c*****************************************************************
93  C
94            RETURN
95            END
```